Title
Geodetic and Seismological Investigations of Earthquake Cycle Deformation and Fault Zone Properties

Author
Materna, Kathryn

Publication Date
2019

Peer reviewed|Thesis/dissertation

Geodetic and Seismological Investigations of Earthquake Cycle Deformation and Fault Zone Properties

by

Kathryn Z Materna

A dissertation submitted in partial satisfaction of the

requirements for the degree of

Doctor of Philosophy

in

Earth and Planetary Science

in the

Graduate Division

of the

University of California, Berkeley

Committee in charge:

Professor Roland Bürgmann, Chair
Professor Douglas Dreger
Professor Steven Glaser

Summer 2019

Geodetic and Seismological Investigations of Earthquake Cycle Deformation and Fault Zone Properties

Abstract

Geodetic and Seismological Investigations of Earthquake Cycle Deformation and Fault Zone Properties

by

Kathryn Z Materna

Doctor of Philosophy in Earth and Planetary Science

University of California, Berkeley

Professor Roland Bürgmann, Chair

A number of geologic processes on the surface and in the interior of the Earth result in ground deformation on human timescales. These processes include the steady motion of tectonic plates, the internal deformation of heterogeneous regions in the crust, the response of the Earth to surface loads, and deformation at plate boundaries, all acting to produce millimeter-scale displacements each year. These same processes are also responsible for many natural hazards that cause harm to human communities: earthquakes and tsunamis are the most directly related, but sea level rise and extreme flooding are also pertinent natural threats exacerbated by the deformation of the ground. In order to understand these natural hazards and to mitigate their impacts, it is important to quantify surface deformation and to understand the physical mechanisms underlying it. The chapters of this dissertation address several questions in the field of tectonic deformation that relate to these processes. In particular, I focus on understanding earthquake hazards and fault zone properties using a variety of tools at the intersection of space geodesy and seismology.

Zones of weakness in the Earth's crust at all scales are relevant for the study of natural hazards. They respond to external stresses and often host earthquake ruptures. Fault zones, as one small-scale example, are thought to be mechanically weaker than their surroundings because the accumulated near-fault damage results in lower mechanical strength, forming compliant fault zones. Importantly, the presence of a compliant fault zone around a fault affects the types of earthquake ruptures the fault can sustain. In order to study compliant fault zones around a major fault, I investigated the elastic properties of the crust near the San Andreas Fault Zone in northern California. I used GPS measurements to characterize compliant fault structures along strike and found that their distribution is heterogeneous even over short spatial scales.

Larger zones of weakness also impact present-day deformation. On continental scales, inherited zones of weakness from previous tectonic episodes can affect the seismic activity of a region even millions of years later. In the craton of southern Africa, I studied the rupture process of a rare M6.5 earthquake in Botswana that ruptured the lower crust in a

continental plate interior. Using a joint analysis of teleseismic waveforms, InSAR data, and relocated aftershocks, I identified the rupture plane out of the two possible focal planes. The modeled strike matches with the boundary of an ancient collisional mountain belt that has been reactivated in the present day as a set of normal faults. Intraplate earthquakes such as this one are challenging to forecast because they occur in regions of low interseismic strain, but they can be especially damaging because they occur in places that aren't expecting earthquakes. Understanding the structure of pre-existing weak zones in the crust may be key in such situations.

Clues to the internal structure of the crust may also come from the study of periodic hydrological loads on the Earths surface. Seasonal loads from snow, rivers, lakes, groundwater, the ocean, and the atmosphere cause surface deformation that depends on the structure of the underlying medium and the processes involved. In order to analyze these processes in a tectonically active region, I performed a study on hydrological loading in GPS data from South Asia and Southeast Asia, a region impacted by a strong yearly monsoon. The annual deformation varies across the region but is generally consistent with the elastic loading modeled from an independent gravity dataset. The appropriate modeling of the hydrological loading deformation in the future could help quantify the storage of aquifers, improve our understanding of earthquake cycle deformation, and aid in the accurate detection of transient fault behavior.

The remaining two chapters of this dissertation relate to transient fault behavior of the Mendocino Triple Junction in northern California. This region lies at the intersection of three major plate-bounding faults, and it produces some of the largest earthquakes in California. Several of the plate-bounding faults at the Mendocino Triple Junction produce a mix of seismic and aseismic moment release; this results in fascinating time-dependent slip behavior and an interplay between aseismic and seismic slip modes. In one study of this behavior, I used characteristically repeating earthquakes to identify regions of the Mendocino Fault Zone that are creeping aseismically. Using a dataset from 2008 to 2018, I found several dozen families of small-magnitude repeating earthquakes that show a high degree of active creep on the plate boundary fault. The creep rate is calculated to be about 65% of the overall slip budget, a significant amount but in line with previous estimates of aseismic slip on oceanic transform faults. During this time interval, the slip appears to be relatively steady, but the repeating earthquake catalog allows us to study any time-dependent variations of the creep rate in the future.

On the neighboring Cascadia Subduction Zone, I also find aseismic creep with time-dependent rate variations. Well-known slip transients called Episodic Tremor and Slip events occur on the southern Cascadia Subduction Zone margin every 7-10 months, resulting in several centimeters of slip at about 30 km depth. However, in the final chapter of this dissertation, I document changes in surface velocity that appear uncorrelated with the process of Episodic Tremor and Slip. I find that surface GPS velocities near the Mendocino Triple Junction show systematic variations in their east/west component that last for several years apiece. The timing of several velocity changes is coincident with the timing of large (M>6.5) offshore earthquakes. The spatial pattern and temporal pattern of the observations indicate

that more usual processes like afterslip, viscoelastic relaxation, and hydrological loading are insufficient to explain the observations. Instead, inversion of the velocity changes suggests that in a region slightly updip of the Episodic Tremor and Slip portion of the interface, interseismic coupling may both increase and decrease in connection with the offshore earthquakes. A speculative dynamic triggering mechanism is presented. Such observations suggest that understanding fault zone properties is of paramount importance in the study of earthquake hazards. The findings also show that in light of newer geodetic and seismological datasets, there is still much to be learned and many unanswered questions about the behavior of fault zones throughout the earthquake cycle.

To David, Peter, Nancy, and Laura.

Contents

List of Figures

List of Tables

Acknowledgments

Firstly, I would like to thank my advisor, Roland Bürgmann, for all he has done over the past five years. As a scientist and as an advisor, Roland is a remarkable example for those of us in his lab. His boundless optimism in the face of research challenges is a skill I hope to always carry with me in my future endeavors. I am also thankful to him for allowing me to follow my intellectual curiosity wherever it leads, trusting in my potential as a scientist even when I did not believe in it myself. I am thankful for Roland's encouragement to pursue goals outside of science too; he reminds us that the best scientists can't do science all the time.

I would like to acknowledge the Active Tectonics research group and all of its members. Thanks in particular to my fellow graduate students and lab-mates Christopher Johnson, Brent Delbridge, Yuexin Li, Patcharaporn Maneerat, Kang Wang, Baptiste Rousset, Chris Milliner, and Lian Xue for all they have taught me and for their part in creating a lab where innovative science is done. I would also like to thank my office mates William Hawley, Christopher Johnson, Qingkai Kong, Yuexin Li, and Runze Miao. I've learned numerous things from them that have made me a better researcher and a better person.

To the talented members of the Berkeley Seismology Lab, I am grateful for many helpful discussions over the years. Their deep knowledge of seismology is an invaluable resource. Thanks especially to Taka'aki Taira and Noel Bartlow, who became second advisors to me during my time at Berkeley. I want to also thank the BSL operations team, whose efforts to operate geophysical networks in Northern California allow for so much of the research that we do.

I am additionally grateful to my collaborators in Singapore, who provided me with an exciting and fruitful research experience abroad. Emma Hill, Eric Lindsey, and Shengji Wei each contributed to this work in a variety of ways, for which I am very thankful.

Finally, I would like to thank my family, who supported me through the ups and downs of these past five years. I owe a special thanks to David, who has been instrumental and this degree would not have been possible without him. Also, I am extremely grateful to my parents and my sister, who were always ready to lend their encouragement and advice. I have relied on their steadfast support through it all.

Chapter 1

Introduction

In the last several decades, space geodesy has opened new avenues for probing the structure and behavior of the earth's crust. By increasing the accuracy, precision, spatial density, and temporal sampling of geodetic measurements, we can address some of the most pressing questions in earth science. These include questions related to earthquake cycle deformation, mountain-building, sea level change, mass loading, landsliding, groundwater withdrawal, soil compaction, and more. In every geodesist's ideal world, an exact spatial and temporal description of deformation would exist globally to allow us to study each of these processes. Although major gaps still exist, recent advances in GPS, InSAR, and seafloor geodesy are making this vision of the "ideal" network closer to a reality than ever before.

Unfortunately, theoretical and practical considerations limit the usefulness of geodesy as an isolated tool to study the earth's mechanics. All deformation observed at the surface is viewed through the filter of the earth's crust, leading to non-uniqueness in modeling the observations. In the simple example of coseismic slip, many different slip distributions can produce the same surface deformation pattern within reasonable uncertainties. Furthermore, contributions from multiple deformation sources are almost always difficult to isolate from one another in geodetic data. The deeper the deformation source, the more challenging the problem becomes.

Geodesists employ several mitigation strategies in these situations. In many cases, especially in under-constrained geodetic inversions, we impose regularization or other forms of reasonableness on the solution. In other cases, increasing the density of observations or the accuracy of the measurements (i.e., bringing our measurements closer to the "ideal" network) could help distinguish between possible models of deformation. However, there is inherent non-uniqueness in these problems and unknown structural heterogeneity of the earth on relevant spatial scales. As a result, it is likely that even with improved spatial resolution and vastly reduced uncertainties on measurements, we would still be unable to answer some key scientific questions with geodetic datasets alone. For example, questions related to fault behavior at larger depths, such as at the brittle-ductile transition, and related to the mechanics of inelastic deformation such as folding would remain difficult to answer even with perfect observations.

A far more powerful technique to make full use of geodetic data is to appropriately integrate them with information from other geophysical data sources. Independent datasets such as aftershock catalogs, microseismicity, seismic waveforms, gravity, and models of global hydrology can provide logical constraints to resolve tradeoffs in models driven by geodetic data alone. In that sense, geodesy research that bridges the boundaries across traditional disciplines has the potential to produce more insightful and accurate scientific understanding than research that relies on space geodesy in isolation.

In my dissertation, I discuss several cases where the use of space geodesy provides insight into earthquake cycle processes such as aseismic creep, coseismic slip, and fault zone damage; however, in each case, further information is gleaned with the incorporation of additional geophysical datasets beyond the geodetic data. In Chapter 2, I use campaign GPS measurements to assess fault zone elastic structure in the San Francisco Bay Area. I test whether elastic models that include a compliant fault zone core are necessary or warranted to explain the measured interseismic velocities on both young and mature sections of the San Andreas Fault. The addition of locking depth constraints from microseismicity resolves some of the ambiguity and trade-off between the locking depth and slip rate in the models, allowing us to place better constraints on both.

In Chapter 3, I use characteristically repeating earthquakes (CREs) at the Mendocino Triple Junction to study aseismic creep from 2008-2018. Aseismic creep is an important fault process that is poorly understood. Its occurrence is traditionally detected geodetically, but in this case, the creep is located on the offshore Mendocino Fault Zone, and we show that land-based GPS is nearly blind to movement on this fault. The analysis of repeating earthquake data (calibrated from historical geodetic measurements) shows strong creep indicators and provides spatiotemporal creep information on a fault that we otherwise know very little about.

Coseismic slip inversions also benefit from the integration of space geodesy with multiple types of geophysical data. I focus Chapter 4 on the case of a M6.5 normal-faulting earthquake in Botswana, an unexpected earthquake far from active plate boundaries. Space geodetic measurements from InSAR provide constraints on the coseismic deformation of several centimeters. However, we find that due to the depth of the earthquake, we are unable to resolve which focal plane the earthquake ruptured using InSAR alone. With the addition of teleseismic waveform data and relocated aftershocks, we conclude that one plane was significantly more likely than the other, a finding that helps us better understand the event within the context of the region's geology.

In Chapter 5, I study the response of the earth's crust to hydrological loads in Southeast Asia, a region with active earthquake cycle deformation and a large seasonal monsoon. GPS time series from this region contain a mixture of signals from these processes and others, all acting on similar timescales and with similar amplitudes. In order to properly separate tectonic deformation processes from hydrological loading, I use data from the GRACE gravity mission that independently constrains the terrestrial water storage as a function of space and time. Models driven by this gravity dataset are generally successful at removing seasonal components from the geodetic time series, allowing for more accurate determination

of tectonic velocities associated with the earthquake cycle.

Finally, I use GPS time series to study time-dependent fault coupling behavior in southern Cascadia in Chapter 6. The coupling of the Cascadia megathrust is a critically important quantity for seismic hazard modeling, and the key conclusion of Chapter 6 — that this quantity changes over years-long timescales — is quite surprising. Although the coupling change signals we observe are small (<5 mm total), they appear to be real. These changes can be isolated and distinguished from hydrological loading, another common cause of small deformation signals, through the use of independent hydrological models. The further addition of an independent tremor catalog into the analysis shows other important details and context of how the megathrust coupling can change in space and time.

It is clear that geodetic data have huge potential to improve our understanding of the earthquake cycle, yet they have inherent limitations in sensitivity, depth resolution, and accuracy. As a result, geodetic data become even more useful when used in combination with other techniques. In that vein, the studies presented here, although all different in their methods, demonstrate the information to be gained by approaching earthquake cycle questions at the border between geodesy and the rest of the geophysical disciplines.

Chapter 2

Contrasts in Compliant Fault Zone Properties from Geodetic Measurements in the San Francisco Bay Area

Published as: Materna, K. and R. Bürgmann (2016), Contrasts in compliant fault zone properties inferred from geodetic measurements in the San Francisco Bay Area, Journal of Geophysical Research: Solid Earth, 121, doi:10.1002/2016JB013243.

2.1 Abstract

In crustal fault zones, regions of damaged rock characterized by reduced elastic shear modulus can influence patterns of near-field interseismic deformation. In order to study these compliant fault zones (CFZs) and how they might develop over the lifetimes of faults, we compare two fault segments with contrasting fault age and lithology along the San Andreas Fault in the San Francisco Bay Area. New geodetic measurements of the interseismic velocity fields at each location are used to constrain fault zone parameters through a Markov Chain Monte Carlo method. At Black Mountain, in the Santa Cruz Mountains of the San Francisco Peninsula, we do not find evidence for a compliant fault zone; instead we find that the geodetic data is more consistent with a model of a single fault in a homogeneous elastic half-space. At Lake San Andreas, a younger fault segment 35 km farther north, we find evidence for a compliant fault zone about 3.4 +1.1/-1.4 km wide, containing a shear modulus of about 40% of the shear modulus of the surrounding rock. We also find that the best-fitting CFZ model at this location, unlike the best-fitting homogeneous half-space model, has a locking depth that agrees well with the observed depth of microseismicity. Based on differences in fault age, cumulative displacement, and lithology between Black Mountain and Lake San Andreas, we infer that lithology plays an important and, in this case, perhaps a dominant

role in the accumulation of fault zone damage structures and the development of CFZs over the lifetime of a fault.

2.2 Introduction

In studies of interseismic crustal deformation, faults are often modeled as dislocations embedded in homogeneous elastic half-spaces (Savage and Burford, 1973). However, increasingly sensitive geodetic measurements of active faults in nature can show deviations from this first-order model. Variations in elastic properties, for example through brittle damage or changes in rock composition, can change a fault's geodetic signature. One important example of a structure that differs from the first-order model of faults is a compliant fault zone (CFZ), or near-fault region of damaged rock characterized by a reduced shear modulus. CFZs have been shown to affect the interpretation of geodetic data for coseismic slip distributions (Barbot et al., 2008), and can affect the type of strong ground motion that structures near the fault zone experience during large earthquakes (Ben-Zion et al., 2015). Recent studies have also shown a connection between faults with CFZs and faults that can sustain supershear ruptures (e.g., Huang et al., 2016). In order to fully understand these features, it is important to characterize the CFZ structures around major faults.

Recent studies have investigated CFZs around the world through a variety of geophysical observations. Discontinuous deformation observed after the Izmit and Landers earthquakes on faults away from the main rupture are consistent with the coseismic elastic deformation of CFZs (Fialko, 2004; Hamiel and Fialko, 2007). Studies of deformation have also investigated the role of CFZs in producing enhanced strain interseismically near the traces of faults in California (Chen and Freymueller, 2002; Jolivet et al., 2009; Lindsey, Sahakian, et al., 2013) and in Venezuela (Reinoza et al., 2015). Furthermore, seismic studies have pointed to the existence of material with low seismic velocity and shear modulus around faults such as the Calico Fault in the Mojave Desert and the central San Andreas Fault (SAF) (Li, Vidale, et al., 2004; Cochran et al., 2009). Xue et al. (2016) also documented the presence of highly permeable, low rigidity material using data from monitoring wells in a 500-meter zone around the SAF. The CFZs that have so far been studied are typically on the order of hundreds of meters to several kilometers wide, and display rigidities up to several times lower than the surrounding rocks.

On the northern SAF in particular, previous geodetic studies have found conflicting evidence for low-rigidity fault zones. Lisowski et al. (1991) suspected the presence of low-rigidity materials in the fault core at a trilateration profile in Point Reyes, north of San Francisco, California. The Electronic Distance Measurement (EDM) data in their study showed high strain rates that were not easily explained by shallow locking depths or shallow fault creep. Chen and Freymueller (2002) analyzed a denser set of EDM and Global Positioning System (GPS) measurements along the northern SAF, finding high strain rates that suggested the presence of a CFZ on the San Francisco Peninsula, but not at Point Reyes where Lisowski et al. (1991) had suggested low-rigidity materials. Jolivet et al. (2009) used a combination

of trilateration, GPS, and Interferometric Synthetic Aperture Radar (InSAR) data to revisit the region north of San Francisco Bay. The results of their work suggest strong variability in the CFZ structures along the SAF, even at small spatial scales. In agreement with earlier results by Chen and Freymueller (2002), Jolivet et al. (2009) find no evidence for a CFZ for a GPS profile at Point Reyes, but a separate geodetic profile only 30 km north of Point Reyes provides strong support for a CFZ.

In this study, we use new GPS measurements of two geodetic networks previously considered by Chen and Freymueller (2002) along the San Francisco Peninsula segment of the SAF. We examine two decades of geodetic measurements to more completely characterize the variations in the CFZ's structure along the SAF. Our study regions are Lake San Andreas (Figure 2.1a) and Black Mountain (Figure 2.1b), both located just south of San Francisco. These two areas provide a contrasting case study for CFZ formation through their differences in fault age, lithology, and tectonic setting.

Generally, the SAF in northern California forms the boundary between the Salinian Block to the west and the San Francisco Bay Block to the east (Figure 2.1c). The Salinian Block is made up of mostly Cretaceous granites and metamorphic rocks overlain by Tertiary sediments (Mattinson, 1978; James, 1992). To the east, the San Francisco Bay Block is a mixture of rocks of the Franciscan complex: mostly sandstone, shale, basalt, chert, and schist derived from the subduction of the former Farallon plate (Blake and Jones, 1974). Plate reconstructions show that the SAF at this latitude, as the primary fault of the plate boundary system, has accommodated about 162 km of right-lateral strike-slip motion over its 12 to 13 million year lifetime (Powell, 1993).

On the San Francisco Peninsula, however, most of the 162 km of right-lateral motion appears to have been accommodated not on the current SAF but on a presently inactive structure called the Pilarcitos Fault, which is west of the SAF and forms the boundary between Salinian and Franciscan rocks (Parsons and Zoback, 1997). Geologic and magnetic studies suggest that slip shifted eastward from the Pilarcitos Fault to the present-day SAF approximately 1.5 million years ago (Hengesh and Wakabayashi, 1995; Jachens and Zoback, 1999), resulting in a long triangular region of the initial San Francisco Bay Block (hatched region in Figure 2.1c) currently moving northwest with the Salinian Block and the Pacific Plate. Since the shift of the active fault trace, this region has been displaced about 23 km to the northwest from its original position (Jachens and Zoback, 1999).

The SAF segments at both the Black Mountain and Lake San Andreas study areas were affected by the Quaternary shift of the Peninsula SAF to its present position. Lake San Andreas is on a young stretch of the Peninsula SAF, with the blocks to the east and west of the fault both having only 23 km of cumulative displacement over active lifetimes of 1.5 million years. Both sides of the fault zone are lithologically part of the Franciscan complex. At Black Mountain, the western side is a relatively mature fault zone, consisting of Salinian rocks that have seen more than 100 km of cumulative displacement. The eastern side is similar to the young fault zone at Lake San Andreas (most easily seen if one imagines the triangular block in Figure 2.1c backtracked to the southeast by 23 km, to its position before the active fault shifted; see Figure 10 in Parsons and Zoback (1997)). The two fault zone

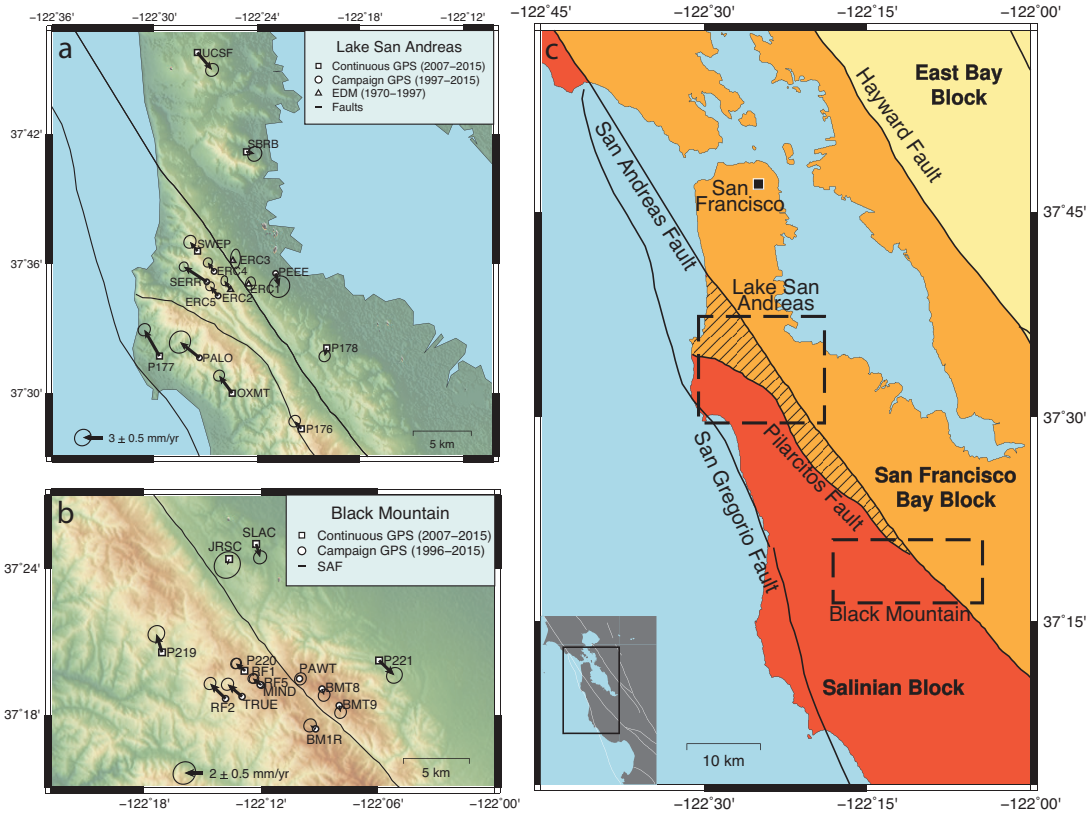

Figure 2.1: a) Map of the Lake San Andreas region showing the GPS and EDM-derived velocities used in this study with 95% confidence ellipses. The velocities are displayed assuming zero velocity at the trace of the SAF. b) Map of Black Mountain showing the GPS velocities used in this study with 95% confidence ellipses. c) Simplified geologic map of the San Francisco Bay Area showing the major faults in the region, including the Pilarcitos Fault. The hatched area shows the region of the San Francisco Bay Block that has been offset by the currently active strand of the SAF at Lake San Andreas. The central regions of the Lake San Andreas and Black Mountain geodetic networks are highlighted in the black dashed boxes.

sections considered in this study therefore have eastern sides that are similar, but western sides that differ in both fault age and lithology.

A further difference between the two fault zones is the present-day tectonic environment. The SAF at Black Mountain goes through a restraining bend of approximately 9 degrees just south of the mapped region in Figure 2.1c, which produces a transpressional environment and uplift of the Santa Cruz Mountains (Scholz, 1985; Anderson, 1990; Bürgmann, Arrowsmith, et al., 1994). The focal mechanisms of small earthquakes in this area, which are mainly strike-slip and reverse, support the idea that the region is currently in transpression (Zoback et al., 1999). In contrast, the SAF at Lake San Andreas is thought to be in transtension associated with a slight releasing bend in the fault trace of approximately 5 degrees, and with the nearby junction of the San Gregorio fault. The earthquakes along this stretch of the fault are a combination of strike-slip and normal faulting events (Zoback et al., 1999).

In this study, we use the Black Mountain and Lake San Andreas segments of the SAF to explore the factors that influence the development of CFZs. Because CFZs consist of highly damaged rocks, it is reasonable to expect that mature fault segments accumulate more brittle damage and thus develop broader CFZs over many earthquake cycles. However, it is also possible that rock composition strongly influences the creation of damage structures like CFZs; this factor may be particularly important in the San Francisco Bay Area, where seismic studies have shown differences in seismic wave speed and shear modulus between Salinian and Franciscan rocks (Parsons and Zoback, 1997; Brocher, 2005; Thurber et al., 2007). In this study we consider the contrasts between Lake San Andreas and Black Mountain in order to investigate the relationships between fault age, fault lithology, tectonic setting, and the presence of CFZs.

2.3 Methods

2.3.1 Data Collection

We collected campaign GPS data at nine geodetic benchmarks at Black Mountain and four benchmarks at Lake San Andreas during the spring and summer of 2015. These benchmarks, all located within five km of the surface trace of the SAF, were installed by the USGS in the 1970s for trilateration surveys. Consequently, we have nearly twenty years of EDM measurements from the 1970s to the 1990s, which were analyzed by Chen and Freymueller (2002), as well as a time series of campaign GPS measurements at each benchmark from 1996-1997 to 2015. The campaign GPS time series at Black Mountain typically contain at least four measurements spaced at intervals between 1996 and 2015. At Lake San Andreas, we only have measurements in 1997 and 2015.

During our campaign, we collected data spanning at least two consecutive days at all sites, with data at many sites spanning five days or more. Daily position estimates and time series were computed for each site using the GAMIT/GLOBK software package, version 10.6 (Herring, King, et al., 2015). Nearby continuous sites, mostly from the Plate Boundary

Observatory (PBO) and Bay Area Regional Deformation (BARD) networks, were processed jointly with the campaign sites in order to improve network stability. Velocities for all stations were calculated using the ITRF08 reference frame. We produced velocity profiles relative to the SAF by projecting the velocities into the fault-parallel direction and solving for an appropriate offset such that measurements at the fault trace have zero fault-parallel velocity (Figure 2.1).

At Lake San Andreas, we were unable to locate two benchmarks (ERC1 and ERC3) that we believe have been obscured or destroyed since their last occupation in 1997. At a third site (ERC2), we suspect that the 1997 and 2015 measurements were accidentally made at separate but nearby benchmarks. For these stations, we only have EDM data to constrain their velocities. We converted the EDM line-length data into fault-parallel velocities using the outer coordinate solution (Prescott, 1981), which produces a fault-parallel velocity field but is not expressed in an absolute reference frame. We then used the network's stations that have both EDM and GPS measurements to place the EDM data into the reference frame of the GPS data. The velocities calculated by EDM and GPS using this method show good agreement (differences are generally less than 0.5 mm/year). This agreement implies that there is very little time-dependence in the interseismic velocity field between the 1970s and 2015.

2.3.2 Modeling

We modeled the Black Mountain and Lake San Andreas velocity fields using three possible deformation models. We focused our modeling on measurements within ten km of the SAF rather than large-scale modeling of the fault system (e.g., d'Alessio et al. (2005)), because in the near-field regions of interest, the SAF dominates the deformation signal and contributions from neighboring faults are small. We calculate that the Hayward Fault, located approximately 20 km to the east and slipping at 10 mm/year, should produce modest deformation gradients of about 0.3 mm/year across the networks in our study ($<$ 0.3 mm/year if accounting for shallow creep on the Hayward Fault). Similarly, the San Gregorio Fault to the west, which is closer but has a lower slip rate, should produce gradients of about 0.3 mm/year across each network. The deformation signal from the SAF in this region is an order of magnitude higher. Therefore, we focus only on the deformation related to the SAF, and model each velocity field using a single fault for the three candidate crustal models below.

Homogeneous elastic half-space model

The arctangent model (Savage and Burford, 1973) contains a homogeneous elastic half-space with a buried dislocation. The fault-parallel velocity field v, as a function of fault-perpendicular distance from the fault trace x, is modeled by an arctangent function with two parameters: slip rate $\dot{s}$, and locking depth d.

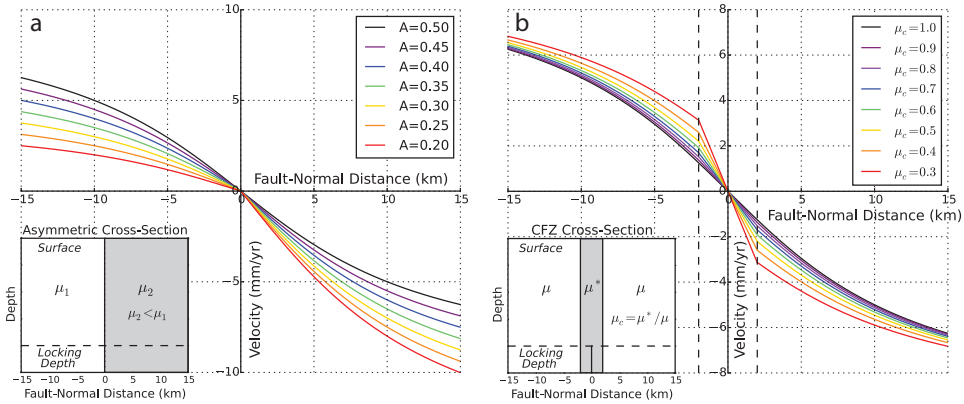

Figure 2.2: a) Fault-parallel velocity profiles for an asymmetric elastic half-space model using a range of values for the asymmetry parameter $A = \mu_2/(\mu_1 + \mu_2)$. b) Fault-parallel velocity profiles for a CFZ model with a 4-km-wide fault zone and variable ratio of elastic modulus μ_c.

$$v(x) = \frac{\dot{s}}{\pi} \arctan\left(\frac{x}{d}\right)$$

Asymmetric elastic half-space model

The asymmetric model, detailed in Le Pichon et al. (2005) and Segall (2010), is an elastic half-space with contrasting shear moduli across the fault (given by μ_1 and μ_2). This model is characterized by three parameters: slip rate $\dot{s}$, locking depth d, and the asymmetry parameter A. The A parameter is defined as $\mu_2/(\mu_1 + \mu_2)$, and is equal to 0.5 when the model has no contrast in rigidity. As defined, this parameter ensures that the portion of the model domain with lower shear modulus experiences higher-amplitude deformation (Figure 2.2a). This model, like the homogeneous half-space and the CFZ models, has the fault trace located at $x = 0$.

$$x < 0 : v(x) = \frac{2A\dot{s}}{\pi} \arctan\left(\frac{x}{d}\right)$$

$$x \geq 0 : v(x) = \frac{2(1-A)\dot{s}}{\pi} \arctan\left(\frac{x}{d}\right)$$

Compliant Fault Zone model

The Compliant Fault Zone model is an elastic half-space of shear modulus μ containing a fault zone characterized by a reduced elastic shear modulus μ^* (Figure 2.2b). This model

has four parameters: slip rate $\dot{s}$, locking depth d, contrast in shear modulus (expressed as a ratio $\mu_c = \mu^*/\mu$, which ranges from 0 to 1), and half-width w of the fault zone. The analytical solutions for the velocity field are from Rybicki and Kasahara (1977) and from Segall (2010). A parameter k is defined as $(\mu - \mu^*)/(\mu + \mu^*)$.

$$x \leq -w : v(x) = \frac{2(1-k)\dot{s}}{\pi} \sum_{n=0}^{\infty} k^n \arctan\Big(\frac{x - 2nw}{2d}\Big)$$

$$-w < x < w : v(x) = \frac{\dot{s}}{\pi}\Big[\arctan\big(\frac{x}{2d}\big) + \sum_{n=1}^{\infty} k^n\big[\arctan\big(\frac{x-2nw}{2d}\big) + \arctan\big(\frac{x+2nw}{2d}\big)\big]\Big]$$

$$x \geq w : v(x) = \frac{2(1-k)\dot{s}}{\pi} \sum_{n=0}^{\infty} k^n \arctan\Big(\frac{x + 2nw}{2d}\Big)$$

In each case, the fault was modeled as a vertical, infinitely deep dislocation below the locking depth. CFZs in nature, formed as damage zones in earthquakes, are likely no deeper than the locking depth of the fault. Jolivet et al. (2009) found that finite-element modeling of a CFZ with depth equal to the locking depth changed the predictions of surface deformation by less than 5% of the far-field velocity compared to an infinitely-deep CFZ. The results the finite-depth CFZ show a narrower and steeper velocity gradient across the fault than the infinitely-deep CFZ model, but the differences never exceed 1 mm/year (Jolivet et al., 2009). Because the differences are small, we performed model comparisons using the analytical solutions for an infinitely deep CFZ and dislocation for this study.

For each model and study area, we identified best-fit parameter values of slip rate, locking depth, etc., using a Markov Chain Monte Carlo (MCMC) method (Metropolis et al., 1953; Patil et al., 2010). This method was chosen for its ability to identify regions of the parameter space with high probability given the observed data, while also allowing for the use of prior information using Bayes' Rule (Bayes, 1763). In the case of our analysis, the prior information was derived from independent data sources such as geologic slip rate estimates and the depth extent of seismicity. We chose prior distributions for slip rate and locking depth based on the UCERF-3 (Field et al., 2014) fault model (17 ± 3 mm/year slip rate on the San Andreas Fault, and 13 ± 2 km locking depth). These values are in close agreement with block modeling results using GPS velocities (d'Alessio et al., 2005). Because we had no initial information about the asymmetry or compliant fault zone properties, we chose uniform priors for these parameters. The MCMC algorithm was then used to generate posterior probability distributions for each parameter, including maximum posterior probability values and uncertainty estimates. We also analyzed the trade-offs between parameters in each model.

For each study area, we used the Bayes Factor to select the best of the three candidate models in a Bayesian framework (Kruschke, 2015). This technique compares a model $M1$ to a different model $M2$ by calculating the likelihood of producing the observed dataset under

each model. The Bayes Factor, K, is defined as the ratio of the probabilities of observing the data under each model:

$$K = \frac{\int Pr(\theta_1|M1)Pr(D|\theta_1, M1)d\theta_1}{\int Pr(\theta_2|M2)Pr(D|\theta_2, M2)d\theta_2}$$

K is computed as an integral over the entire parameter space, θ, of each model, thus imposing a natural penalty on more complex models with larger parameter spaces. A common interpretation of the Bayes Factor is that the data shows "substantial" support for Model 1 when the Bayes Factor is greater than 3, and "substantial" support for Model 2 when the Bayes Factor is less than 1/3 (Jeffreys, 1961). A Bayes Factor of 1 shows that the two models are equally probable.

2.4 Results

2.4.1 Black Mountain Modeling Results

The fault-parallel GPS velocities for the Black Mountain dataset are shown in Figure 2.3a, together with the modeling results for each candidate model of deformation. Across the 12 km of fault-perpendicular distance spanned in this dataset, we see a fault-parallel velocity change of about 5 mm/year. The fault-perpendicular velocities for these GPS data are all less than 1 mm/year and show no systematic trend. The SAF is located at $x = 0$ in Figures 2.3a and 2.3b.

When we search for best-fitting model parameters for this dataset using the MCMC approach, we find preferred values for locking depth and slip rate at about 13 km and 17 mm/year (Figure 2.4) under the homogeneous elastic half-space model. The posterior probability distributions for both parameters are in strong agreement with the prior distributions from UCERF-3. There is a trade-off between slip rate and locking depth (Figure 2.4, lower left), which is a common feature that Lisowski et al. (1991) and others have noted in the problem of slip rate and locking depth estimation from geodetic data, especially in the near-field.

The results of the modeling using an asymmetric arctangent model were very similar to the results of the pure arctangent model. In our modeling efforts, the preferred values for the asymmetry parameter were always very close to 0.5, indicating that this GPS dataset does not support a contrast in shear modulus across the fault zone. Furthermore, the asymmetry coefficient does not have any strong trade-offs with the other parameters. This model does not provide substantially better fits to the data than the homogeneous elastic half-space model.

Finally, the results of the CFZ model are shown in the posterior distributions of Figure 2.5. This model produced best fitting slip rates of about 16 mm/year and best fitting locking depths of about 14 km, as shown in the black histograms. The preferred values for compliance contrast μ_c of the fault zone are between 0.6 and 1, and the width of the CFZ is poorly constrained by the current data.

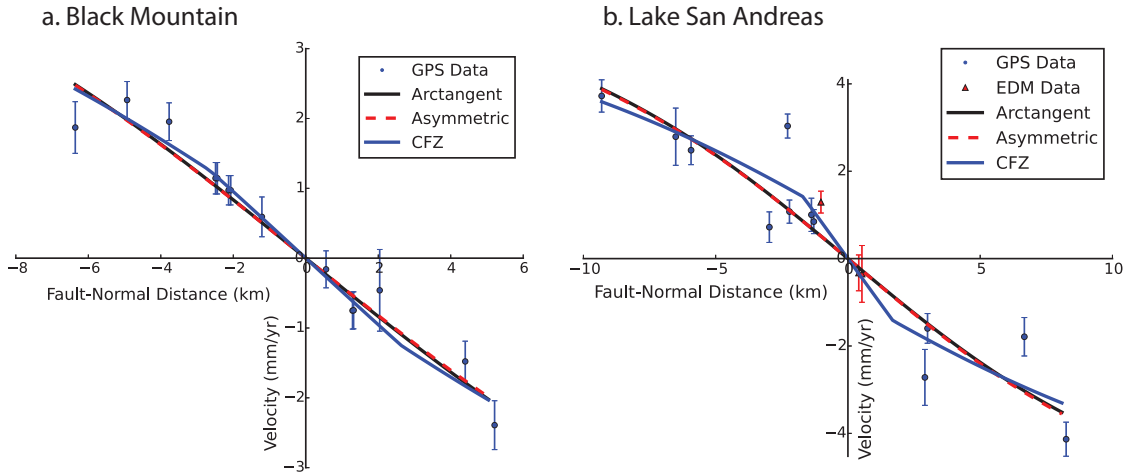

Figure 2.3: a) Black Mountain fault-parallel (N39°W) GPS velocities with one-sigma confidence intervals and best-fitting candidate models. The arctangent model is shown in a solid black line; the asymmetric model, which produced very similar results to the arctangent model, is shown in a dashed red line; and the CFZ model is shown in solid blue. b) Lake San Andreas fault-parallel GPS and EDM (N35°W) velocities with one-sigma confidence intervals. The solid and dashed curves show the best-fitting candidate models for the geodetic dataset.

The poor constraints on the width of the CFZ (lower plots in Figure 2.5) are in part due to the fact that most of the preferred values for the normalized elastic modulus of the fault zone are close to 1. When the rigidity in the fault zone is relatively high, such as in these models, the fault zone deforms much like a homogeneous elastic half-space regardless of the width of the CFZ. In this case, the width of the fault zone has little effect on the resulting deformation.

2.4.2 Lake San Andreas Modeling Results

For Lake San Andreas, the fault-parallel GPS velocities and the three best-fitting candidate models are shown in Figure 2.3b. This dataset, which spans 18 km of fault-normal distance, shows a fault-parallel velocity change of about 8 mm/year. All GPS measurements except one show fault-perpendicular velocities less than 1 mm/year with no systematic patterns. Station SERR shows a fault-perpendicular velocity of 1.3 mm/year (see Discussion section for more on this measurement).

Figure 2.6 depicts the slip rate and locking depth results under the arctangent model. The preferred parameter values for this model were slip rates of about 17 mm/year and locking depths of about 11 km, which is shallower than the UCERF-derived prior distribution centered at 13 km (shown by the red curve). This is also shallower than the depth extent of microseismicity in the area (about 14 km; see Figure 2.8).

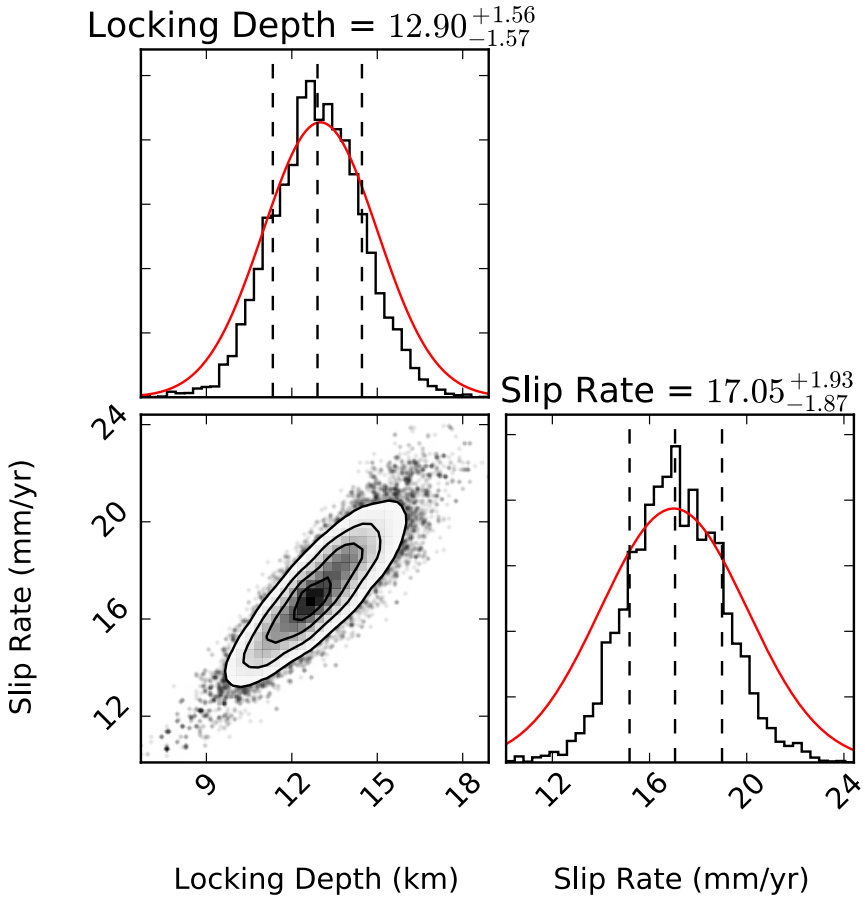

Figure 2.4: Results of arctangent (homogeneous elastic half-space) modeling at Black Mountain. The black histograms show posterior probability distributions for the slip rate and locking depth, with the dashed lines indicating the one-sigma (68%) error bounds on each parameter. The red curves show the prior distributions derived from UCERF-3 (13 ± 2 km for locking depth and 17 ± 3 mm/year for slip rate). The lower left plot shows the tradeoff between slip rate and locking depth. The contours on the trade-off diagram show the joint probability distribution, delineating regions with 11%, 39%, 68%, and 86% of the maximum probability value.

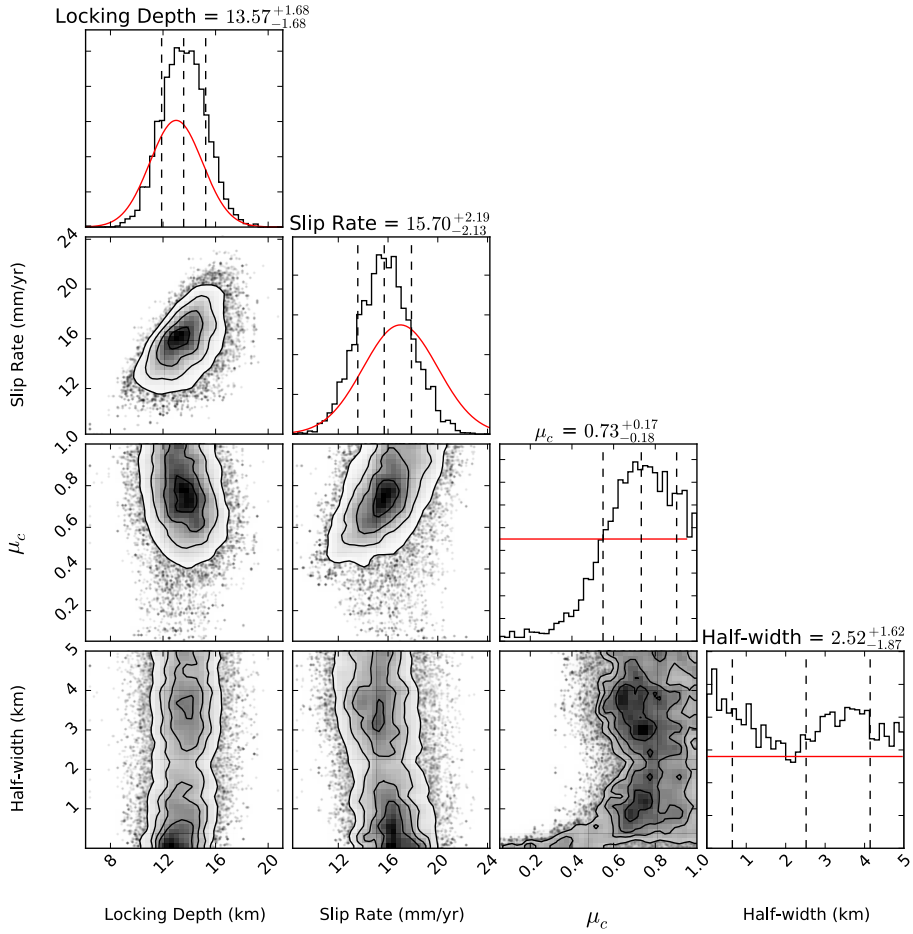

Figure 2.5: Results of CFZ modeling at Black Mountain. The black histograms show posterior probability distributions for the slip rate, locking depth, contrast in shear modulus, and half-width of the CFZ, with the dashed lines indicating the one-sigma (68%) error bounds on each parameter. The red curves show the prior distributions, derived from UCERF-3 models or otherwise assumed to be uniform. The lower plots show tradeoffs between the various parameters.

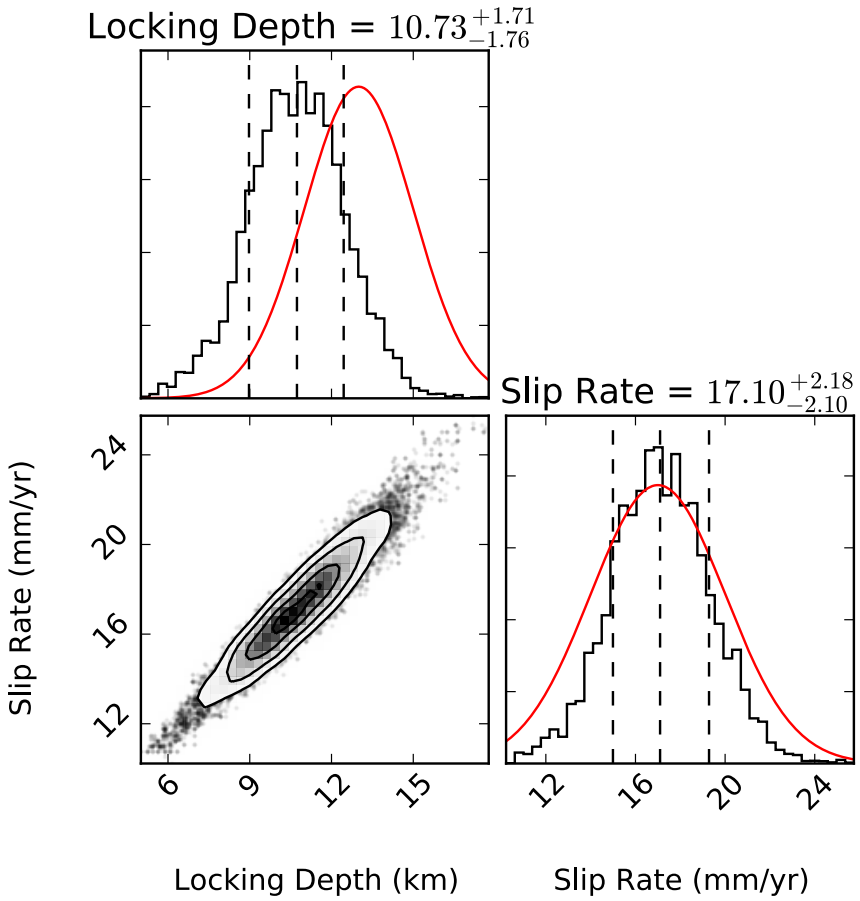

Figure 2.6: Results of arctangent modeling at Lake San Andreas. The black histograms show posterior probability distributions for the slip rate and locking depth. The red curves show the prior distributions derived from UCERF-3. The lower left plot shows the tradeoff between slip rate and locking depth.

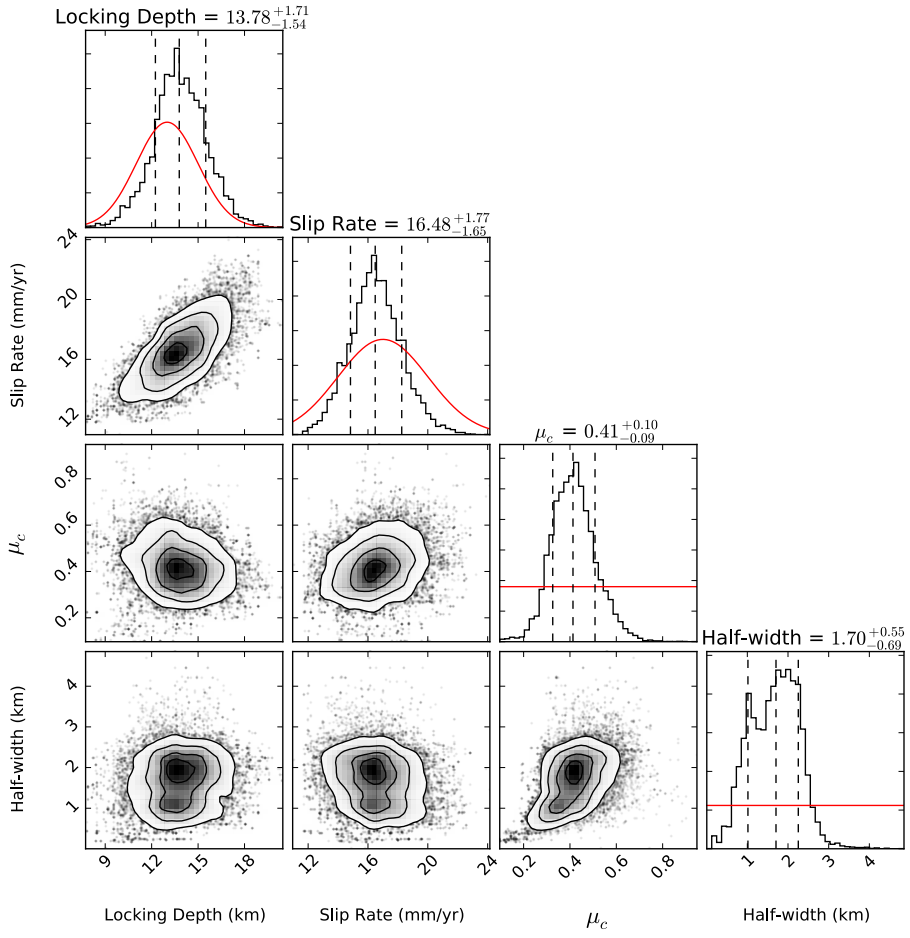

Figure 2.7: Results of CFZ modeling at Lake San Andreas. The graphs are similar to Figure 5, but for the Lake San Andreas dataset. The prior distributions chosen for each parameter are shown in red.

Like the Black Mountain dataset, the Lake San Andreas dataset did not provide any convincing evidence for asymmetry in the elastic modulus across the fault. The results of this model produced asymmetry values near 0.5, resulting in nearly identical results to the homogeneous half-space model.

The CFZ modeling at Lake San Andreas (Figure 2.7) indicates a best-fit shear modulus that is reduced in the fault zone compared to the surrounding rock. The best fitting slip rates of about 16 mm/year and locking depths of about 14 km are similar to the posterior distributions for slip rate and locking depth from the Black Mountain dataset, but the CFZ parameters are quite different. The preferred values for the compliance ratio of the fault zone μ_c are about 0.4, and the half-width of the CFZ is constrained between 1 and 2.25 km, with highest probability values around 1.7 km. The inferred total width of the CFZ is 3.4

Study Area	Model 1	Model 2	Bayes Factor	Interpretation
Black Mountain	Arctangent	Asymmetric	12.711	Strong preference for Arctangent
Black Mountain	Arctangent	CFZ	7.462	Strong preference for Arctangent
Lake San Andreas	Arctangent	Asymmetric	18.152	Very strong preference for Arctangent
Lake San Andreas	Arctangent	CFZ	0.002	Very strong preference for CFZ

Table 2.1: Summary of Bayes Factor comparisons.

+1.1/-1.4 km.

2.4.3 Model Comparisons

For each study area, we compared the arctangent model to the asymmetric and CFZ models using the Bayes Factor (Table 2.1). For Black Mountain, we found that the two-parameter arctangent model was able to explain the data as well as the alternative three-parameter (asymmetric) or four-parameter (CFZ) models, and that the Bayes Factor was substantially greater than 1 in each comparison. We would expect such a result because the three models only produce slightly different fits (Figure 2.3a), and the Bayes Factor, when given similar alternatives, tends to select the simplest model.

On the other hand, for Lake San Andreas, the CFZ model was strongly preferred over the arctangent model, as shown by the Bayes Factor for this comparison being much less than 1. The asymmetric model was again not the preferred choice for explaining the data.

2.5 Discussion

The major result of our analysis is that geodetic measurements support the presence of a CFZ at Lake San Andreas, but provide little support for a CFZ at Black Mountain. These results are somewhat different from the results of Chen and Freymueller (2002), who previously investigated the SAF and found geodetic evidence for CFZs at both of these locations. The values from Chen and Freymueller (2002) are presented in terms of a single shear strain rate measured by EDM and assumed to be representative of the entire fault zone. For straightforward comparison with their work, we converted our GPS velocity profiles into shear strain rates. We collected all fault-parallel velocities within 3 km of the fault, where the shear strain rate is 95-100% of the peak shear strain rate (utilizing 9 GPS/EDM velocities in each region). We computed the shear strain rate from the slope of a linear trend fit to the GPS profile using weighted least squares.

At Black Mountain, we find shear strain rates that are near the low end of the one-sigma confidence intervals presented in Chen and Freymueller (2002). The previous study reports a shear strain rate of 0.316 $\pm$ 0.06 microstrain per year, while we find lower shear strain rates of 0.236 $\pm$ 0.05 microstrain per year. As Chen and Freymueller (2002) noted, we would expect about 0.208 microstrain per year from a homogeneous half-space (assuming

reasonable values of 17 mm/year slip rate and 13 km locking depth). Our measurements are much closer to this value than the previous study's. It seems that GPS measurements collected over the last 20 years refine our picture of SAF deformation at Black Mountain to one with lower strain rates. This shift is likely due to an improvement in data quality and coverage rather than a temporal change in slip rate or locking depth.

At Lake San Andreas, the EDM measurements from Chen and Freymueller (2002) showed high shear strain rates of 0.366 ± 0.095 microstrain per year, and our measurements are in very close agreement (0.340 ± 0.09 microstrain per year). The Bayes Factor analysis shows that a CFZ model is strongly preferred over a homogeneous half-space model in order to explain the geodetic data.

The physical parameters we infer for the CFZ at Lake San Andreas, including a CFZ width of about 3.4 +1.1/-1.4 km and a 60% reduced elastic modulus, are similar to other geodetically inferred CFZs in the literature. For example, Hamiel and Fialko (2007) find CFZs of approximately 2-3 km in width and 60-70% reductions in elastic modulus for faults in the North Anatolian Fault system. Fialko (2004) finds compliant zones around the Calico and Pinto Mountain Faults in the Mojave Desert characterized by widths of 2 km and 50% reductions of elastic modulus. Such CFZs may be common for crustal faults with extensive damage sustained over many earthquake cycles, but more research is required to characterize these zones around other major faults.

The introduction of a CFZ into the deformation modeling at Lake San Andreas places the geodetically inferred locking depth at about 14 km depth, whereas modeling with an elastic half-space model results in a shallower locking depth of about 11 km (Figure 2.6 and Figure 2.7). The 14 km locking depth at Lake San Andreas is more closely aligned with the depth extent of local microseismicity, shown in Figure 2.8 from the double-differenced catalog of Waldhauser and Schaff (2008a). At Black Mountain on the other hand, small earthquakes are observed to about 12 km, which is already close to the inferred geodetic locking depth under the homogeneous half-space model (13 km in Figure 2.4). The addition of a CFZ into the model is not necessary to match the depth of microseismicity. We note that the depth of microseismicity at our study areas is likely a useful but not definitive indication of the true locking depth. The geodetic locking depth of a fault need not always agree with the seismogenic depth, which may undergo variations throughout the earthquake cycle (Jiang and Lapusta, 2016). However, Smith-Konter et al. (2011) found that on the southern SAF, the geodetic and seismogenic locking depths most often agree to within 2 km. With a CFZ model at the Lake San Andreas, we find agreement at or below this level.

At both Lake San Andreas and Black Mountain, we find that the asymmetric half-space model does not provide a better fit to the data than the simple arctangent model. This finding is not surprising given that we consider mostly near-field rather than far-field geodetic data, making our analysis less sensitive to asymmetry parameters simply due to the geometry of our networks (Le Pichon et al., 2005). In order to more thoroughly characterize the possible asymmetries in elastic parameters on the San Francisco Peninsula, we would need to obtain more geodetic data far to the east and west of the San Andreas Fault and construct a larger-scale model that includes nearby faults and tradeoffs with slip rates on

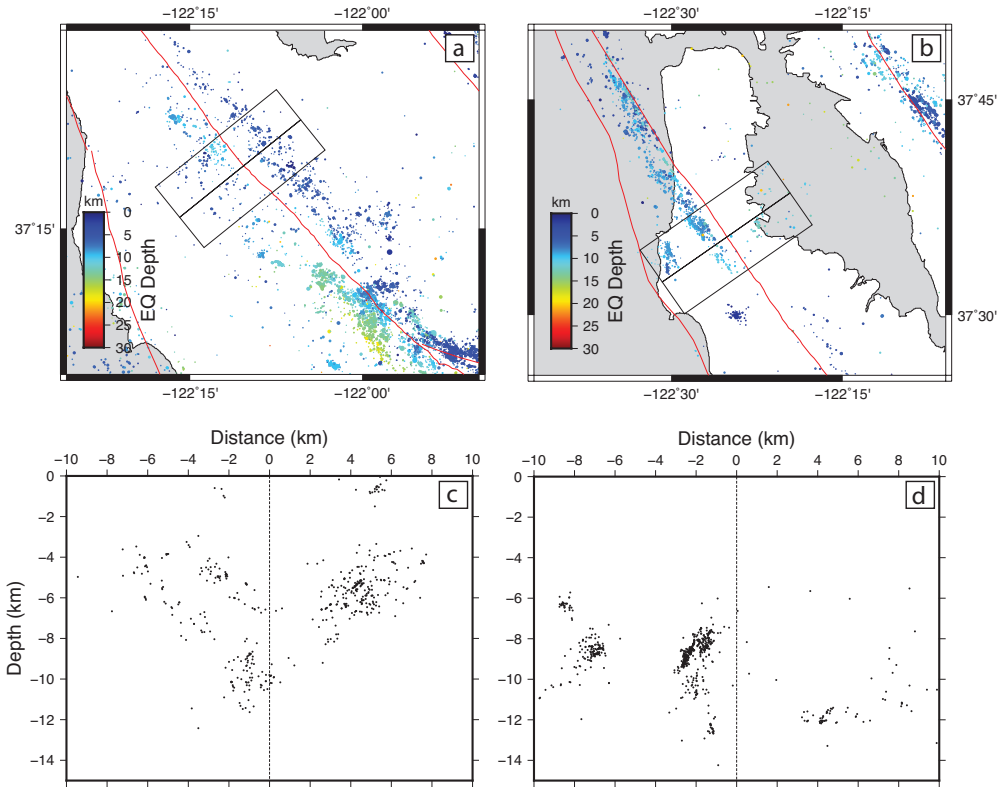

Figure 2.8: Microseismicity at Black Mountain (a) and Lake San Andreas (b). Figures c and d show the profiles of microseismicity with depth drawn across each field site. The seismicity data is from the double-differenced catalog (1984-2015) accessed through the Northern California Earthquake Data Center. Mean 95% relative location errors in the double-differenced catalog are 0.06 km in the vertical and 0.04 km in the horizontal.

those faults. In one larger-scale model (d'Alessio et al., 2005), the residuals show no obvious asymmetry, suggesting that the effects of asymmetric elastic heterogeneity in this region may be small.

Even with our relatively dense dataset of near-field measurements, the specific placement of GPS benchmarks still somewhat limits our ability to infer fault zone properties and kilometer-scale features. With only 10-15 GPS benchmarks at each field site, we are subject to effects from potential outliers and small sample sizes. For example, the Lake San Andreas dataset has a station (SERR, located about 2.2 km west of the SAF in Figure 2.6) that appears to have an unusually high fault-parallel velocity. This campaign measurement is based on one observation in 1997 and one observation in 2015, so it is possible that measurement errors at either epoch could have affected the velocity. However, earlier EDM measurements also show this benchmark moving unusually fast in the fault-parallel direction, with the GPS

velocity 0.8 mm/year faster than the EDM measurement. Non-tectonic explanations for the velocity could include site disturbances or landsliding beneath the benchmark, but we did not see evidence for that in the field (the benchmark was in good condition at the top of a hill). Therefore, because we lacked field evidence to correct the motion of the benchmark, we chose to include this data point in our modeling efforts rather than exclude it outright. Removing this data point from our parameter estimation resulted in approximately the same estimates for CFZ width, rigidity, locking depth, and slip rate, but with lower significance. With a denser spacing of geodetic measurements in the future, we could avoid potential biases from such data points, which might include non-tectonic signals we are otherwise unable to separate from the fault-related deformation.

Data from Interferometric Synthetic Aperture Radar (InSAR) may be able to generate the desired dense profiles of deformation in the future. To gain higher spatial resolution, we analyzed the available InSAR data from Chaussard, Bfffdfffdrgmann, et al. (2015) for evidence of CFZ-related localization of deformation. This estimate of fault-parallel velocities is derived from InSAR alone with scenes selected to maximize coherence over the Santa Clara Valley, so it is not adjusted to optimize for the specific velocity fields of our study regions. Nonetheless, the InSAR data generally shows very good agreement with the GPS data in both regions (Figure 2.9). The data is limited to the west of the SAF due to decorrelation from vegetation, but is more coherent in the populated areas east of the fault. We were unable to directly resolve features as subtle as CFZs in the InSAR data for either field area. The deformation signals that indicate the presence of a CFZ around the SAF are about 1mm/year in magnitude, which is the same order as the scatter in the InSAR data. Further work, including with future InSAR missions that have L-band measurements with shorter repeat times, may be able to help resolve CFZs with InSAR in this and other regions in the future.

We note that the MCMC analysis and the Bayes Factor comparison between the candidate models provide a useful framework for distinguishing between models, but do not address the assumptions in those models that may be fundamentally wrong. For example, we do not model off-fault inelastic deformation, which may play a role in this region given the presence of off-fault microseismicity at both study areas (Figures 2.8c and 2.8d). Lindsey, Fialko, et al. (2014) suggest that a fault's tectonic setting, for example within a restraining or releasing bend, can influence the fault's style of off-fault deformation and localized surface creep. In their work, releasing bends are observed to have more off-fault deformation than restraining bends. At Lake San Andreas, located along a releasing bend of the SAF, the degree of off-fault deformation from either folding or distributed brittle faulting is an important question to address in future models. However, it is difficult to address with the currently available GPS and InSAR data. With ever-increasing quality and spatial density of InSAR data, especially west of the SAF in highly vegetated areas, we hope to address these important questions in future work.

A related factor that we do not model in this work is a dipping SAF. Studies such as Lindsey and Fialko (2013) show that the dip of a fault in an elastic half-space can affect the geodetically inferred slip rate and locking depth, and Fialko (2006) shows that the elastic

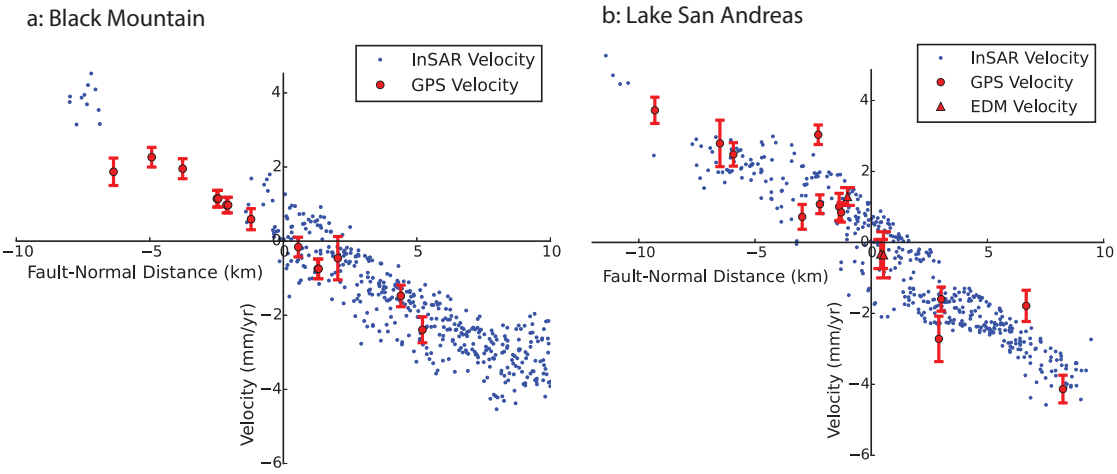

Figure 2.9: GPS/EDM and InSAR velocities at Black Mountain (a) and Lake San Andreas (b). InSAR data are from Chaussard, Bfffdfffdrgmann, et al. (2015), where velocities are obtained from ascending and descending satellite viewing geometries. The line-of-site velocities are projected into the horizontal assuming that the horizontal component is only due to fault-parallel movement.

asymmetry parameter inferred across a fault and the dip of the fault trade off with one another. The location of the CFZ relative to the surface trace and the deep dislocation may also have effects on modeled deformation. While fault dip is an important factor in modeling geodetic data, we suggest that the effects of fault dip in these two study areas are probably small. There is seismicity away from the surface trace of the SAF in both study areas, but Zoback et al. (1999) find that these events have dip-slip mechanisms and are likely related to off-fault seismicity rather than the main SAF. A number of tomographic studies also find that the SAF is a steeply dipping to vertical feature in both study regions (Parsons and Zoback, 1997; Thurber et al., 2007).

We also do not model shallow creep on the SAF, but we consider this unlikely to be a major factor on the SAF due to the lack of creep detected on creepmeters just north of Lake San Andreas (Lienkaemper et al., 2014), the high interseismic coupling estimated in UCERF-3 (Field et al., 2014), and the lack of localized microseismicity on the fault.

The results of our study have implications for how CFZs form over the lifetimes of crustal faults. In the context of earlier studies on CFZs along the northern SAF (e.g., Chen and Freymueller (2002) and Jolivet et al. (2009)), our results suggest that there is strong variability in fault zone structure within the San Francisco Bay Area. From south to north, there is little to no evidence for a CFZ at Black Mountain, strong evidence at Lake San Andreas, little evidence at Point Reyes, and strong evidence at Bodega Bay, just 30 km north of Point Reyes. Our data at the two southern field sites allows us to speculate on what factors might control the development of these features in some places and not others.

Based on the data at Black Mountain and Lake San Andreas, we suggest that fault

lithology is an important factor in CFZ formation, perhaps even more important in this case than fault age or cumulative displacement. At Lake San Andreas, although there is only 23 km of cumulative fault displacement on a relatively young branch of the SAF, there is evidence for a well-developed CFZ. A CFZ is made of extensively damaged rocks; thus, the lithology of the fault zone, and specifically how the rocks sustain damage, should play a major role in CFZ formation. The lithology of the Lake San Andreas region (Franciscan rocks adjacent to other Franciscan rocks) may play a large role in determining the type of CFZs we infer from geodetic data. In contrast, Black Mountain is a more mature fault zone bounded on the west by rigid Salinian rocks, but it does not display evidence for a CFZ. A recent study on post-seismic deformation and afterslip in northern California (Floyd et al., 2016) has also found evidence that changes in fault behavior can be correlated with first-order changes in fault lithology. More research is needed to understand the effects of lithologic contrasts on fault zone development and behavior.

The tectonic setting may also play a role in the type of damage sustained by the fault zone. In our study areas, the transpressional region at Black Mountain shows less evidence for a CFZ than the transtensional section near Lake San Andreas. The morphology of the SAF at the transtensional region, where we infer the presence of a CFZ, includes a low-lying 1-2 km wide "rift valley" with two lakes, which could reflect an easily eroded damage zone surrounding the fault. The reduction in normal stress associated with the transtensional regime at Lake San Andreas could also play a role in the extent of damage structures and the resulting topographic expression of the fault.

Our study of fault zone properties has potential implications for the coseismic behavior of faults. For example, Dolan and Haravitch (2014) show that the degree of localized surface slip during strike-slip earthquakes is correlated with the structural maturity of faults. They find a relationship between the cumulative displacement on a fault and the amount of distributed slip or "shallow slip deficit" during earthquakes. Our results imply that cumulative displacement may be only one of several factors that define fault maturity, with fault lithology and tectonic setting also playing a significant role.

Recently, Huang et al. (2016) reported a possible connection between faults with CFZs and faults that can sustain supershear ruptures. In light of this, our results are particularly interesting given geodetic and seismic evidence that the 1906 earthquake, which ruptured at both of our study areas, may have been a supershear rupture along at least some of its length (Song et al., 2008). Further observational and theoretical studies are required in order to better understand the connection between the fault zone damage structures in the San Francisco Bay Area and the types of ruptures they can sustain.

2.6 Conclusion

Using new geodetic measurements, we infer the presence of a compliant fault zone around the northern SAF at Lake San Andreas, characterized by a width of about 3.4 +1.1/-1.4 km and a 60% reduction in shear modulus; we also infer a slip rate of about 16 mm/year and

locking depth of 14 km (Materna and Bürgmann, 2016). However, we do not find evidence for a similar CFZ feature at Black Mountain. We find that the best-fitting model for the Black Mountain GPS data contains a homogeneous elastic half-space with the SAF slipping at about 17 mm/year and locked to 13 km depth.

This result, highlighting two nearby but lithologically different segments of the SAF, suggests that fault lithology may influence the formation of CFZs in this region. However, questions remain about the distribution and characteristics of fault zones in the larger SAF system and on other faults. In order to more fully understand CFZs in northern California and variations in CFZ properties along faults, further geodetic measurements are necessary. We also suggest that other geophysical methods, including seismic studies of fault zone guided waves (e.g., Cochran et al. (2009)), are needed to characterize the fault zones of the northern SAF. Given that geodetic data suggests the presence of a CFZ at Lake San Andreas, a study of this kind at Lake San Andreas may be a promising avenue for future work on CFZs.

Chapter 3

Aseismic Transform Fault Slip at the Mendocino Triple Junction From Characteristically Repeating Earthquakes

Published as: Materna, K., T. Taira, and R. Bürgmann (2018), Aseismic transform fault slip at the Mendocino Triple Junction from Characteristically Repeating Earthquakes, Geophysical Research Letters, 45, doi: 10.1002/2017GL075899.

3.1 Abstract

The Mendocino Triple Junction (MTJ), at the northern terminus of the San Andreas Fault system, is an actively deforming plate boundary region with poorly constrained estimates of seismic coupling on most offshore fault surfaces. Characteristically repeating earthquakes provide spatial and temporal descriptions of aseismic creep at the MTJ, including on the oceanic transform Mendocino Fault Zone (MFZ) as it subducts beneath North America. Using a dataset of earthquakes from 2008 to 2017, we find that the easternmost segment of the MFZ displays creep during this period at about 65% of the long-term slip rate. We also find creep at slower rates on the shallower strike-slip interface between the Pacific plate and the North American accretionary wedge, as well as on a fault that accommodates Gorda subplate internal deformation. After a nearby M5.7 earthquake in 2015, we observe a possible decrease in aseismic slip on the near-shore MFZ that lasts from 2015 to at least early 2017.

3.2 Introduction

Seismic coupling on many faults is known to be spatially and temporally variable, but what controls seismic coupling remains an open question in tectonics (Avouac, 2015). As a result of variations in seismic coupling, fault segments may creep aseismically as a mechanism of moment release at any stage of the earthquake cycle. Factors proposed to influence the creeping behavior of faults include the frictional properties of fault zone rocks, loading rate, temperature, fault surface geometry, and pore fluid pressure (Scholz, 1998; Avouac, 2015; Harris, 2017). Determining spatiotemporal variations in creep rates on a variety of faults and in many tectonic settings is key to approaching the general question of factors promoting creeping fault behavior.

Oceanic transform faults are one class of faults that may give insight into fault creep processes (Abercrombie and Ekström, 2001). In contrast to continental faults, oceanic transform faults juxtapose relatively homogeneous lithosphere, making them simpler geologic systems in which to study creeping faults. Research suggests that oceanic transform faults are especially likely to display creep due to the presence of fluids in the crust and the hydration of ultramafic minerals in the mantle (Boettcher and Jordan, 2004; McGuire, Boettcher, et al., 2005; Frohlich and Wetzel, 2007). Hydrated minerals such as serpentine and talc contribute to velocity-strengthening frictional behavior, and the presence of fluids may promote creep by reducing the effective normal stress on faults and enhancing pressure solution creep (Harris, 2017). Boettcher and Jordan (2004) evaluate a global data set of historical seismic moment release along 65 oceanic transform faults and determine an average seismic coupling coefficient (ratio of seismic to total slip above the 600°C isotherm) of 0.15 $\pm$ 0.05. Evidence of earthquake swarms, foreshock sequences, and dynamically triggered seismicity on oceanic transforms also suggests that creep on these systems may be highly time-dependent (McGuire, Boettcher, et al., 2005; Cattania et al., 2017).

In northern California, the Mendocino Fault Zone (MFZ) provides an opportunity to study fault creep on an oceanic transform fault located close to land. This transform fault is part of the Mendocino Triple Junction (MTJ), the region where the North American plate, Pacific plate, and Gorda sub-plate meet (Figure 3.1). In this area, the Gorda sub-plate, the southern portion of the Juan de Fuca plate, subducts obliquely beneath the North American plate at a rate of about 27 mm/yr (DeMets et al., 2010). South of the MTJ, the Pacific plate moves northwest at about 51 mm/yr with respect to North America along the San Andreas fault system (DeMets et al., 2010). The Pacific plate south of the MFZ is overlain by the Vizcaino block, an over-thickened piece of crust with origins in the North American accretionary complex (Leitner et al., 1998; Henstock and Levander, 2003). Along the MFZ, the relative motion between the Pacific plate and Gorda sub-plate, determined from 0.78 Ma magnetic lineations, is about 47 mm/yr oriented west-northwest (DeMets et al., 2010). The relative motion between the three plates results in northward migration of the MTJ (Furlong and Schwartz, 2004) and internal deformation within the Gorda lithosphere (Gulick et al., 2002; Chaytor et al., 2004). In 1992, this area hosted a M7.1 mainshock with slip oriented parallel to the plate interface followed by two M6.5 aftershocks within the Gorda sub-plate

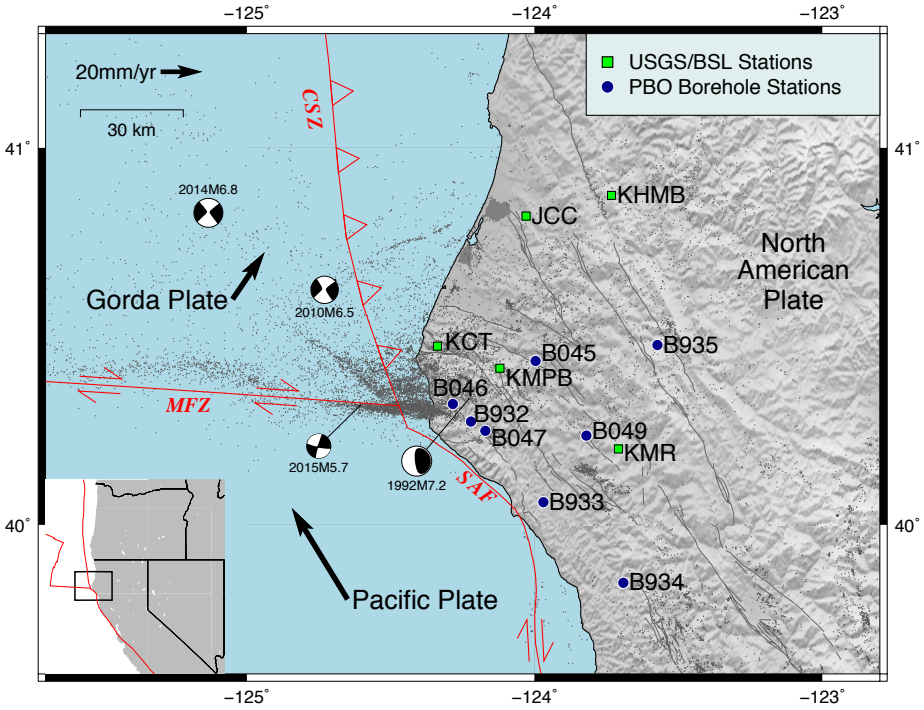

Figure 3.1: Map showing the tectonic setting of the Mendocino Triple Junction (MTJ) and the seismometers used in this study. The San Andreas Fault (SAF), Mendocino Fault Zone (MFZ), and Cascadia Subduction Zone (CSZ) are shown in red with black plate motion vectors (DeMets et al., 2010). Green squares and blue circles show the locations of seismic stations used in this study to detect CREs. The 1984-2017 background seismicity from a double-difference relocated earthquake catalog (Waldhauser and Schaff, 2008b) is shown in gray. Moment tensors extracted from the Northern California Earthquake Data Center for recent or especially large previous seismic events are also shown.

(Oppenheimer et al., 1993).

Much of the current research on fault creep relies on geodetic measurements from terrestrial and space geodetic techniques. Seafloor geodetic measurements have been used to study oceanic transform faults (McGuire and Collins, 2013), but these techniques are still prohibitively challenging. At the MTJ, we instead use characteristically repeating earthquakes (CREs) to identify fault segments with aseismic creep. These micro-earthquakes with nearly identical waveforms represent repeated ruptures of the same seismic asperity surrounded by an otherwise creeping fault zone (Nadeau and McEvilly, 1997). The local creep rate of a

fault segment can be inferred from the timing and magnitude of CREs (Nadeau and Johnson, 1998). CREs have been used to detect fault creep and estimate aseismic slip rates in a variety of tectonic settings (Nadeau and McEvilly, 2004; Chen, Nadeau, et al., 2007; Uchida and Matsuzawa, 2011; Uchida and Matsuzawa, 2013; Meng et al., 2015; Dominguez et al., 2016; Yao et al., 2017). Several examples of CREs with overlapping rupture areas have been detected along the MFZ (Waldhauser and Schaff, 2008b). Here we use this approach to identify creeping fault structures in the MTJ and explore the recent spatio-temporal distribution of aseismic slip on the MFZ.

3.3 Methods

In order to detect CREs, we use vertical component seismic waveform data from eight Plate Boundary Observatory (PBO) borehole stations (∼150-200m depth) and five surface broadband stations in the Cape Mendocino area (Figure 3.1). All waveforms have a sampling frequency of 100 Hz. The PBO borehole geophones were installed in late 2008 and provide the bulk of the data for this study. We investigate over 120,000 waveform records from 18,000 earthquakes between October 2008 and July 2017 in the Northern California Seismic Network (NCSN) catalog. Waveforms in the vertical component were extracted from the Northern California Earthquake Data Center (NCEDC) continuous data. The instrument responses were corrected to obtain velocity waveforms, and a high-pass filter of 0.5 Hz was applied to suppress microseismic noise. We select waveforms for each event from 30 seconds before the P-wave arrival to 20 seconds after the P-wave arrival.

We identify repeating earthquake pairs within this dataset based on waveform similarity. We compute the mean frequency-domain coherence for each event pair with locations less than 30 km apart across a frequency band between 0.5 Hz and a maximum of 15 Hz. For events with low signal to noise ratio (SNR), we reduce the relevant frequency band to only include the frequencies at which both events have SNR greater than 5.0. If the mean coherence across this frequency band is greater than 0.97 at two or more stations, then we determine that the event pair is a repeating pair. We then group repeating earthquake pairs into sequences that share common events (Uchida and Matsuzawa, 2013). The method employed in this study is similar to a CRE detection algorithm used for small repeating subduction events offshore Japan (Uchida, Nakajima, et al., 2009; Uchida and Matsuzawa, 2013), but with the additional requirement that the SNR>5 for each event pair. As most CREs at the MTJ are offshore and small-magnitude, this modified approach improves reliability by rejecting the attenuated or noisy parts of the seismic signal when making CRE detections.

For locating CRE sequences on maps, we average the locations from the double-differenced catalog (Waldhauser and Schaff, 2008b) where possible, but use original catalog locations in cases where no double-differenced locations were available. In all figures, each sequence is plotted as a circle if double-differenced locations were available, and as a square if no double-differenced locations were available. Example sequences are plotted in Figure 3.2.

We then estimate the slip rate of all CRE sequences that span more than one year in

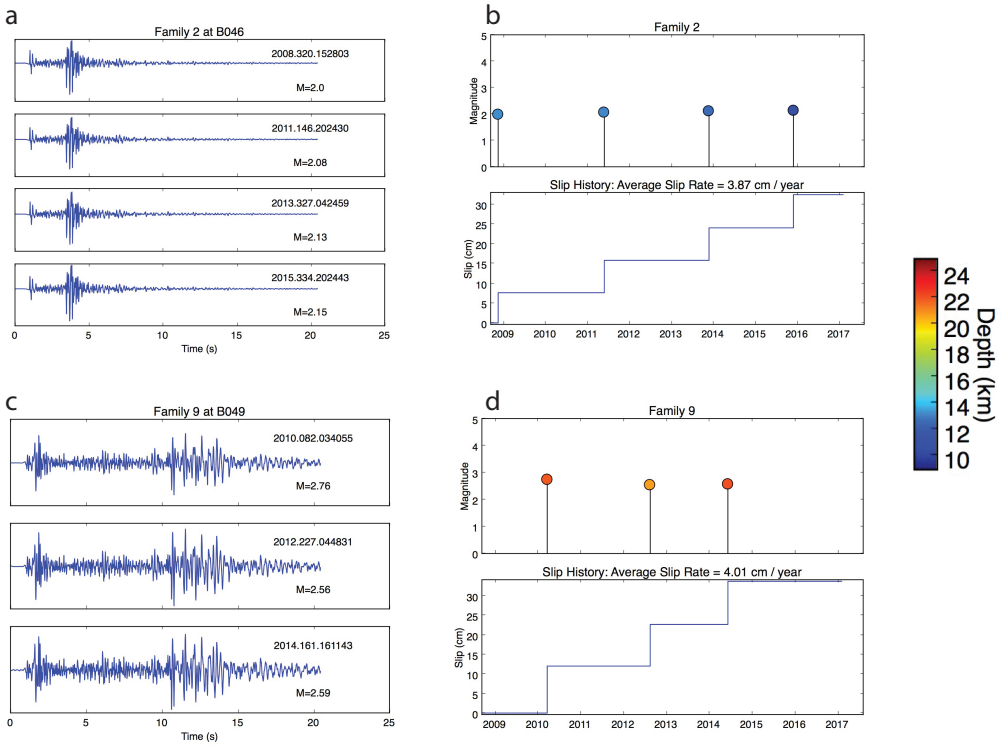

Figure 3.2: a and c) Example waveforms from two repeating earthquake families detected at the MTJ. b and d) Timing, depth and magnitude information for the earthquakes in (a) and (c). This information is used to compute average slip rate from sequences of CREs.

total duration. By removing short-lived sequences, we avoid biasing the slip rate estimates with burst-type repeaters that do not reflect the tectonic loading rate (Templeton et al., 2008). We use the empirical scaling relationship of Nadeau and Johnson (1998), derived from small repeating earthquakes in Parkfield, California, to relate the occurrence of CREs to cumulative slip history:

$$log(d) = -2.36 + 0.17log(M_0) \tag{3.1}$$

where the slip d is in cm and the moment M_0 is in dyne-cm.

Although this scaling equation is empirically calibrated for Parkfield, comparisons of geodetic and CRE-derived creep rates elsewhere suggest that this relationship holds well in different tectonic regimes around the world, such as California, Taiwan, Japan, and Tonga-Vanuatu, among others (Chen, Nadeau, et al., 2007; Uchida and Matsuzawa, 2013; Yu, 2013). Based on these existing comparisons, we make the assumption that this empirically calibrated scaling relationship sufficiently describes slip history inferred at the MTJ from repeating earthquakes. Even if this assumption is not valid, trends in CRE activity should reveal any time-dependent slip behavior at the MTJ.

3.3.1 Sensitivity of Repeating Earthquakes to Cutoff Parameters

We explored a range of cutoff criteria and studied the sensitivity of our CRE results to the choices made in the data processing steps. Our preferred detection scheme involves taking the mean coherence of the two waveforms between 0.5 Hz and a maximum of 15 Hz. However, we reduce the relevant frequency window in cases of low signal to noise ratio (SNR) to those frequencies where the SNR is greater than 5.0 for both signals. This procedure produces similar results to CRE detection using waveform cross-correlation, but detects CREs more reliably at larger distances. In our preferred scheme, repeating earthquakes must have a mean coherence greater than 0.97. By this detection scheme, we detect 78 sequences of CREs.

We computed the results for this detection scheme under each coherence cutoff between 0.90 and 0.99 (Figure 3.3). We also computed bootstrapped slip rate uncertainties for each region of interest in Figure 3.5 by randomly removing 2 sequences (from a set of typically 15 to 30 sequences), re-computing the resulting slip rate 100 times, and sampling the standard deviation of the slip-rate distribution.

For lower choices of coherence cutoff, we find that the number of CRE sequences increases, and that the quality of those sequences decreases. Reducing the cutoff criteria results in the detection of more burst-type repeaters, which are usually separated by just a few hours or days (Templeton et al., 2008), instead of long-lived CREs. Similarly, we find that increasing the strictness of the cutoff criteria reduces the average coefficient of variation (COV) of the sequences, meaning that the detected sequences occur more periodically in time rather than randomly (e.g., Chen, Bürgmann, et al., 2013). These tests suggest that the event-pairs with the strongest waveform similarity in fact represent the long-lived repeating earthquakes and not the burst-type repeating earthquakes.

Even though the number of CREs detected increases with lower cutoffs, the inferred slip rates and bootstrapped slip rate uncertainties are relatively unchanged across many choices of cutoff criteria between 0.90 and 0.99 (Figure 3.3). However, above a cutoff value of 0.97, the slip rates change and the uncertainties increase. Based on the result of this tradeoff, we chose 0.97 as the cutoff in our preferred detection scheme. This scheme allows for the detection of the most selective CRE sequences without entering the regime where slip rate estimates become highly variable.

By changing the frequency band or the statistic to summarize coherence over that frequency band (mean vs. median), we produce many possible detection schemes and corresponding CRE results. Above 15 Hz, the results are not very sensitive to the choice of maximum frequency band, although higher bands generally result in fewer detections. At lower frequency bands, we detect many undesired event pairs. Therefore, in our preferred solution, we choose a maximum of 15 Hz because it allows for the detection of many CREs in the magnitude range common at the MTJ without being so strict that it detects few events. The results are somewhat sensitive to mean vs. median coherence within the frequency band, so we choose the mean of the frequency band because it results in fewer false identifications of non-repeating events.

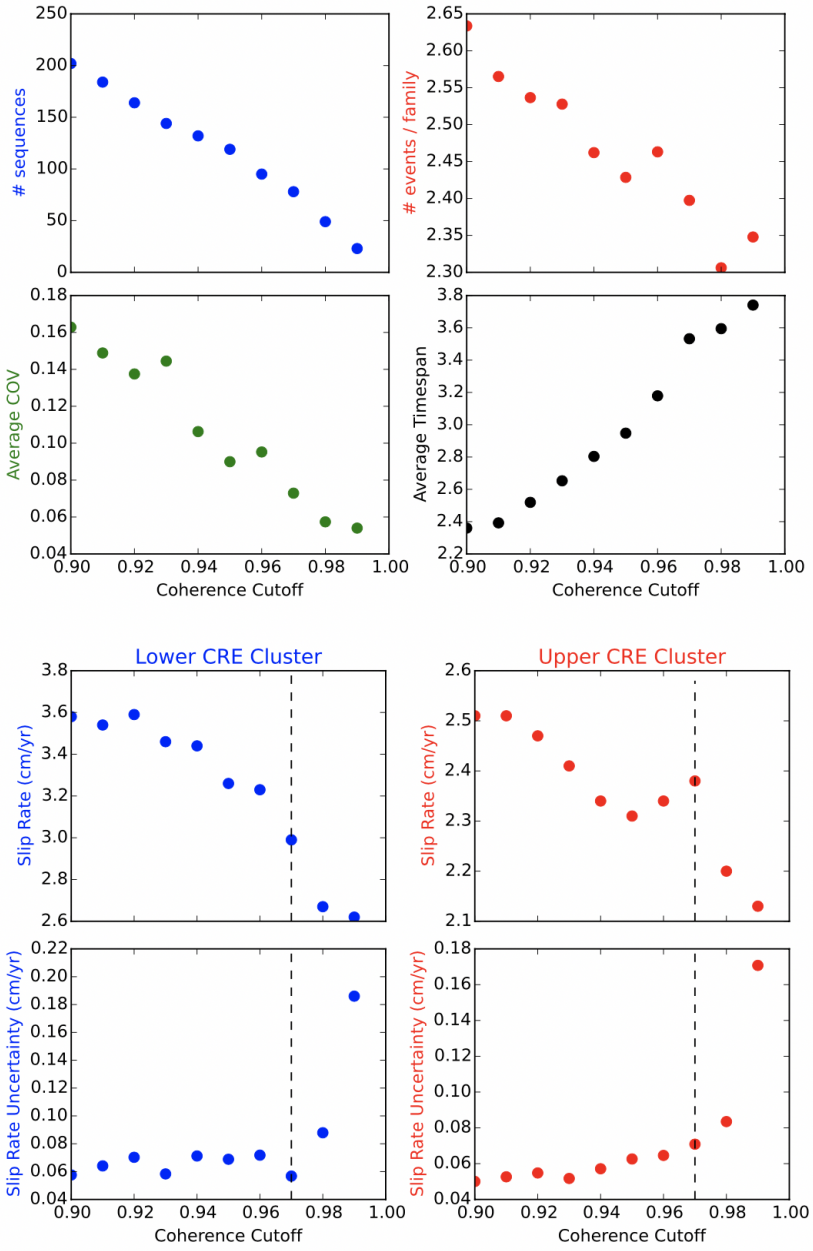

Figure 3.3: Summary characteristics of CRE detections as a function of coherence cutoff for the preferred detection scheme (mean coherence of all frequencies from 0.5 to 15 Hz with high SNR). Lower plot shows mean slip rate estimates and bootstrapped uncertainties for CRE sequences in the upper and lower clusters of Figure 3.5. The changes in values and uncertainties at a cutoff of ∼0.97 justify the selection of 0.97 as a cutoff criterion.

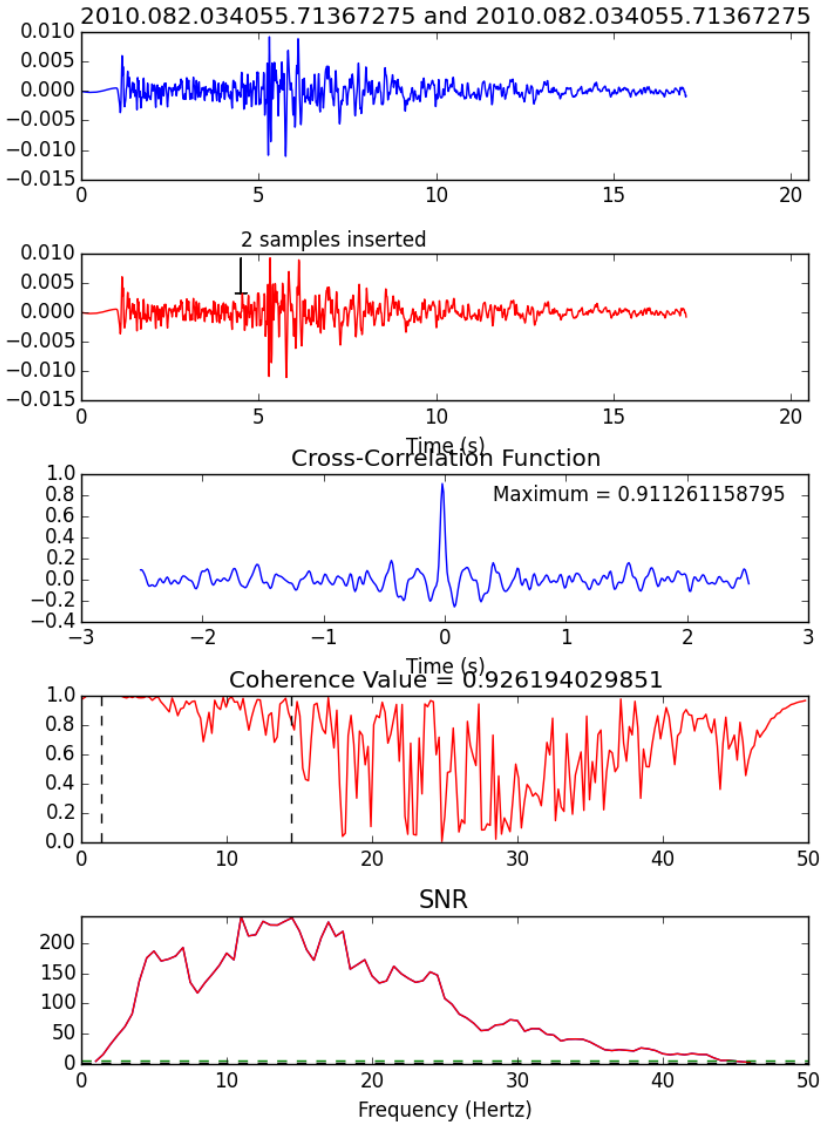

Figure 3.4: A test waveform compared to a copy of itself, but with two samples (0.02 seconds) inserted between the P and S arrivals to simulate the translation of the source patch away from the receiver by 80 meters. The coherence value is no longer above 0.97, meaning that the event pair would no longer be detected as a repeating earthquake.

The magnitudes of the CREs we detect are not sensitive to cutoff criteria; the magnitudes are almost always in the M1.5-M3.0 range, with most between M2.0 and M3.0. However,

smaller-magnitude CRE sequences may exist but are not complete in the Northern California Seismic Network catalog. According to Tormann et al. (2014), the magnitude of completeness for the near-shore MFZ is slightly below M2.

Our analysis suggests that different cutoff criteria for CRE detection may be appropriate for different tectonic settings or different levels of data coverage. For example, the magnitude range of the repeating earthquakes at a particular location may influence the appropriate frequency band required to detect CREs. We suggest that the most useful CRE detection scheme for a certain environment may not be known a priori, and may need to be determined in different areas through empirical approaches.

3.3.2 Sensitivity to CRE Relative Location

CRE analysis assumes that individual CRE sequences originate from the same source patch on a fault. In order to assess whether the CREs we detect are co-located, we performed synthetic tests on waveforms and found that the frequency-domain coherence between two waveforms is extremely sensitive to the distance between the source and receiver (related through the S-minus-P time). For test waveforms at various distances between 20 and 60 km from the receiver, we compared existing waveforms to synthetic copies of themselves, but with additional samples inserted between the P arrival and S arrival to simulate increasing the distance between the source and receiver. In all cases, inserting one or at most two samples between the P and S arrivals (whether the sample was 0.0, random noise, or a copy of the previous sample) caused the mean coherence of the waveform to drop below 0.97, meaning we would not detect the event pair as a repeater within our cutoff criterion (Figure 3.4). With our sampling frequency of 100 Hz, this shift corresponds to a change in epicentral location of approximately 80 meters, assuming 4 km/s average shear wave speed and 8 km/s average P-wave speed. As we added more samples (increasing the simulated distance between patches up to 400 m), the coherence value dropped to 0.6-0.8. It is still possible that location differences could exist in the azimuth-perpendicular direction, but we believe that we are able to distinguish these cases by requiring that the event pairs pass the repeater detection criterion at two or more stations. In our final catalog, >60% of repeating event pairs were detected at 4 or more stations, with some detected at as many as 12 stations. This analysis suggests that when we detect pairs of highly coherent waveforms at multiple receivers, with coherence at the 0.97 level or higher, we are detecting pairs of earthquakes that originate from nearly co-located source patches.

3.4 Results

3.4.1 Spatial Distribution of Repeating Earthquakes

Applying this method to northern California events west of 123.3°W, we find 83 CRE sequences, with average magnitudes between 1.5 and 3.0. Many sequences are located on a

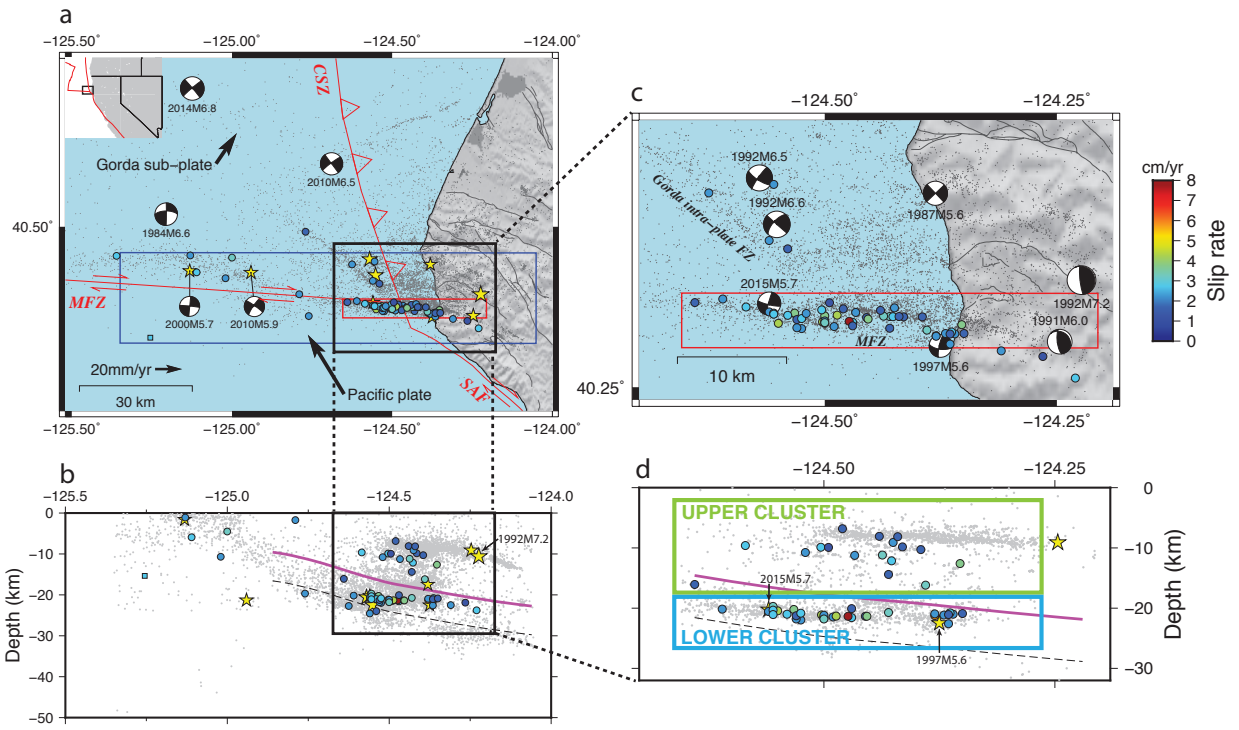

Figure 3.5: a) CREs at the MTJ, where the Mendocino Fault Zone (MFZ), Cascadia Subduction Zone (CSZ), and San Andreas Fault (SAF) intersect. The 1984-2017 background seismicity from a double-difference relocated catalog (Waldhauser and Schaff, 2008b) is shown in gray. Especially large previous seismic events are marked by their moment tensors in map view (Ekström et al., 2012), and by yellow stars on the cross sections. b) Depth profile through the blue box in (a). Each sequence is color-coded by inferred slip rate. CRE sequences with double-differenced locations are marked by circles; one sequence with only NCSN locations is shown as a square. The subduction interface model from Slab1.0 (Hayes et al., 2012; McCrory et al., 2012) is shown in magenta, with a dotted line to represent the approximate position of the Moho 7km deeper than the interface. Figures c) and d) show corresponding close-ups of the central region.

narrow and well-defined surface that trends east-west at 40.3°N (Figure 3.5a), closely aligned with the MFZ and its eastward continuation below land. In particular, the CRE sequences on this surface are separated into an upper cluster at 10-17 km depth, and a lower cluster at 18-25 km depth (Figure 3.5d). We separate these two distinct clusters of seismicity in our subsequent analysis.

The lower cluster lies below the CSZ plate interface of McCrory et al. (2012), suggesting

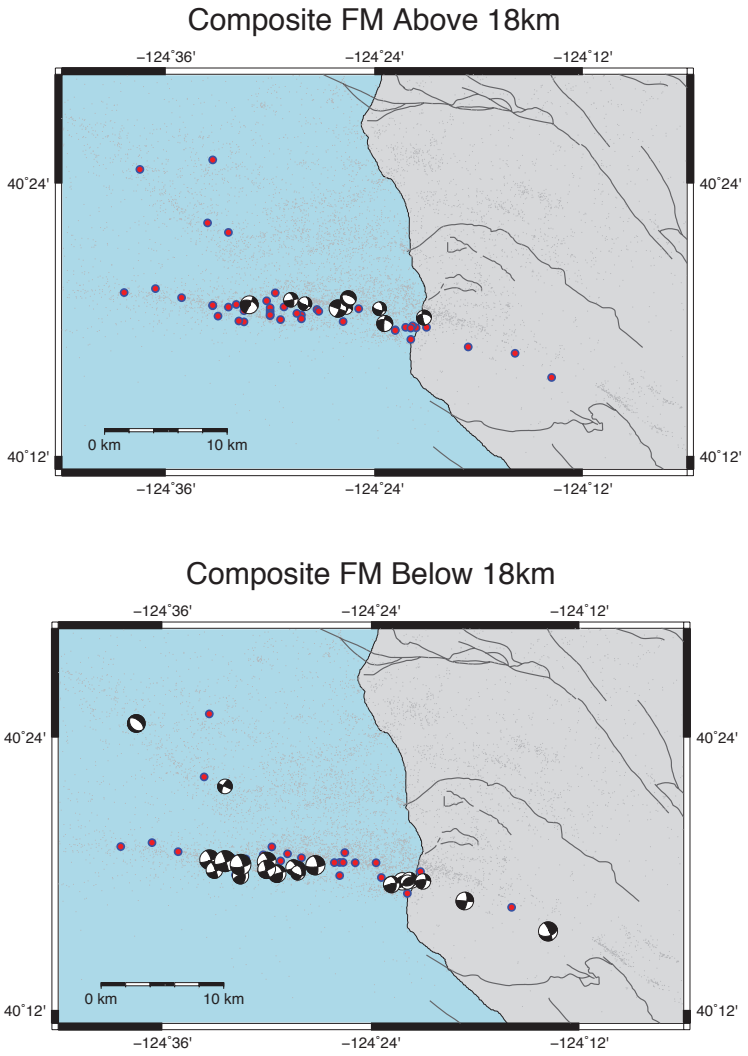

Figure 3.6: Composite focal mechanisms computed for CRE sequences in the upper cluster and lower cluster of Figure 3.5 (the regions above and below 18 km depth). These composite focal mechanisms for CREs are consistent with moment tensors for larger events in the same regions (http://seismo.berkeley.edu/∼dreger/mtmaps.html). Pink dots represent the locations of CRE sequences.

that it is located between the oceanic Pacific plate and the Gorda sub-plate. Composite focal mechanisms computed for CRE sequences in the lower cluster show overall right-lateral strike-slip movement (Figure 3.6), consistent with the moment tensors of nearby M5.6 and M5.7 earthquakes in 1997 and 2015 (Figure 3.5c).

The upper cluster (between 10 km and 17 km depth) lies above the inferred CSZ plate

interface, placing it along the North American accretionary wedge. Composite focal mechanisms for the upper cluster also show dominantly right-lateral strike slip on east-west striking nodal planes (Figure 3.6).

Outside of the narrow structure that contains most of the CREs, we detect several sequences on a northwest-southeast striking intraplate fault in the Gorda sub-plate (Figure 3.5c). These sequences are located at depths of 15-25 km. Their focal mechanisms are poorly constrained, but historical focal mechanisms for M3-M4 events on that structure show dextral strike-slip. We also detect several CRE sequences further west on the MFZ, which tend to contain larger-magnitude (M∼3) events with poorly constrained depths (Figure 3.5a). We do not detect CREs east of 124°W or on the subduction thrust.

3.4.2 Creep Rates and Time-Dependent Creep

We compute average slip rates for the upper and lower clusters on the MFZ by summing the slip inferred from each CRE and dividing by the total number of CRE sequences in each region (Nadeau and McEvilly, 2004). This technique helps to reduce some of the uncertainty in individual sequence slip rates under the assumption that the CREs are driven by spatially coherent aseismic slip. In the upper cluster (Figure 3.5d), we find 17 CRE sequences and infer an average slip rate of about 23 ± 4 mm/yr. The lower cluster contains a more active and variable set of 38 CRE sequences with an average slip rate of 29 ± 12 mm/yr over the observed time window. The average slip rate of CRE sequences west of ∼124.6°W on the MFZ is about 27 ± 3 mm/yr.

Several time-variable features of the dataset highlight differences in behavior between the upper and lower clusters. We note that the background seismicity in the two regions responds differently to two regional earthquakes (Figure 3.7). In the upper cluster, aftershock activity is observed following a 2014 M6.8 strike-slip earthquake 100 km to the northwest, while in the lower cluster, aftershock activity is observed following the nearby 2015 M5.7 event. The most notable potential slip rate variation is observed in the lower cluster surrounding the 2015 M5.7 event (Figure 3.7d). There appears to be faster slip for about 6 months before this earthquake, and two years of relative quiescence afterwards. The M5.7 earthquake occurred on the western edge of the lower cluster (Figure 3.8) and has a similar focal mechanism to many of the composite CREs. We conservatively estimate the rupture patch of this event to be about 9 km in length by 6 km wide (Wells and Coppersmith, 1994). Preliminary modeling of this event using empirical Green's functions suggests a smaller patch with a ∼6-km-long rupture and 7 MPa stress drop (Jianhua Gong, personal communication, 2017), consistent with other findings that MFZ earthquakes have higher-than-average stress drops (e.g., 5-20 MPa from Chen and McGuire (2016)). The spatial and temporal relationship between this M5.7 earthquake and the CRE sequences is shown in Figure 3.8.

3.5 Discussion

Our data show evidence for multiple robust sequences of CREs in the MTJ, which we interpret as representing aseismic slip on several fault structures between 2008 and 2017 (Figure 3.9). At 20-30 km deep, the highly active CRE sequences (Figure 3.5d, lower cluster) reflect aseismic creep between the Pacific plate and the subducting Gorda sub-plate. In this area, the background microseismicity in the downgoing slab illuminates a previously documented double seismic zone, whose layers are thought to result from dehydration embrittlement of the upper crust and the serpentinized upper mantle respectively (Yamasaki and Seno, 2003; McCrory et al., 2012). The CREs in this region appear to lie on the southern edge of the Gorda sub-plate in the depth range between the upper and lower layers of the double seismic zone (Figure 3.5b), where the downgoing slab abuts the Pacific lithosphere along the eastern extension of the MFZ (Wang and Rogers, 1994; McCrory et al., 2012).

We interpret the upper cluster of Figure 3.5d (10-17 km depth) to be above the subducting slab interface, and therefore juxtaposing the Pacific plate and overlying Vizcaino block against the accretionary wedge of the North American plate (Figure 3.9a). However, the CREs in this range have a patchier spatial distribution. Based on the sparser distribution of CREs, we infer that this part of the transform fault zone more likely contains a heterogeneous distribution of locked and aseismically slipping patches.

We do not see any CRE activity on the plate interface of the CSZ, consistent with previous estimates that it is highly coupled in this region (McCaffrey, Long, et al., 2000; Schmalzle et al., 2014). We also do not see spatial overlap between the CRE activity and the deep-seated tremor on the CSZ (Boyarko and Brudzinski, 2010; Wech, 2010), suggesting that CREs and tremor reflect separate slip processes on the shallow transform fault and the deep subduction zone respectively.

We detect several sequences of CREs on a northwest-southeast trending strike slip fault in the interior of the Gorda sub-plate (Figure 3.5c). In the last several decades, large earthquakes up to magnitude 7 have been recorded on strike-slip faults within the Gorda sub-plate (Rollins and Stein, 2010), including a 2010 M6.5 slightly north of the MTJ (Figure 3.5a). Our results suggest that for the intra-plate fault of Figure 3.5c, some of the deformation budget is also aseismic, although it is difficult to quantify how much given current data. We cannot place constraints on other faults that do not host CREs, as they may be fully locked or creeping without producing detectable CREs.

The inferred 2008-2017 average slip rate of the MFZ from repeating earthquakes is about 29 mm/yr with uncertainties of 12 mm/yr. By comparison, the expected long-term slip rate of the MFZ, derived from sea-floor spreading data in MORVEL 2010, is 44 mm/yr (DeMets et al., 2010)(Figure 3.9). Assuming this long-term velocity is representative of the loading rate, only about 30% of the total moment deficit between 18 and 28 km depth has been relieved in recorded earthquakes since 1976 (Figure 3.9b), leaving 70% of the moment deficit on the MFZ to be accounted for in another fashion, i.e., future earthquakes or aseismic slip. Although we cannot characterize the aseismic slip processes before the start of our observations, the CRE results since 2008 lead us to conclude that in recent years, aseismic

slip has accommodated a majority of the 70% remaining moment deficit on the MFZ. A caveat, however, relates to the internal deformation of the Gorda sub-plate and the non-uniform spreading rate on the Gorda ridge (Wilson, 1986; Wilson, 1989; Chaytor et al., 2004). Taking this adjustment into account, the long-term slip rate on the MFZ may vary from the MORVEL 2010 estimate, with lower slip rates in the west and higher slip rates in the east (Pollitz, McCrory, et al., 2010). Consequently, on the near-shore segment of the MFZ, we would expect a larger overall moment budget on the MFZ and a smaller aseismic contribution to the moment release.

The 2015 M5.7 earthquake shows that the MFZ, although partially creeping, also occasionally generates moderate-sized earthquakes. Estimates of the earthquake's rupture dimensions suggest that a number of CRE sequences are located near or within the rupture patch (Figure 3.8). It is possible that the true dimensions of the rupture are smaller than the estimate presented here, as the event likely had a relatively high stress drop. The cataloged aftershock sequence is widespread across the fault and does not provide immediate information about the rupture dimensions. However, it is likely that the M5.7 rupture zone coincided with at least some of the aseismic zone around the repeaters, meaning that some areas of the fault zone may have deficits to be made up by future seismic slip. The potential quiescence for the two years following the M5.7 event suggests that this event had relatively little postseismic slip. Interestingly, the possible quiescence following this event extends to CRE sequences many km away from the inferred rupture patch, in regions of the fault interface that should have experienced small Coulomb stress increases after the rupture (Figure 3.8c). This may be because many sequences happened to have events in late 2014 and early 2015, meaning they were early in their presumed seismic cycle when the M5.7 earthquake occurred (Figure 3.7d). The most recent observations suggest that many CRE sequences resumed activity again in 2017, although it is still too early to completely characterize the interactions between M5.7 event and the surrounding CRE sequences.

Our results demonstrate the value of using CREs to monitor for aseismic creep and creep transients where geodetic measurements are not readily available. Although the creep rates we infer are relatively high, they have not been previously documented because land-based geodetic techniques are not well equipped to observe aseismic slip at the offshore MTJ. To test the interseismic displacements at PBO GPS stations that would result from various seismic coupling ratios on the MFZ (Figure 3.10), we construct a back-slip dislocation model in a homogeneous elastic half-space (Okada, 1992) with an assumed shear modulus of 30 GPa. Our simple model contains 46 mm/yr of strike-slip motion along the SAF and 34 mm/yr of oblique slip on a 30-degree dipping CSZ surface from 10 to 30 km depth, consistent with more detailed dislocation models of this plate boundary zone (Schmalzle et al., 2014). We then vary the backslip rate on the MFZ from 0 mm/yr, representing 0% coupling, to 48.7 mm/yr, representing 100% coupling. We know from repeating earthquakes that the average coupling on the MFZ is intermediate between these two values.

Using this model, we find that changes in coupling on the MFZ would barely be detectable at the currently existing PBO continuous GPS stations. We find that only two GPS stations show velocity changes above 1 mm/yr as a result of changing the coupling on the MFZ from

0% to 100% (Figure 3.10). Furthermore, these calculations are upper bounds, because they assume that the contributions from interseismic coupling on the SAF and CSZ are known precisely and modeled completely with elastic dislocations, which is unlikely to be the case in the MTJ. It is thus very difficult to image slip on the MFZ using the existing network of land-based continuous GPS.

However, our findings suggest that this region may be well suited for experiments with seafloor geodesy in the future using acoustic ranging or GPS-acoustic systems (McGuire and Collins, 2013; Bürgmann and Chadwell, 2014). The fast deformation rates and high likelihood of aseismic creep make the MFZ a favorable target for these techniques, especially when integrated with constraints from seismicity data and CREs.

3.6 Conclusion

Repeating micro-earthquakes provide evidence that the MFZ, an oceanic transform fault, is creeping on average between 2008 and 2017 at about 65% of its long-term slip rate and may display small variations in creep rate over the study period (Materna, Taira, et al., 2018). This evidence of fault creep supports previous suggestions that aseismic moment release is an important mode of slip for oceanic transform systems. Surrounding a nearby M5.7 earthquake on the MFZ, we find that CRE activity may undergo a slight increase and subsequent decrease, but the decrease cannot be explained by static earthquake stress interactions alone. In addition to the MFZ, we detect shallower creep between the Pacific plate and the southern edge of the North American accretionary prism, and several persistent CRE sequences on an intra-plate fault in the Gorda sub-plate. Determining whether the slip rates inferred in this study are transient or representative of longer-term rates will require additional work on older and future datasets. In the complex deformation field of the MTJ, CRE observations can provide an important observational constraint on aseismic slip and its time-dependent variations.

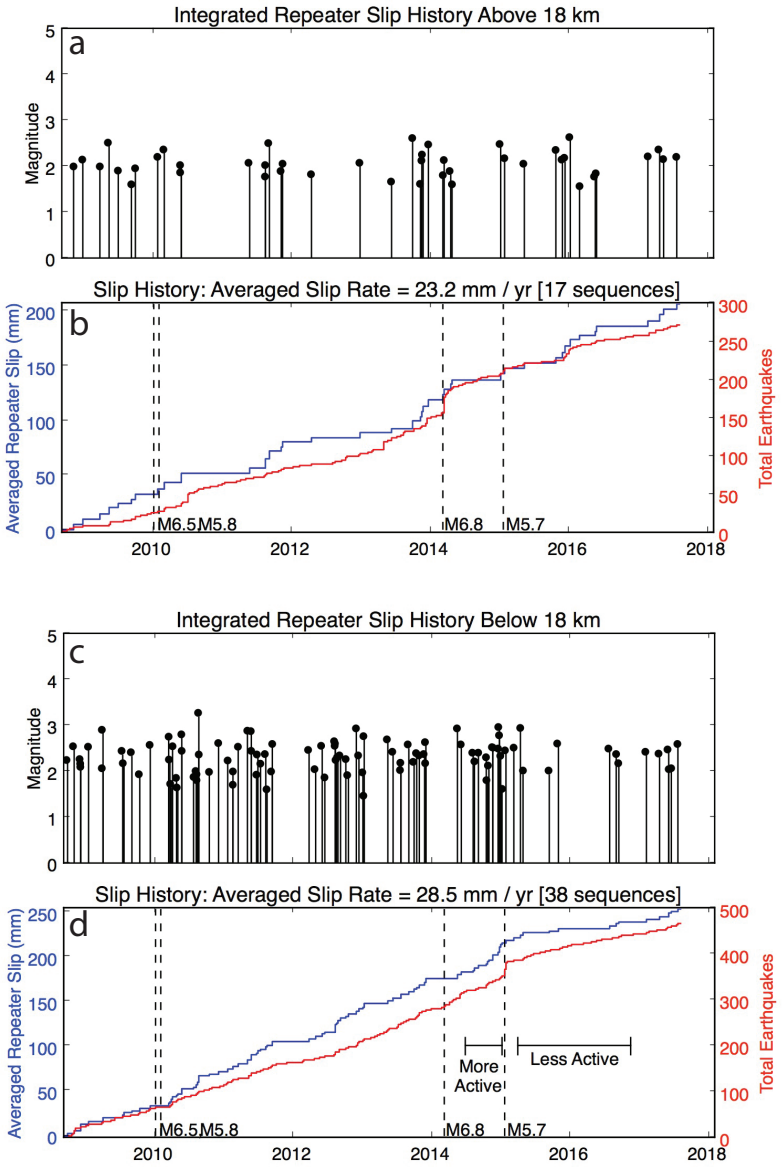

Figure 3.7: a and b) History of CRE activity in the upper cluster, 10-17 km depth (Figure 3.5d). c and d) History of CRE activity in the lower cluster, 18-25 km depth (Figure 3.5d). Blue lines represent cumulative slip inferred from CREs with equation (3.1). Black dashed lines show occurrence times of nearby moderate earthquakes (see Figure 3.5 for locations); the red curves show the cumulative number of events in the double-differenced catalog within the regions of interest.

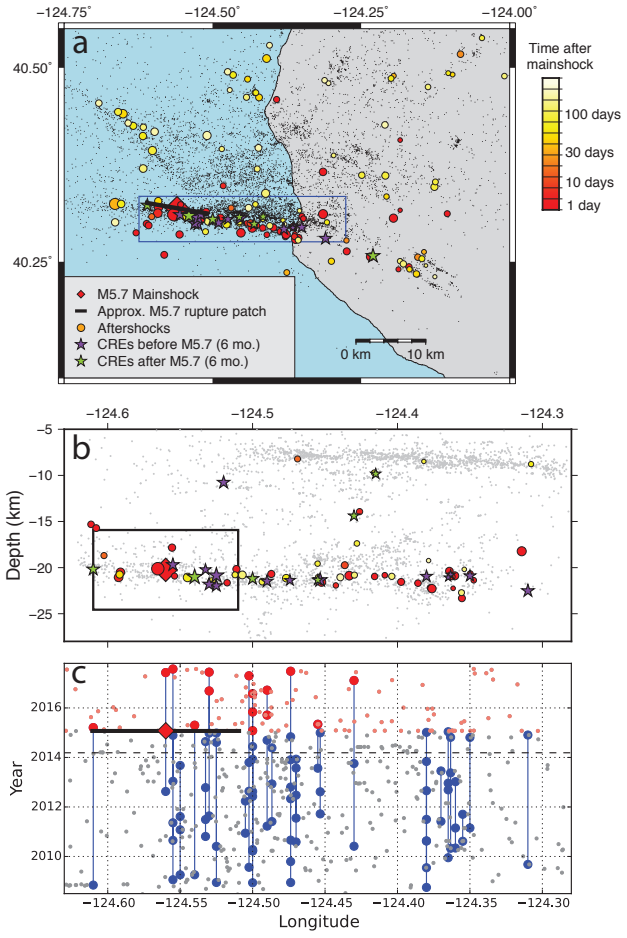

Figure 3.8: Evolution of the 2015 M5.7 earthquake sequence (double-differenced hypocenter marked by red diamond). The first-order rupture patch dimensions based on Wells and Coppersmith (1994) are shown in black. a) Map view of the earthquake sequence. Double-differenced background seismicity (1984-2017) is shown in black dots. Aftershocks of the 2015 event are shown as filled circles color-coded by time, ranging from the day of the mainshock (red) to up to six months later (yellow). Purple and green stars show the locations of CRE activity in the six months before and after the earthquake respectively. b) Cross-sectional view of the blue box in (a). c) Time-space plot of the CRE sequences in the blue box in (a) at 18-35 km depth; this depth range corresponds to the lower cluster in Figure 3.5. Sequences of CREs are shown as large dots connected by vertical lines, while background seismicity is marked by small dots. The red-blue color change indicates when the 2015 M5.7 earthquake occurred. The horizontal dashed line indicates the time of a M6.8 earthquake located 85 km to the northwest (Figure 3.5).

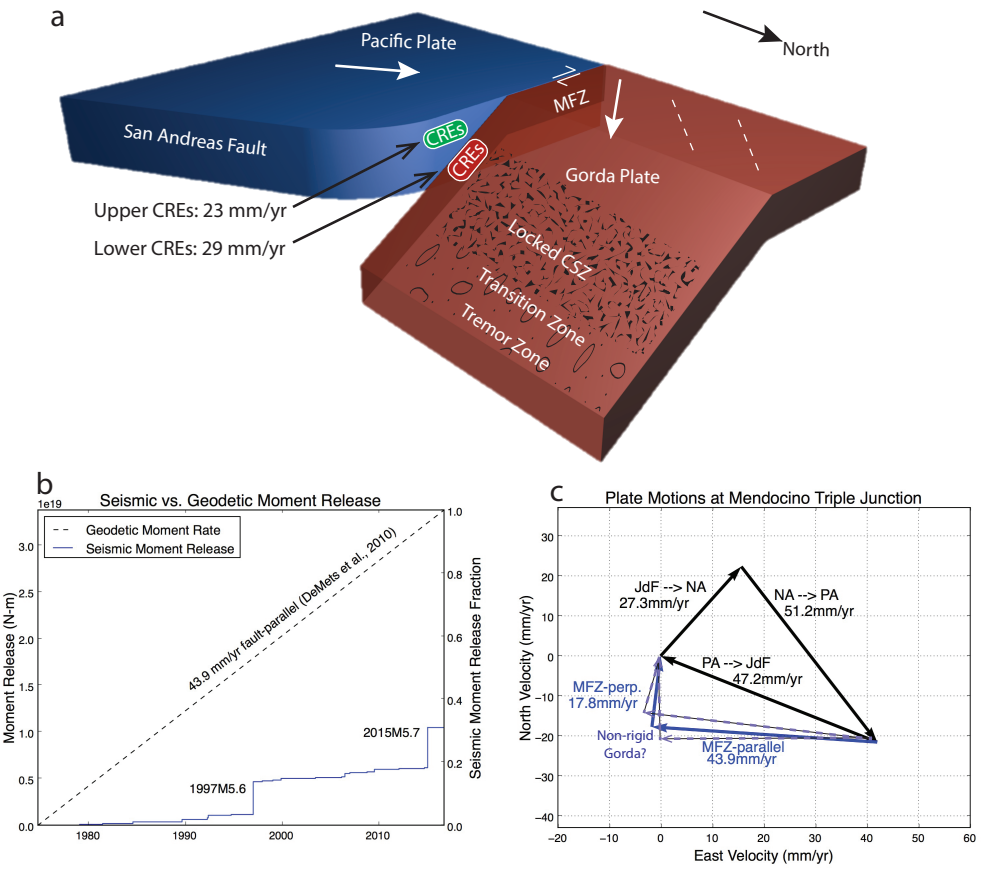

Figure 3.9: a) Schematic interpretation of the CRE sequences in the MTJ. This view is from the northeast with the North American plate removed. The red region of CRE activity shows the fastest creep rates (lower cluster in Figure 3.5d; about 29 mm/yr), while the green region shows creep rates of about 23 mm/yr. b) Long-term moment accumulation vs. seismic moment release on the MFZ (lower cluster in Figure 3.5d), showing that approximately 30% of the moment budget in the last 40 years has been released seismically in M>3.0 earthquakes from the NCSN catalog. c) Relative motion vectors around the MTJ from the MORVEL 2010 model assuming a rigid Juan de Fuca plate. The blue arrows denote the components of the Pacific/Juan de Fuca relative motion that are parallel and perpendicular to the MFZ, contributing to the dextral slip and shortening across the fault respectively. When adjusted for internal deformation within the Gorda sub-plate, relative motion vectors are lower than the MORVEL model in the western segment of the MFZ and higher in the eastern segment.

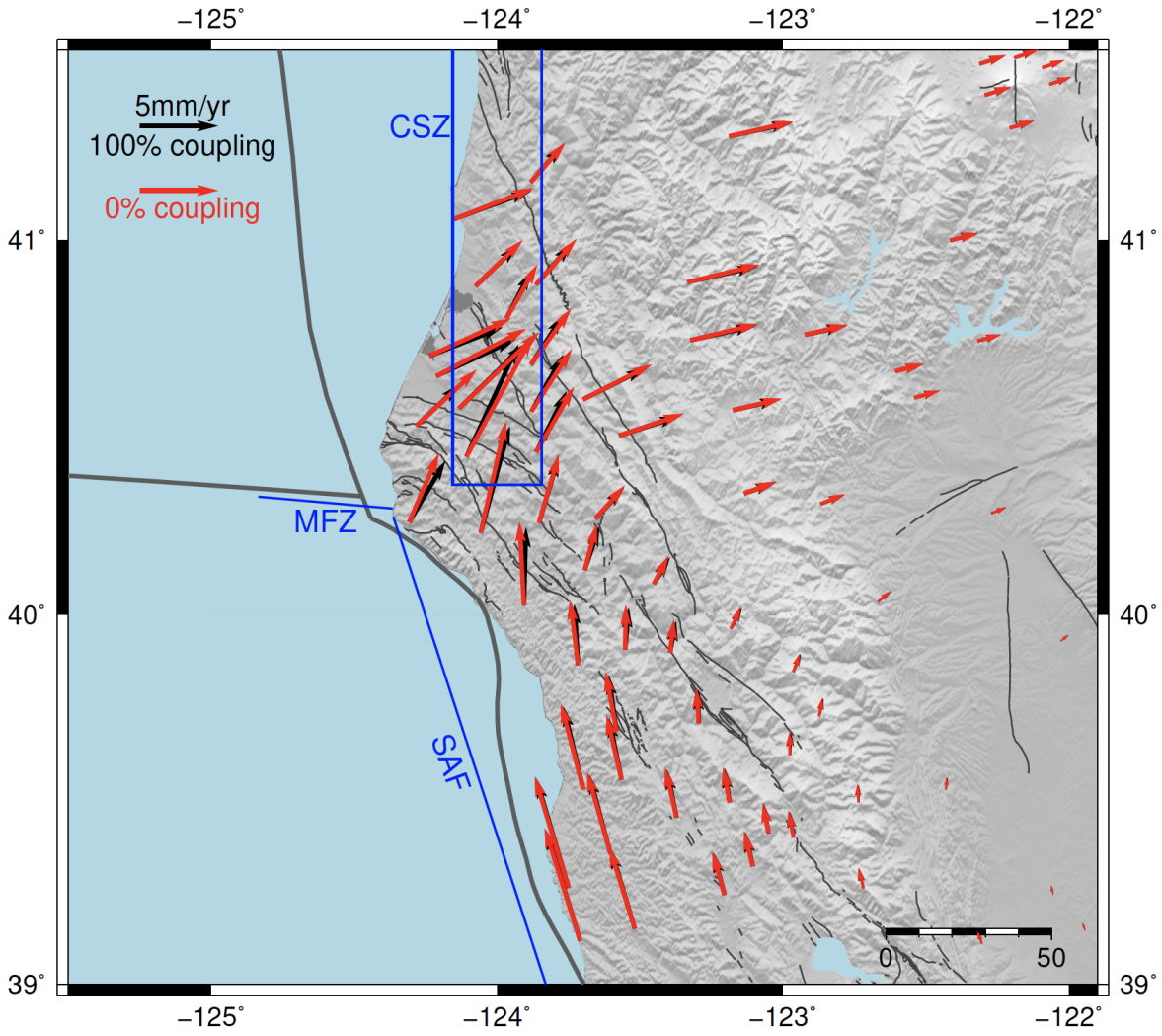

Figure 3.10: Interseismic velocities computed from a back-slip model containing the San Andreas Fault (SAF), the Cascadia Subduction Zone (CSZ) and the Mendocino Fracture Zone (MFZ). Blue regions show the source faults for backslip models. The red and black arrows show the model results when the applied backslip rates on the MFZ are 0 mm/yr (fully slipping; 0% coupling) and 48.7 mm/yr (fully locked; 100% coupling).

Chapter 4

The 2017 Mw 6.4 Moijabana, Botswana earthquake, a rare lower-crustal event within an ancient zone of weakness

Published as: Materna, K., S. Wei, X. Wang, L. Heng, T. Wang, W. Chen, R. Salman, and R. Bürgmann (2019), Source characteristics of the 2017 Mw 6.4 Moijabana, Botswana earthquake, a rare lower-crustal event within an ancient zone of weakness, Earth and Planetary Science Letters, 506, p. 348-359, doi:10.1016/j.epsl/2018.11.007.

4.1 Abstract

The 2017 Moijabana earthquake in central Botswana (Mw 6.4) was a large and deep event for a continental interior and occurred in a region with little historical seismicity. Based on InSAR measurements of surface deformation spanning the event and teleseismic observations, we determine the ruptured fault plane and finite rupture model of the earthquake. Although this oblique normal-faulting earthquake is too deep to uniquely determine the rupture plane geometry from InSAR alone, the best-fitting fault plane constrained by the joint inversion of teleseismic waveforms and InSAR data has a southwest dip and a strike of 126°, roughly consistent with the geologically mapped strike of the Kaapvaal craton's northern edge. Our results indicate that the earthquake had a total duration of ∼10s, characterized by two major asperities. The first asperity nucleated in the lower crust and then the rupture propagated up-dip. The lower crustal asperity shows a much shorter rise time compared with the shallower asperity, indicating that contrasts in stress or material properties may have played an important role in the rupture process. The earthquake appears to have occurred in the Limpopo belt, a Proterozoic orogenic belt that represents an ancient zone of weakness between the Archean Zimbabwe and Kaapvaal cratons. In the present day,

this zone of weakness may be responding to the stress field imposed by the East African Rift System.

4.2 Introduction

The vast majority of global seismicity is associated with active faults along plate boundaries. However, the occurrence of intraplate earthquakes demonstrates that continental interiors are not entirely stable and are associated with seismic hazard (England and Jackson, 2011). Large intraplate earthquakes, although rare, show that continental lithosphere can build up significant tectonic or non-tectonic stresses. The causes of these earthquakes have long been debated in the literature (Liu and Zoback, 1997; Pollitz, Kellogg, et al., 2001; Calais, Camelbeeck, et al., 2016).

A large intraplate earthquake occurred in a remote area of central Botswana on April 3, 2017. The Moijabana earthquake had an oblique normal faulting mechanism (Figure 4.1), nucleated at a depth of 29 km, and had a W-phase moment magnitude of Mw 6.5 (ANSS ComCat). It was widely felt in Botswana, Zimbabwe, and South Africa. Some buildings in nearby villages sustained structural damage, but there were no reported casualties (Government of Botswana). The event produced 11 Mb 4-5 aftershocks recorded in the USGS catalog, with the most recent so far occurring in November 2017.

The earthquake occurred in an area with no historic record of seismicity (from the ISC-GEM catalog, dating back to 1920), very little topographic relief, and no known active faults. Before this earthquake occurred, most seismic activity in Botswana was in the Okavango Delta, several hundred kilometers to the north (Reeves, 1972; Gumbricht et al., 2001). In this study, we jointly analyze Interferometric Synthetic Aperture Radar (InSAR) measurements of deformation from the earthquake and teleseismic waveform observations to constrain the source parameters and kinematic rupture of the event. We also consider geologic and geophysical information on the epicentral area to better understand the event's tectonic framework.

4.3 Tectonic Setting

The large-scale active tectonic regime of southern Africa (Figure 4.1) is the East African Rift System (EARS). The rift system is accommodating extension between the African plate (Nubia) and the Somalia plate (DeMets et al., 2010). Extension is faster (4-6 mm/yr) in the north and slower (1-2 mm/yr) in the south, where the rift also splits into eastern and western branches (Kinabo, Atekwana, et al., 2007; Stamps, Calais, et al., 2008). In Botswana, the southwestern EARS produces slow extension in the northwest of the country, but is not known to extend to the area of the earthquake.

Southern Africa includes a broad region known as the Kalahari craton (Hanson et al., 2004; Priestley et al., 2006), which contains most of Botswana and the epicenter of the

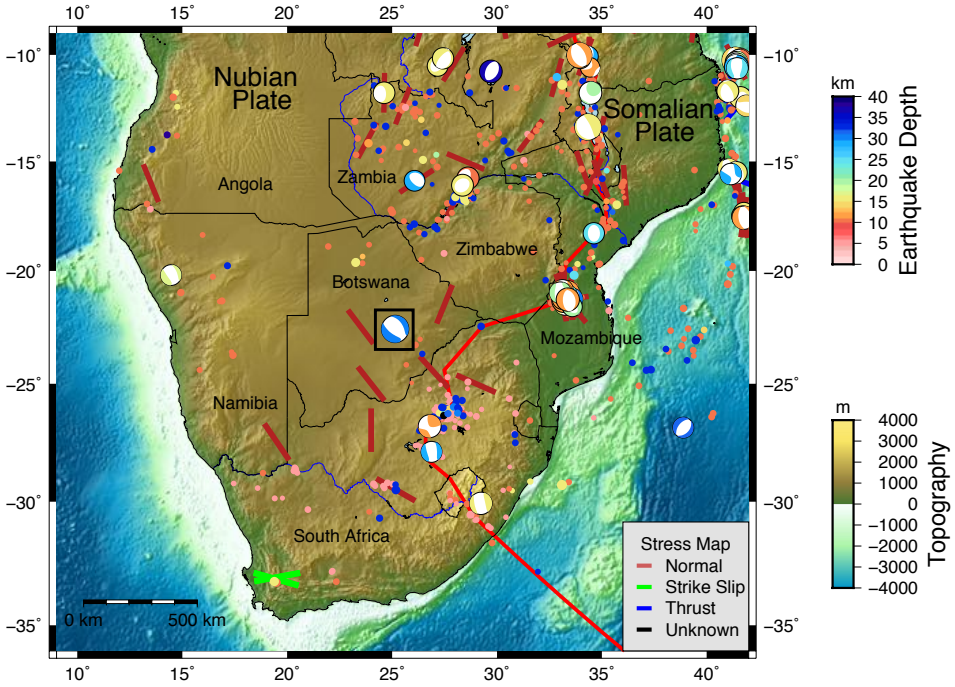

Figure 4.1: Tectonic setting of southern Africa. The colored dots represent historical earthquakes in the USGS COMCAT catalog (1910-2017). Moment tensors are shown where available in the Global Centroid Moment Tensor (GCMT) catalog from 1976-2017 (Ekström et al., 2012). Event colors represent hypocentral depth from the USGS. The simplified EARS plate boundary from Bird (2003) is shown in red. The 2017 Moijabana earthquake is outlined by a black box. Orientations of SHmax from the World Stress Map 2008 (Heidbach et al., 2010) are drawn as solid bars, colored according to their faulting environment.

Moijabana earthquake. This craton is generally Archean in age and participated in the formation of multiple supercontinents through geologic time (Groenewald et al., 1995). The Kalahari craton has remained stable over the last 2.3 Ga, although there is evidence for intrusions and orogenesis within the craton at various times (Priestley et al., 2006). At a smaller scale in Botswana, the Kalahari craton is made of a number of constituent geologic terranes (Figure 4.2a). Prominently, the Kaapvaal craton and Zimbabwe craton are two major blocks of Archean age that have been deformed little since their formation, and the rocks within these cratons display only low-grade metamorphism (Begg et al., 2009; Wit et al., 1992).

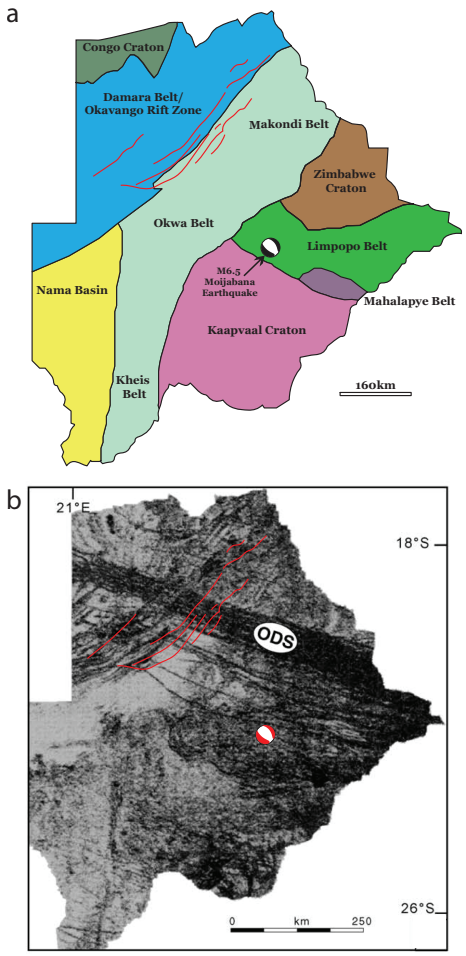

Figure 4.2: a) Schematic geologic map of Archean terranes in Botswana based on a compilation of maps and information in Key and Ayres (2000), Schluter (2006), Mapeo et al. (2001), and Millonig et al. (2010). b) Aeromagnetic data over Botswana showing the placement of Karoo dykes. Figure is adapted from Le Gall et al. (2005). ODS represents the Okavango Dyke Swarm, a member of the Karoo dykes. Fault traces of the ORZ, shown as red overlays, are from Kinabo, Atekwana, et al. (2007).

In contrast, a series of highly deformed Archean and Proterozoic orogenic belts surround these cratonic blocks (Figure 4.2). The Limpopo belt is Archean age continental material (Wit et al., 1992) that was subjected to multiple episodes of intense deformation and high-grade metamorphism throughout the Proterozoic (Mapeo et al., 2001). The southern edge of the Limpopo belt is the Mahalapye belt, a mix of heavily deformed migmatite, gneiss, granodiorite, and quartz-monzonite that is intruded by granitic plutons (Millonig et al., 2010;

Ranganai et al., 2002). North and west of the Kaapvaal craton, the Makondi, Okwa, and Kheis belts together comprise a NE-SW trending structure known as the Kalahari Suture Zone (Key and Ayres, 2000). This former thrust zone contains granulite facies metamorphic rocks such as garnet-bearing gneiss (Mapeo et al., 2001), but in many places today is overlain with thick Phanerozoic sediments from the Kalahari desert (Schluter, 2006). The age range for most deformation in the orogenic belts around the two cratons is 1.96-2.06 Ga (Key and Ayres, 2000; Mapeo et al., 2001).

The most recent major deformation event throughout Botswana was the emplacement of the Karoo igneous dykes related to the Mesozoic breakup of Gondwana (Le Gall et al., 2005). A survey of almost 400 Karoo dykes found that they consist of mainly basalt, dolerite, and gabbro, and that 87% of them were emplaced 178-179 Ma (Le Gall et al., 2005). Some of the dykes trend NE while others trend WNW through the Limpopo belt. An aeromagnetic dataset clearly showing the Karoo dyke intrusions is shown in Figure 4.2b.

Further north in Botswana, the Damara Belt and Okavango Rift Zone (ORZ) form an ancient collisional zone that now accommodates geologically recent rifting (Kinabo, Atekwana, et al., 2007; Modisi et al., 2000). The ORZ, consisting of multiple northeast striking half-grabens, is often considered a type example of an incipient rift, as rift initiation is inferred to be as young as 40 Ka (Bufford et al., 2012; Kinabo, Hogan, et al., 2008). The ORZ is part of the southwest branch of the EARS, but there are no mapped faults or evidence of young tectonism south of ∼21°S (Bufford et al., 2012).

Historical seismicity in southern Africa is primarily related to EARS features, such as the ORZ and rifting in Zimbabwe/Zambia, or related to mining activity in central South Africa (Figure 4.1). Two large rifting earthquakes have taken place in recent years: a Mw 6.2 event in Malawi in 1989, and a Mw 7.0 event in Mozambique (Copley et al., 2012). Most present-day seismicity in Botswana, including a sequence of two M5.8-M5.9 earthquakes in 1952, is associated with the ORZ (Reeves, 1972).

Previous work on the Moijabana earthquake has focused on the geologic and aeromagnetic features at the edge of the Kaapvaal craton, the surface deformation patterns, and the potential association of the event with anthropogenic activity (Albano et al., 2017; Kolawole et al., 2017). In this work, we combine the InSAR-measured surface deformation of the event with teleseismic waveform modeling to better understand the earthquake's source parameters and tectonic setting.

4.4 InSAR data and modeling

We use synthetic aperture radar (SAR) acquisitions from the European Space Agency's Sentinel-1B satellite to quantify the deformation field of the Moijabana earthquake. Twenty-one scenes from December 24, 2016 to September 2, 2017 obtained along the ascending orbit were processed to form interferograms. No descending-orbit data have been collected over this area.

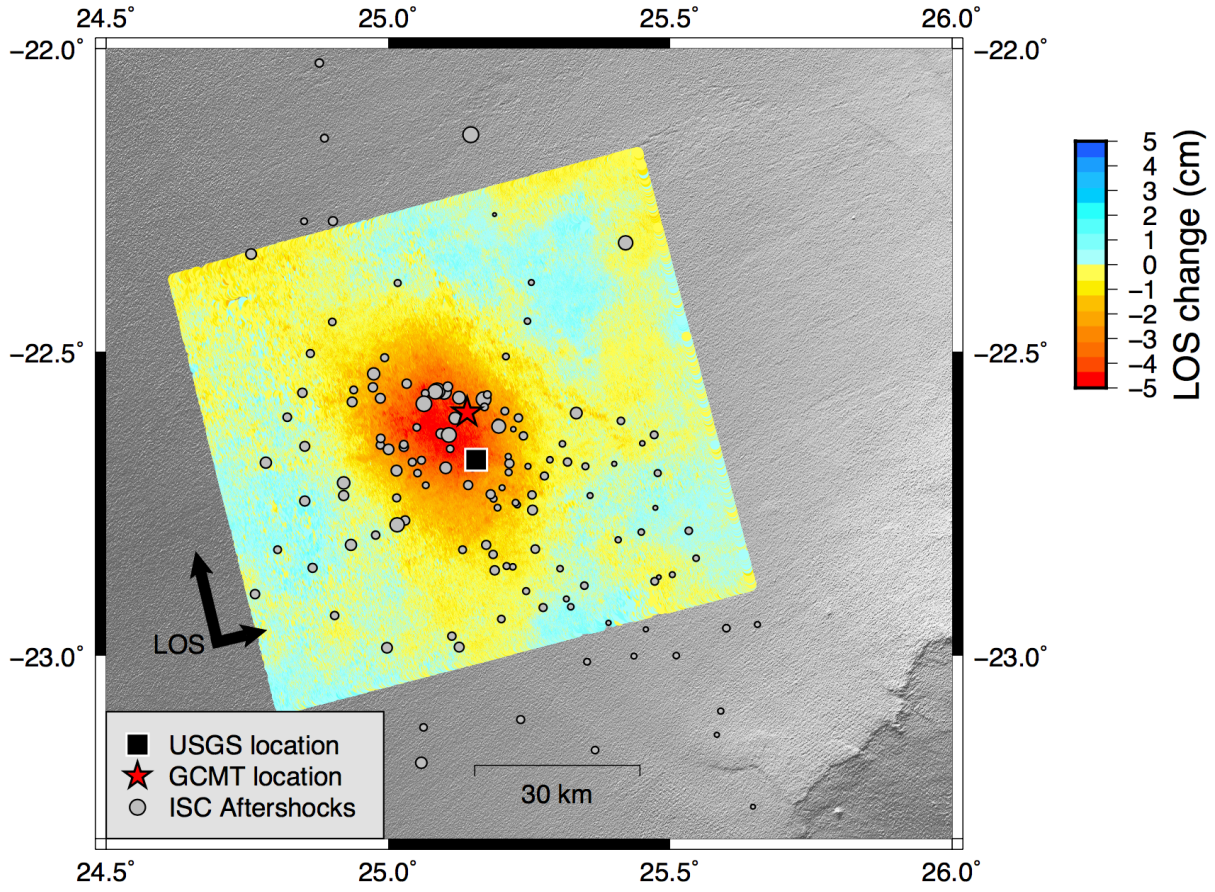

Figure 4.3: Unwrapped Sentinel-1B stack of interferograms for the Moijabana earthquake. Negative line-of-sight (LOS) displacement means that the ground moves away from the satellite, representing either subsidence or east-northeast movement. Aftershocks are from the ISC catalog (http://www.isc.ac.uk/iscbulletin/search/catalogue/).

We selected the first image acquired before the earthquake as master and co-registered all the other images with it, forming 20 interferograms with the same master image. We used a digital elevation model from the Shuttle Radar Topography Mission (SRTM-1) to correct for the contribution of topographic phase. Phase unwrapping was performed using the statistical-cost network-flow algorithm for phase unwrapping (SNAPHU)(Chen and Zebker, 2000). After unwrapping these interferograms, a linear ramp was estimated from data points far away from the deformed area and was removed from each interferogram in order to account for possible long-wavelength orbit errors and atmospheric noise. We discarded 6 interferograms with visible complex atmospheric turbulence that is difficult to estimate. In order to suppress temporally uncorrelated noise, we then averaged the two sets of remaining

unwrapped interferograms: one containing interferograms formed between the master and the images acquired before the earthquake, and the other formed between the master and images acquired after the earthquake. We subtracted the averaged unwrapped phase measurements from these two sets of interferograms to obtain a cleaner coseismic deformation measurement. Finally, we used the quadtree downsampling method (Jonsson et al., 2002) to reduce the number of InSAR data to 438 points, making the inversion computations more feasible.

The observations show that the earthquake locations in the USGS COMCAT catalog, the GCMT catalog, and the InSAR data are quite close (within 10 km; Figure 4.3), suggesting that location biases from errors in the seismic velocity model are small compared to some other areas (Weston et al., 2011). The USGS hypocentral (29 km) and moment tensor (23 km) depth estimates place the event in the lower crust. Surface displacement patterns for deep faulting events generally have the same nodal-plane ambiguities as seismic moment tensor solutions, and the ambiguity increases with source depth. Our goal in modeling the deformation was to find best-fitting solutions based on both nodal planes and compare their misfit values, in hopes of identifying a preferred fault plane and kinematic slip model from the surface deformation.

With the unwrapped InSAR observations, we performed a nonlinear inversion for fault location, geometry and uniform slip amplitude and direction on the fault. We used the Markov Chain Monte Carlo (MCMC) slice-sampling technique from Neal (2003) to draw random samples from the posterior probability density function for each parameter in the model. Initially we prescribed the source to be a rectangular uniform-slip patch with length 23.4 km, width 13.6 km, and slip of 0.66 m. These describe the dimensions for a typical Mw 6.5 normal-faulting rupture (Wells and Coppersmith, 1994). We then used rectangular dislocation elements in an elastic half-space (Okada, 1985) with Poisson's ratio of 0.25 to form Green's functions for line-of-sight (LOS) displacements. We computed the modeled LOS displacements at 438 locations of the down-sampled InSAR observations (Figure 4.4).

As this is a blind rupture and we do not have knowledge of fault structures at depth from past seismicity, we allowed for 7 free parameters in the inversion. The parameters of the inversion are strike, dip, rake, the x and y coordinates of the upper left corner of the fault plane, fault depth z, and event moment magnitude (corresponding to a uniform slip value on the prescribed dislocation plane). We began with initial models drawn from the two focal planes in the GCMT moment tensor solution, and placed the top of the fault plane at 23 km depth (strike, dip, rake = 126°, 51°, -107° and strike, dip, rake = 332°, 41°, -70°). We instituted wide-ranging uniform priors on most parameters. For instance, the range of possible strike values was 90° (i.e., the uniform prior spanned 90°-180° for inversions using the southwest-dipping plane, and 270°-360° for inversions using the northeast-dipping plane). The uniform priors on dip and rake also spanned 90°. The prior distribution on moment magnitude ranged from 6.3 to 6.7. We then initialized models from the two possible nodal planes of the moment tensor, generated 20,000 samples for each model, and analyzed the posterior probability density functions (PDFs).

The nonlinear inversion results show that we are able to fit the downsampled data very

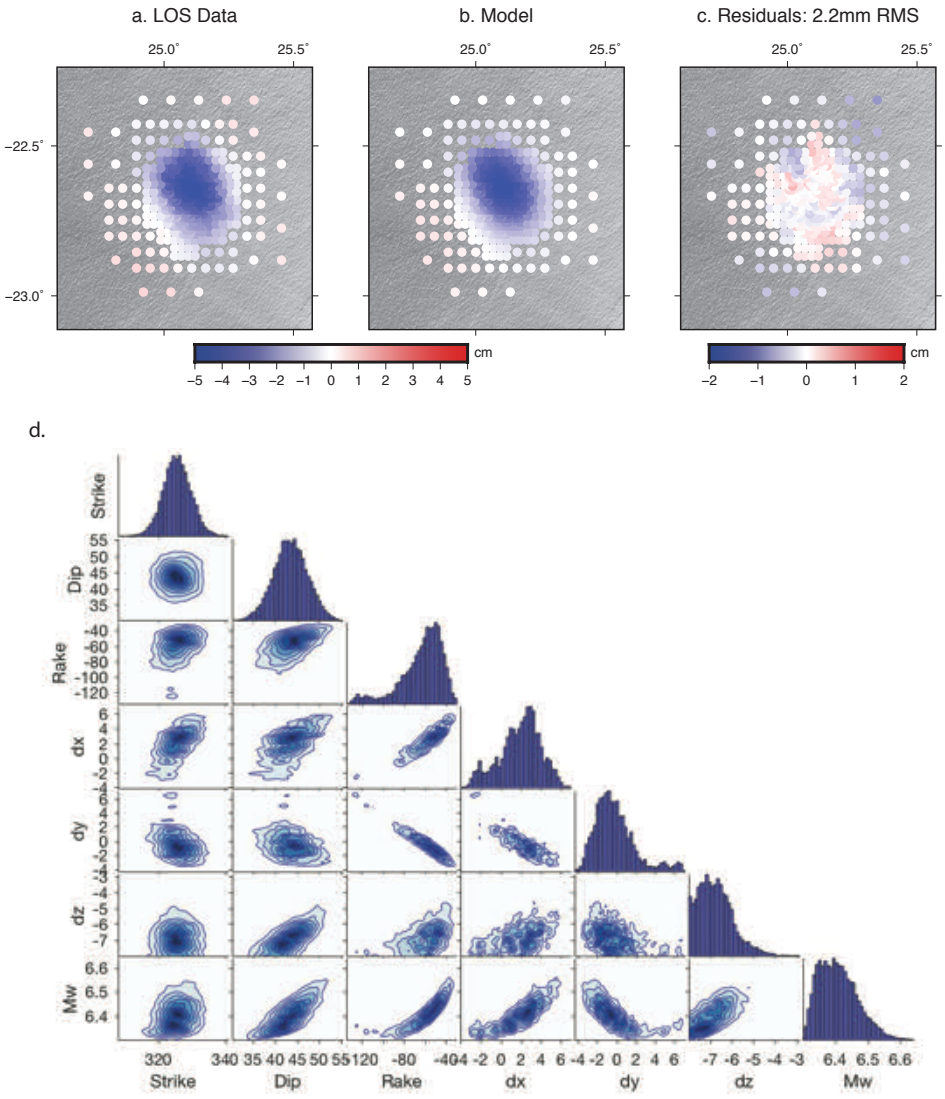

Figure 4.4: a) Unwrapped and sub-sampled line-of-sight displacement data for the Moijabana earthquake. b) Preferred model based on best-fitting posterior parameter values with a NE-dipping plane (strike = 326°). c) Residuals to the best-fitting model. d) Histograms and tradeoff diagrams showing model parameter distributions from the MCMC sampling algorithm. Positive z is deeper; negative z is shallower.

well using fault planes in both NE-dipping and SW-dipping orientations. The overall best-fitting model is a NE-dipping plane (Figure 4.4) with a strike of 326° and an RMS misfit of 2.2 mm. When we use a SW-dipping plane, our best-fitting model has a strike of 131° and

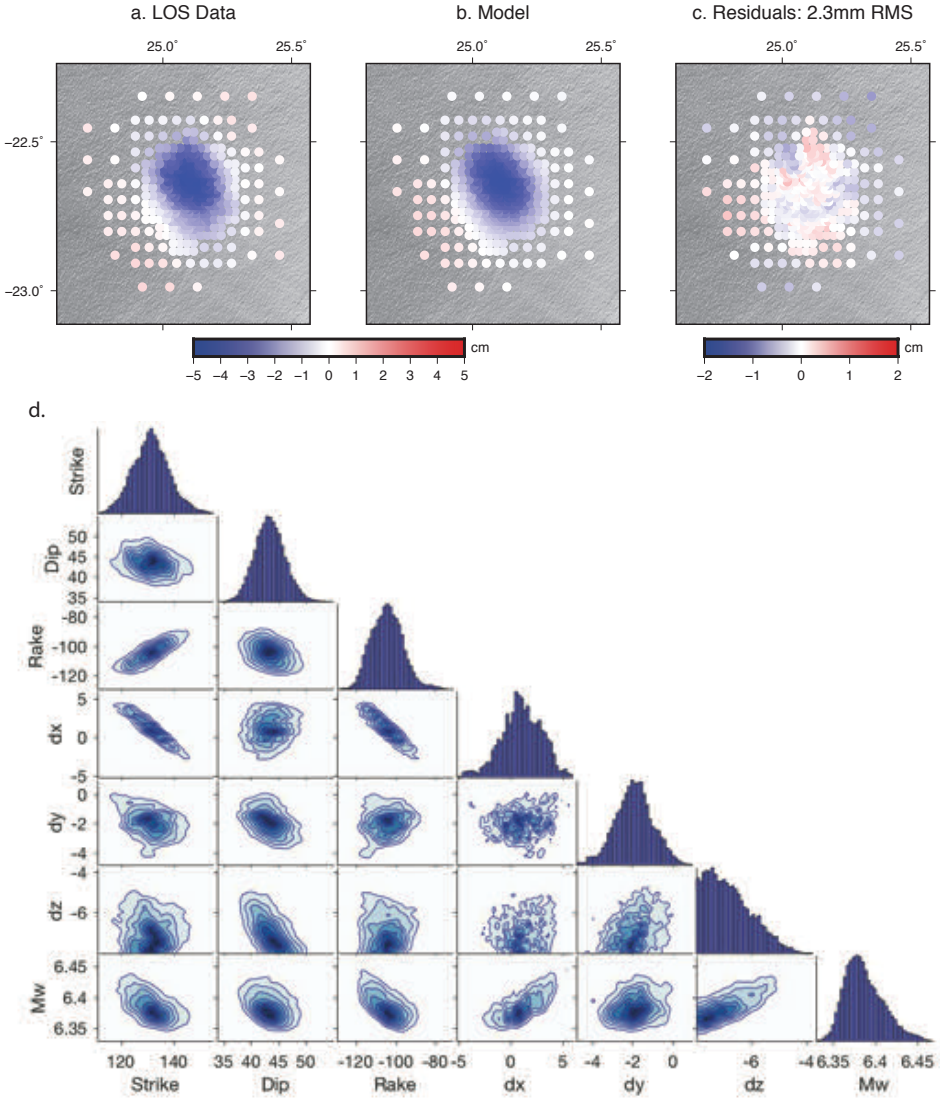

Figure 4.5: Same as Figure 4.4 for the southwest dipping plane (strike = 126°).

fits the data with a 2.3 mm RMS value (Figure 4.5). The PDFs for strike, rake, dip, and position are well constrained in both cases. The best-fitting inversion results for both focal planes slightly reduce the magnitude of the earthquake, preferring values of approximately Mw 6.4 instead of Mw 6.5 (corresponding to a 27% reduction of moment from the USGS W-phase moment tensor estimate of 6.188e+18 N-m). The results are similar if we constrain the magnitude to Mw 6.5, but the RMS misfit is slightly higher (2.9 mm) for the southwest-dipping plane under that constraint.

Input Source (strike/dip/rake)	Input Depth (km)	Applied Noise (mm)	Inverted Source (strike/dip/rake)	RMS Misfit (mm)
A. 126, 51, -107	23	3	129, 50, -105	3.0
A. 126, 51, -107	23	3	325, 38, -64	3.0
A. 332, 41, -70	23	3	129, 50, -105	2.9
A. 332, 41, -70	23	3	326, 42, -88	3.0
B. 126, 51, -107	23	0	130, 52, -105	0.7
B. 126, 51, -107	23	0	330, 36, -59	0.5
B. 332, 41, -70	23	0	139, 47, -100	0.6
B. 332, 41, -70	23	0	332, 42, -74	0.5
C. 126, 51, -107	15	0	127, 51, 107	0.4
C. 126, 51, -107	15	0	321, 37, -65	1.3
C. 332, 41, -70	15	0	146, 45, -94	1.3
C. 332, 41, -70	15	0	331, 42, -76	0.6

Table 4.1: Synthetic tests for resolving the geometry of a known source through the nonlinear inversion technique. The two inversion results for each input source correspond to starting models of either nodal plane geometry.

We performed synthetic tests in order to determine the sensitivity of the InSAR data to the fault plane in question, as both conjugate fault planes seemed to model the data extremely well. As a test, we produced several forward-modeled displacement fields from rectangular sources of known source parameters, added a small amount of Gaussian random noise, and attempted to recover the input sources through our inversion procedure (Table 4.4). In the first case, we forward modeled a rectangular fault source defined in the "Input Source" column and added Gaussian random noise with an amplitude of 3.0 mm to simulate the typical misfit of our inversions in Figures 4.4 and 4.5. We found that we can reproduce the synthetic displacement field equally well with solutions near both nodal planes ("Inverted Source" column in Table 4.4A). The RMS misfit values for inverted solutions based on the two fault planes were identical.

In the case of inverting the forward-modeled displacement field with no additional noise, we still found that we were unable to distinguish the fault plane with the data (Table 4.4B) because the RMS misfits for the two possible fault planes were very similar. However, repeating the synthetic test with a source at 15 km depth rather than 23 km, we found that the inversion begins to distinguish between the input fault geometry and the conjugate fault geometry (Table 4.4C) through producing lower misfits for the plane matching the input geometry.

In light of our inversion results and synthetic tests, we suggest that two sets of strike, dip, and rake values satisfy the observed InSAR data within the level of the noise. For an earthquake of this magnitude and depth, InSAR measurements alone may be unable to

determine which of the two fault planes ruptured. Additional constraints beyond the InSAR are required to unambiguously resolve the fault plane for an earthquake of this magnitude and depth.

4.5 Teleseismic data and modeling

In order to provide additional constraints on this earthquake, we performed joint teleseismic-InSAR inversions for the finite fault model of the earthquake. We discretize the planar fault into smaller subfaults, and invert for the slip, rake, rise time, and averaged rupture velocity on each subfault. The seismic data are more sensitive to the time evolution of the rupture, while the geodetic data are more sensitive to the static fault displacements; therefore, the combination of the two datasets may provide stronger constraints on the source parameters.

We downloaded the teleseismic broadband waveform data from an angular distance range of 30°-90° from the IRIS II and IU networks. We selected stations to sample the focal sphere as uniformly as possible. Although there are many high quality stations available, we did not use all of them because nearby stations have very similar P and SH waveforms. Based on these criteria, we selected 39 P-waves and 36 SH-waves to provide good coverage in azimuth and distance. The instrument response was removed and the displacement waveforms were low-pass filtered below 1 Hz. Synthetic waveforms were produced using a 1-D layered earth model with Moho depth constrained from a receiver function study (Nguuri et al., 2001). The same velocity model is used to calculate the static Green's functions with a method proposed by Xie and Yao (1989). We weighted the teleseismic and InSAR datasets equally and imposed a smoothing constraint on the slip distribution in the inversion. The non-linear inversion was solved with a simulated annealing algorithm to quickly converge on global minima (Ji et al., 2002). Finally, we tried inversions on the candidate nodal fault planes in the GCMT solution at a range of hypocentral depths. We found that a hypocenter of 29 km provides the best fit for both fault planes. We also found that the GCMT solution is similar to the solution when we inverted the P and SH waveforms for a focal mechanism.

The best-fitting joint inversion result was found using a SW-dipping fault plane (strike = 126°; Figure 4.6). Both the modeled teleseismic waveforms and InSAR results fit the data well (Figure 4.6 and Figure 4.7). The displacement P-waves and the depth phases (pP and sP) show clear multiple asperities, indicating a complex rupture process of the earthquake. The best-fitting model shows a rupture that initiated at ∼30 km depth in the lower crust and propagated updip to ∼20 km depth, where it resulted in about 80 cm of slip at the peak of the slip distribution (Figure 4.6). The modeled moment magnitude reflects a Mw 6.4 event, slightly smaller than the Mw 6.5 reported in the W-phase moment tensor. The depth distribution is consistent with the reported hypocenter of 29 km and centroid depth of 23 km. The deep asperity shows a shorter rise time (∼1 s) compared with the shallower rupture (>2 s), corresponding to two peaks in the moment rate function (Figure 4.6c). However, we note that the constraint on the risetime from teleseismic waveform data is relatively weak, and that additional nearfield strong motion data, if there is any, is needed to better resolve

the risetime.

The inversion results on northeast-striking planes produced clearly worse fits to the teleseismic data than the results using southwest-striking planes (average waveform cross-correlation coefficients of 84.8% vs. 81.1%), especially for the depth phases (Figures 4.8-4.9).

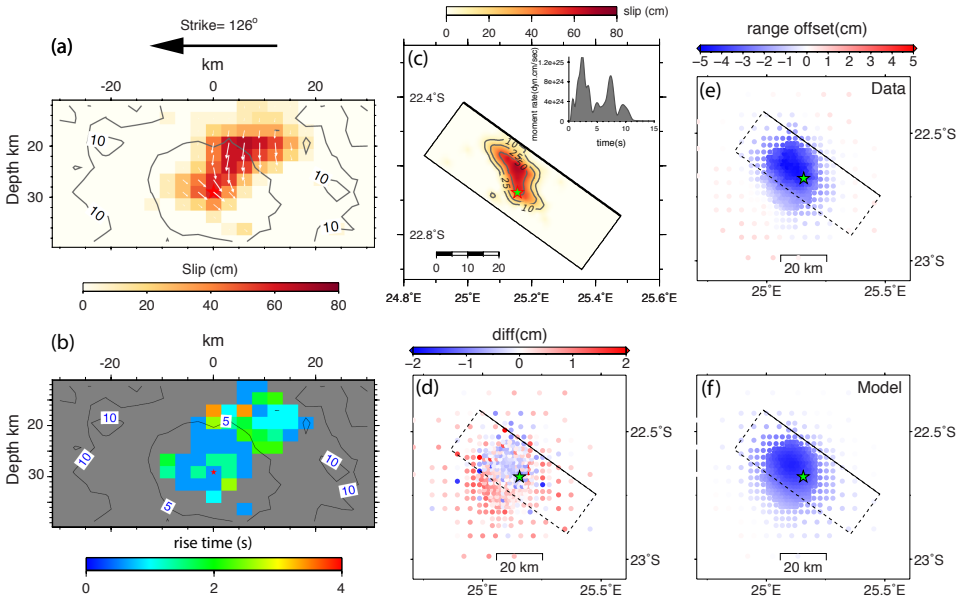

Figure 4.6: Joint teleseismic-InSAR inversion results for a plane with 126° strike. a) Solution for distributed slip on the fault interface. b) Distribution of rise time on the interface. c) Map view of slip distribution, and moment rate function produced by the inversion. d) Residuals between InSAR LOS data and model. e) InSAR LOS data. f) Model fit to the InSAR LOS data (RMS misfit = 6.3 mm).

Compared to the joint inversions, teleseismic-only inversions show similar first-order slip dimensions and peak slip. However, the inversions differ in the relative strength of the two asperities in Figure 4.6. The teleseismic-only inversion has a stronger asperity on the deeper part of the fault plane and a weaker asperity on the shallow part. This discrepancy makes sense given that the deeper asperity also has a shorter rise time in the joint inversion, thus contributing more to the seismic signal.

To verify the ruptured fault plane (southwest dipping) as revealed by the joint inversion of teleseismic and InSAR data, we further refined the location and focal mechanisms of three aftershocks, aiming at delineating the fault geometry. The procedure uses regional broadband waveforms to determine the aftershock focal mechanisms, and then refines their horizontal locations relative to the mainshock by surface wave cross-correlation. Finally, the depths of the aftershocks were constrained by modeling of teleseismic depth phases. The

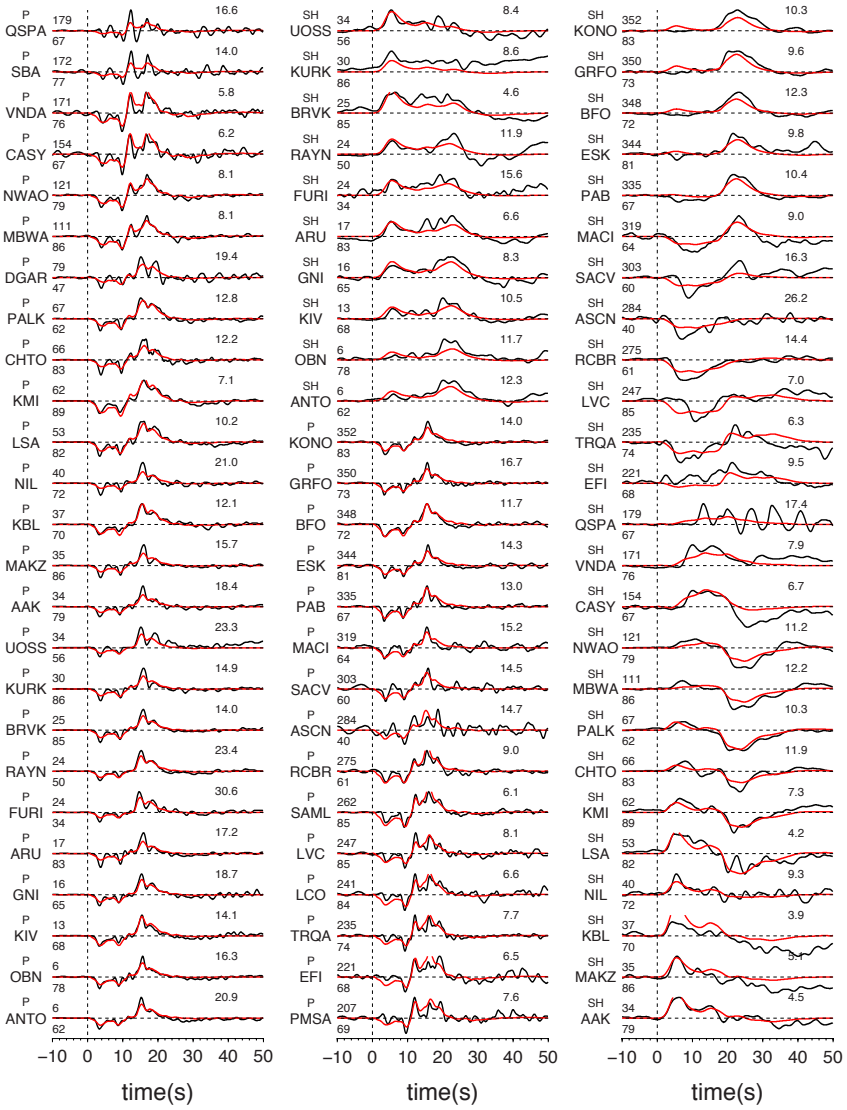

Figure 4.7: Teleseismic waveform fits for P and SH phases from the joint teleseismic-InSAR inversion of the Moijabana earthquake. The numbers above and below the start of each trace represent the azimuth to the station and the station angular distance in degrees, respectively. The numbers on the top right of each trace are the peak amplitudes of the data in micrometers. The average waveform cross-correlation coefficient between data and synthetics is 84.8%.

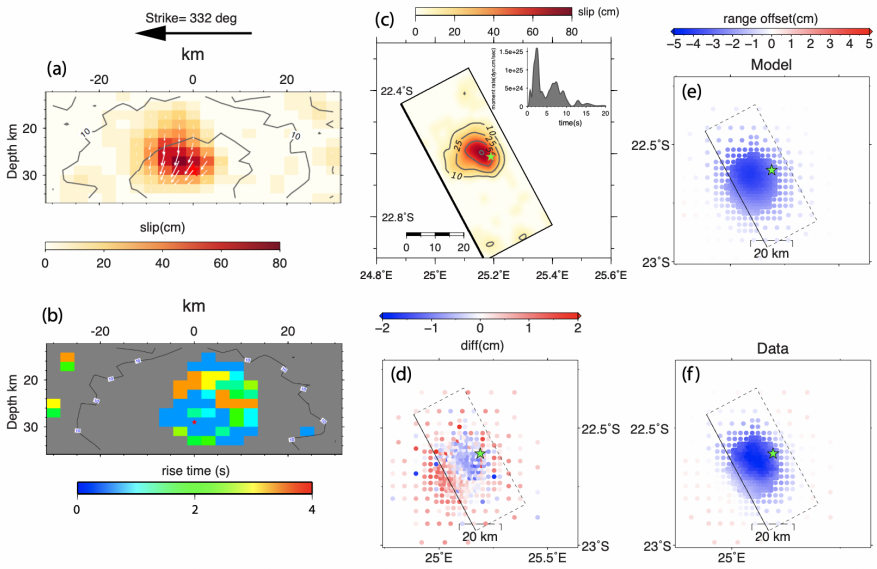

Figure 4.8: Model results for the best-fitting inversion on the 332° striking fault plane; see Figure 4.6 for description of individual panels. The RMS misfit of the InSAR LOS data is 6.2 mm.

methods we employed are similar to those described in Wang, Bradley, et al. (2018), Wang, Wei, et al. (2017), and Zhu and Helmberger (1996). Our refined aftershock distribution (Figure 4.10), although it only includes three aftershocks, delineates a fault plane that is dipping to the southwest, consistent with our joint inversion results.

4.6 Discussion

The Mw 6.4 Moijabana earthquake in central Botswana was a large earthquake for a location far away from known plate boundaries. Stable continental regions, such as the epicentral region of this earthquake, are thought to generate only 0.3% of seismic moment release globally (Johnston, 1989). As such, it is important to understand this rare event's tectonic and geodynamic context. Here we interpret the findings of the InSAR and teleseismic modeling, and discuss the region's tectonic setting and potential stress conditions.

4.6.1 Geophysical inversion results

Our modeling of the InSAR dataset for source fault parameters reveals slightly lower RMS misfit values on planes that dip to the northeast, consistent with previous analyses of

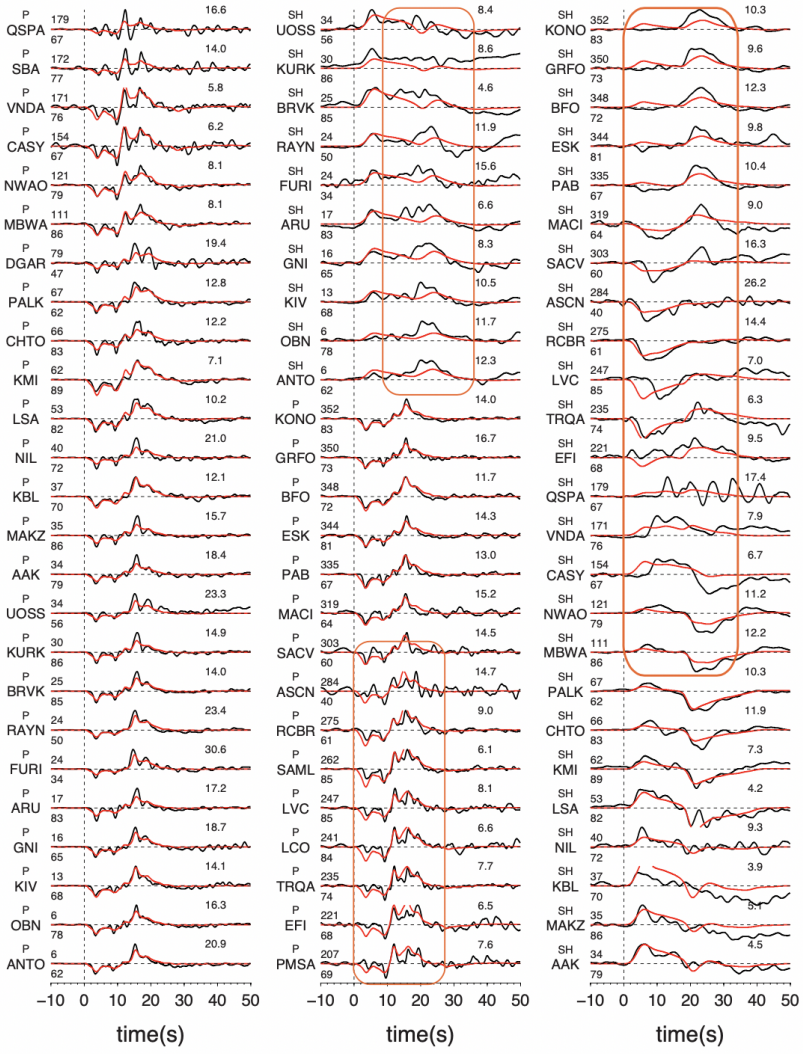

Figure 4.9: Teleseismic waveform fits for the best-fitting model with a strike of 332° (not preferred in our study). The depth phases of the P-wave arrivals and the SH waves are fit more poorly in this model compared to the model with a strike of 126° (Figure 4.7). The average waveform cross-correlation coefficient between data and synthetics is 81.1%.

this event (Albano et al., 2017; Kolawole et al., 2017). However, we find that due to the depth of the earthquake, the magnitude, and the single viewing geometry available from the Sentinel-1B satellite, we can model the LOS observations almost equally well with models from both possible fault orientations. This conclusion is similar to that of Gardonio et al. (2018), who also analyze Sentinel-1 InSAR data and obtain a similarly ambiguous result with respect to the modeled fault plane. We note that the preferred fault models of our study and Gardonio et al. (2018) differ in the details, and in particular, the fault dip differs by as

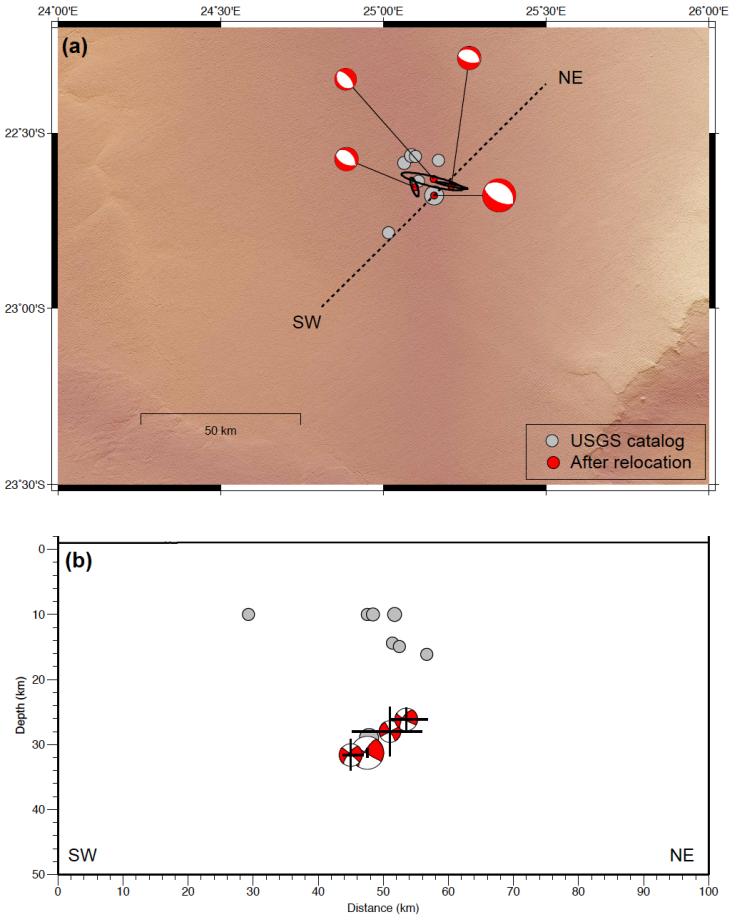

Figure 4.10: Map view and depth profile of the mainshock and three relocated aftershocks, shown as red dots in the map view and beach balls on the profile. Crosses indicate location uncertainty. For comparison, the earthquake locations from the USGS catalog are shown as gray circles.

much as 30 degrees. We suspect that differences in modeling strategies can explain these discrepancies. InSAR downsampling, atmospheric noise mitigation, inclusion of rake as a free parameter, and data covariance assumptions are all different between the two studies, and we suspect that such differences can influence the results of the inversions. Another difference could be the time span of data used. For our inversion, we use a months-long stack of InSAR images, which may include some postseismic signal. However, we do not see

evidence for resolvable postseismic deformation in interferograms from 0-5 months after the earthquake, so we think this effect is small (Figure 4.11). Instead, these differences likely highlight the inherent challenges of using geodetic-only data to resolve the precise kinematics of deep earthquakes.

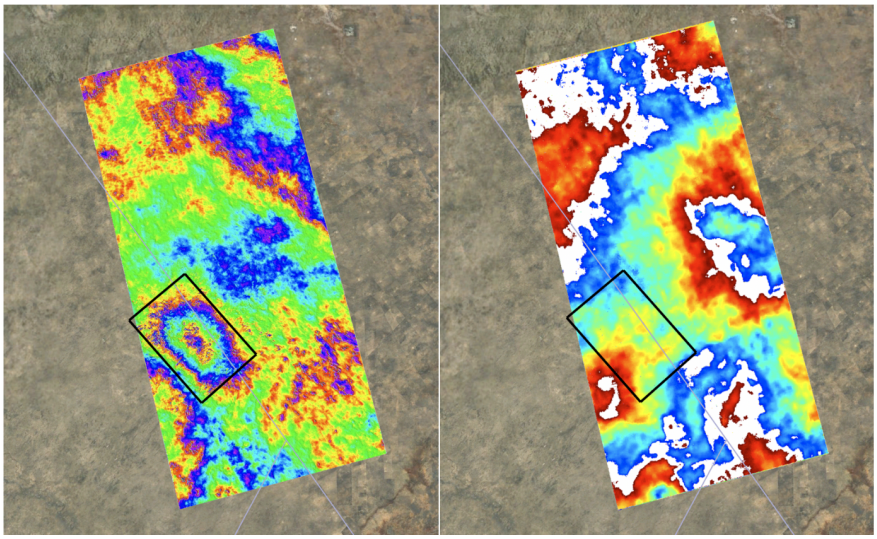

Figure 4.11: Two Sentinel-1 interferograms, one spanning the coseismic period (left) and one spanning the postseismic period from 7 days to 156 days after the earthquake (right). Each fringe represents 2.8 cm of line-of-sight displacement. For this event, postseismic displacements appear to be at or below the level of the InSAR noise in the mainshock area (black box).

We find that the joint InSAR-teleseismic dataset, on the other hand, is better able to resolve the focal plane ambiguity, as has been observed for other earthquakes around the world (Weston et al., 2014). As the two conjugate fault planes of the moment tensor solution are equivalent in the double couple point source solution, they will produce identical waveform synthetics if the source is simple enough to be approximated by a point source. The waveforms of this event, and in particular the P-waves, require a finite rupture model with multiple asperities and rupture directivity to better represent the complexity of the source. In this case, the ambiguity between the two conjugate fault planes can be resolved through the teleseismic data. Our modeling results (Figures 4.6 and 4.7) show that the fault plane with a strike of 126° can fit both direct phases and depth phases better than the fault plane with a northwesterly strike. This is also consistent with the relocated epicenters of three aftershocks (Figure 4.10).

Both our InSAR-only results and our joint inversion results suggest that the true magnitude of the event may be slightly lower than Mw 6.5. The InSAR inversions based on both conjugate fault planes find preferred moment magnitude values around 6.4. The preferred models from the joint inversions also result in an event with Mw=6.4, a moment reduction

of about 27% compared to the moment of the USGS W-phase moment tensor. Similar discrepancies in moment release have been identified in other cases around the world; a global survey found that typical variability of seismic and geodetic moment estimates is about 20%, and can be as high as 44% in some cases (Weston et al., 2011). In the case of the Moijabana earthquake, we speculate that this difference in calculated magnitude may be due to higher-than-average shear modulus at the depth of the earthquake. For the seismic dataset, the high quality of waveform fits for such a relatively small earthquake may result from the simple crustal structure and flat topography in the epicentral region.

The teleseismic dataset also contains an interesting feature with respect to the temporal evolution of this earthquake. The moment rate function shows two distinct peaks, a feature also seen in the SCARDEC solution for the event (Vallee et al., 2011). In the finite source inversion, it seems that the deeper portion of the fault, which ruptured first, had a short rise time (<1 s), in contrast with a longer rise time (>2 s) for the shallower portion of the rupture, although near-field data would be needed to fully quantify these rise times. These features of the rupture may indicate that the fault contains a heterogeneous structure of asperities with locally differing stress conditions or frictional properties. Based on our joint inversion slip model, the static stress drop of the earthquake is only around 1 MPa, which is much smaller than the stress drops of most intra-plate earthquakes (Kanamori and Anderson, 1975). Low stress drops indicate relatively modest high frequency radiation, but unfortunately, we do not have the near field strong motion data that would be needed to verify this.

4.6.2 Deep intraplate earthquakes at craton edges

The Moijabana earthquake took place within the Limpopo Belt, a Proterozoic orogenic zone that was previously reactivated during major tectonic episodes. It appears to be located near the contact between the Limpopo Belt and the Kaapvaal craton (Figure 4.2a). The Jurassic-age Karoo dyke swarm, emplaced in a nearby area during the break-up of Gondwana, also appears to be associated with the same preexisting zone of weakness (Figure 4.2b). The most recent nearby active deformation is found in the Okavango Rift Zone, approximately 300 km to the north.

With a hypocenter at approximately 29 km depth, this earthquake is unusually deep for a rifting event. Receiver functions suggest that the Moho depth in the epicentral region is approximately 45 km (Nguuri et al., 2001), placing this earthquake in the lower crust. Previous earthquakes have occurred in the lower crust and upper mantle of southern Africa (Yang Chen, 2010), suggesting that these regions can support high differential stresses despite high temperatures. Alternatively or in addition, the large depth of the Moijabana earthquake may be related to its location along the edge of the Kaapvaal craton. There is evidence that Proterozoic fold belts at the edges of cratons often host intraplate earthquakes (Mooney et al., 2012), and Craig et al. (2011) show that the deepest rifting earthquakes in southern Africa tend to concentrate along the edges of ancient cratons. In body wave and surface wave seismic tomography, these cratons show high-velocity lithospheric roots, assumed to represent lower temperature material in the upper mantle (James et al., 2001;

Priestley et al., 2006). Furthermore, heat flow measurements depict low heat flow values within the Kaapvaal craton and larger values moving away from the craton margin (Ballard et al., 1987). These observations support the notion that the cratons in southern Africa are strong, conductively cooled rock masses that have lower geotherms and locally deepen the maximum depth of the seismogenic portion of the lithosphere (Chen and Molnar, 1983).

While of lower magnitude, several historical earthquakes in this type of setting show close resemblance to this event. Two unusual normal-faulting earthquakes with magnitudes of M4.5 and M3.6 occurred in south-central Sweden in 1986. Much like the Moijabana earthquake, they occurred at 20-35 km depth within a Proterozoic shear zone separating two cratonic blocks, and the strikes of the nodal planes were parallel to the overall strike of the shear zone (Arvidsson et al., 1992). Similarly, the M5.4 Norseman and M5.2 Ravensthorpe earthquakes in southwestern Australia occurred as a result of normal faulting within a Proterozoic mobile belt on the boundary of an Archean craton, even though the overall stress regime in Australia is compressive (Clark, 2004). The Ravensthorpe event is thought to have a focal depth of 19 km (Clark, 2004). It is clear from earthquake catalogs that some stable continental regions are more likely than others to produce bimodal depth distributions with peaks of activity in the lower crust (Klose and Seeber, 2007). However, it appears that intraplate earthquakes in the depth and magnitude range of the Moijabana earthquake are quite rare (Robert Engdahl et al., 1998).

4.6.3 Possible sources of intraplate stress in southern Africa

The sources of stress that drive intraplate earthquakes are sometimes enigmatic. Plate boundary stresses from distant interfaces are thought to contribute to stress conditions in plate interiors (Zoback, 1992). In this case, the EARS may be contributing to stress conditions in central Botswana, even though the area is ∼300 km south of an actively rifting region (Figure 4.2). It is possible that the Moijabana earthquake points to the continuing southward propagation of the EARS (Bird et al., 2006), as is occurring in the Okavango Rift Zone in northern Botswana (Kinabo, Atekwana, et al., 2007). If this event represents an incipient rift process, then the recurrence interval for this type of earthquake is likely in the thousands of years given the slow geodetic rates of opening in the southern EARS (Stamps, Calais, et al., 2008). Other possible stressing mechanisms that have been suggested for intraplate earthquakes in general, and which may be related to the earthquakes in Botswana, include gradients in gravitational potential energy (Stamps, Flesch, et al., 2014) and density variations due to subsurface rift pillows (Zoback et al., 1999).

It is also possible that this earthquake represents a response to a geologically recent nontectonic stress or strength perturbation (Calais, Camelbeeck, et al., 2016). Redistribution of sediments at the Earth's surface, glacial isostatic adjustment and recent thermal weakening have been proposed as stressing mechanisms for other intraplate earthquakes, such as earthquakes in the Okavango Delta and the New Madrid earthquakes in the central United States (Calais, Freed, et al., 2010; Gumbricht et al., 2001; Liu and Zoback, 1997; Pollitz,

Kellogg, et al., 2001). It is difficult to clearly identify which stressing mechanisms could have ultimately brought the fault to failure in this earthquake.

Reliable in-situ measurements of stress are key to understanding the processes behind the Moijabana earthquake, but are rare in Botswana. The few available measurements suggest a stress state consistent with the earthquake's focal mechanism. Three over-coring measurements from mines were reported in Botswana in the World Stress Map 2008, including one close to the earthquake epicenter (Figure 4.1). This measurement shows the maximum horizontal stress well aligned with the stress field required to cause the earthquake (Heidbach et al., 2010). However, due to the large errors in over-coring measurements and difficulty verifying the details of the measurement procedure, the stress measurements in Botswana were down-graded to E-quality for the World Stress Map 2016 (Oliver Heidbach, personal communication, 2017), and replacement measurements have not been conducted. Models of deviatoric stresses in Africa, driven by gravitational potential energy from topography and crustal density variations, and geodetic motions also show general east-west tension in Botswana (Stamps, Flesch, et al., 2014). Further observational and theoretical constraints on the stress state are needed to provide a more detailed view of the stresses and associated deformation in this region.

Regardless of the original source of stress, a concentrated strain response in reactivated zones of weakness has long been considered as a possible contributor to the occurrence of intraplate earthquakes (e.g., Hinze et al. (1988)), and may be at play in the case of the Moijabana earthquake (Kolawole et al., 2017). The concept has been applied to specific earthquakes such as the New Madrid earthquake sequence (Kenner and Segall, 2000; Pollitz, Kellogg, et al., 2001), and has been proposed as a mechanism for persistent weakness of craton margins during supercontinent cycles (Audet and Bürgmann, 2011; Lenardic et al., 2000). We suggest that in the stress field imposed by the southward-propagating EARS and the regional stresses in southern Africa, the fault structures of the Proterozoic Limpopo orogen can accommodate strain between two more rigid cratonic blocks. This earthquake shows that Archean-age fabrics and geologic boundaries, when subject to a present-day stress field, are an important controlling factor for continental deformation (Begg et al., 2009).

4.7 Conclusion

The 3 April 2017 M6.4 Moijabana earthquake in central Botswana, with an unusually large magnitude and at a large depth, occurred in a region considered a stable continental interior. In order to study this earthquake and its tectonic setting, we compiled existing geophysical and geologic information and modeled the source parameters of the earthquake. We generated a stack of 20 Sentinel-1B InSAR interferograms over the source area. Using this ascending-orbit only dataset, we performed a 7-parameter inversion for strike, dip, rake, magnitude, and three location parameters of the earthquake source. We found that rupture planes close to either focal mechanism nodal plane were able to fit the data within expected noise levels because of the earthquake depth. We performed a joint finite source inversion

with InSAR and teleseismic data and found that the teleseismic waveform data favor a fault plane that dips to the southwest, consistent with aftershock relocations (Materna, Wei, et al., 2019). On the basis of geologic studies in the area and analogous intraplate earthquakes elsewhere, we suggest that the earthquake took place within a pre-existing zone of weakness from a Proterozoic collisional episode between two cratonic blocks. Future studies of the geology, geophysical data, and aftershock patterns may be helpful in further illuminating the geometry and long-term behavior of the fault that ruptured in the event.

Chapter 5

GNSS detection of hydrological loading in South Asia and Southeast Asia

5.1 Abstract

The elastic response of the lithosphere to surface mass redistributions produces significant deformation that can be observed in geodetic time series. This deformation is especially pronounced in Southeast Asia, where the annual monsoon produces large-amplitude hydrological loads. A network of about 20 continuous GNSS stations in Myanmar, India, Bangladesh, and Bhutan, operational since 2012, provides an opportunity to study the earth's response to these loads. In this study, we use GRACE gravity products as an estimate of long-wavelength surface water distribution and input this estimate into an elastic loading calculation. We compare the predicted vertical deformation with that observed with GNSS. We find that elastic loading from the GRACE gravity field is able to explain the phase and much of the peak-to-peak amplitude (typically 2-3 cm) of the vertical GNSS oscillations in northeast India and central Myanmar. GRACE-based corrections reduce the RMS scatter of the GNSS data by 30%-45% in these regions. However, this approach does not capture all of the variation in central Bangladesh and southern Myanmar. Local hydrological effects, poroelastic deformation, or differences in elastic properties may explain discrepancies between the GNSS and GRACE signals in these places. We find that a second independent hydrological loading model (LSDM) captures the amplitude but not the phase of the GNSS observations. The results of our calculations have practical implications for campaign GNSS measurements in Myanmar, which make up the majority of geodetic measurements at this point. By correcting for hydrological loading with independent models, we may be able to more accurately determine velocities and uncertainties from GNSS measurements in Southeast Asia, improving our understanding of regional tectonics.

5.2 Introduction

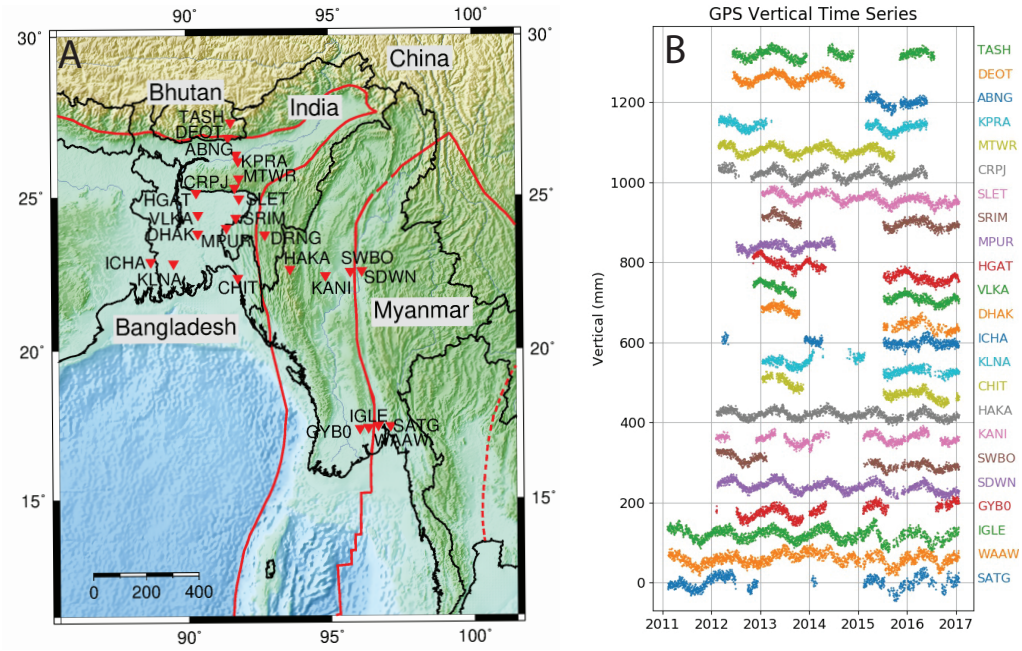

Figure 5.1: A) Map of Southeast Asia with GNSS stations of the MIBB (Myanmar, India, Bangladesh and Bhutan) network labeled. Faults representing global plate boundaries are shown in red (Bird, 2003). B) Vertical time series of GNSS stations shown in (A). Seasonal loading is evident in nearly every time series.

On seasonal timescales, hydrological cycles redistribute large masses of water, ice, and air around the globe. As these masses move, they impose loads on the solid earth, and the earth's deformation in response to the loads reveals information about both the sources of loading and the earth itself. For example, loading deformation provides a means of understanding the exchange of mass between the atmosphere, surface water, soil moisture, and groundwater (Argus, Fu, et al., 2014; Argus, Landerer, et al., 2017; Milliner et al., 2018). In terms of the solid earth, the surface response to time-varying loads also allows us to probe the elastic and viscoelastic structure of the crust and upper mantle (Chanard, Fleitout, Calais, Rebischung, et al., 2018; Chanard, Fleitout, Calais, Barbot, et al., 2018). Furthermore, hydrological loads can be important sources of stress on faults, contributing to the timing and occurrence of earthquakes and non-volcanic tremor (Johnson, Fu, et al., 2017; Pollitz, Wech, et al., 2013). For these applications and others, it is important to characterize the hydrological loading effects in geodetic data as accurately as possible.

For the study of tectonic processes like the earthquake cycle, it is important to determine

the effects of hydrological loading in order to correct for them and isolate earthquake cycle deformation (Fu and Freymueller, 2012). This can be a challenging task but is important in regions with transient earthquake cycle deformation and hydrological loads that vary from year to year (see Chapter 6 of this dissertation as one example). Accurate knowledge of hydrological loading in a region can also help with the interpretation of campaign-style Global Navigation Satellite Systems (GNSS) measurements, which contain both long-term tectonic deformation and seasonal loads but sample the displacements too sparsely in time to allow for separating them.

Hydrological processes generally produce mm-level deformation of the earth's surface through two dominant mechanisms. The first is elastic loading, in which the earth's surface is deflected downward due to the weight of a load placed on or near the surface (Becker and Bevis, 2004; Farrell, 1972). The second mechanism is poroelastic loading, in which the addition of groundwater produces upward deflection by filling pore spaces within the rock below, and is often observed in aquifer settings (Chaussard, Bürgmann, et al., 2015). Both mechanisms act primarily to affect the vertical component of GNSS measurements, although they also act in smaller amounts in the horizontal components (Wahr et al., 2013).

The typical methods used for studying hydrological loads in GNSS time series involve either mathematical functions or hydrological models from independent datasets to assess the effects of elastic loading at GNSS stations. One of the most commonly used external models comes from the Gravity Recovery And Climate Experiment (GRACE) and GRACE-Follow On missions, which produce spatiotemporal descriptions of the earth's gravity field and inferred redistribution of surface mass. A large body of research supports the general agreement between GRACE-based models of deformation and the hydrological loads observed in GNSS data (Chanard, Fleitout, Calais, Rebischung, et al., 2018; Fu and Freymueller, 2013; Fu and Freymueller, 2012; Gu et al., 2017; Hao et al., 2016; Tregoning et al., 2009). However, GRACE data is smooth in both time and space, having a spatial wavelength of 350-500 km. GRACE data does not capture local hydrological loading effects close to individual stations. Other models and techniques may be more appropriate at stations close to local sources of deformation or in regions where GRACE is insufficient.

In this work, we seek to evaluate the performance of several techniques to determine the seasonal deformation at GNSS stations in Southeast Asia (Figure 5.1), an important tectonic region that also has a strong monsoon climate and large seasonal loading deformation (Fu and Freymueller, 2013; Steckler, Nooner, et al., 2010). We compute the amplitude and phase of several models and compare them with GNSS time series and precipitation data. We assess how well the models reduce the variance of the GNSS data with the goal of separating the hydrological from the tectonic contributions to the deformation signal.

Station	Reason
DRNG	Time series is mostly gaps
BNGM	Insufficient data length
KHUL	Time series is mostly gaps
PUST	Time series is mostly gaps
RAJS	Time series is mostly gaps
JAML	Insufficient data length
JAFL	Insufficient data length
CHI0	Time series is mostly gaps

Table 5.1: Blacklist of unused GNSS stations for hydrological loading analysis.

5.3 Methods

5.3.1 GNSS Data

We use data from the Myanmar India Bangladesh Bhutan (MIBB) GNSS network operated by the Earth Observatory of Singapore (EOS). Most of the stations began operation in 2012 and remain in operation, although some have significant data gaps. We use stations until the summer of 2017, and we exclude stations with less than 2 years of data. The list of excluded stations is shown in Table 5.1.

The GNSS time series are processed with the GIPSY-OASIS software version 6.2 (Zumberge et al., 1997), with corrections applied for ocean tidal loading. At two stations in central Myanmar (SDWN and SWBO), we post-process the time series to remove earthquake cycle effects due to a M 6.8 earthquake in 2012. We fit and remove the coseismic offset using a Heavyside function and we model and remove postseismic deformation using an exponential function.

Where available, we also included stations from a separate GNSS network in Bangladesh that was installed in 2007 as part of the NSF- and UNAVCO-supported BanglaPIRE project. Most of these stations have data from 2007-2011. These data have also been processed using the GIPSY-OASIS software.

5.3.2 Hydrological Loading Models

We use two mathematical models to identify seasonal harmonic components in the GNSS time series. The first is a least-squares fit to the time series using Equation 5.1, which we use as the reference model for the hydrological loading. The w is the angular frequency associated with an annual period. The second method is a notch filter that preferentially suppresses frequencies at 1 year and 6 months. These techniques both seek to identify components of the time series with annual periods and remove them. However, the least-squares fitting is constrained to have constant-amplitude seasonal terms (Equation 5.1), while the filtering technique is theoretically able to adjust the amplitude of the seasonal terms year by year.

$$x(t) = Acos(wt) + Bsin(wt) + Ccos(2wt) + Dsin(2wt) + Et + F \tag{5.1}$$

We then evaluate several physically-based elastic loading models starting with the GRACE gravity derived estimate of monthly surface mass changes. Our models are derived from the three GRACE TELLUS Land Grid solutions from NASA's Jet Propulsion Lab (JPL), the Center for Space Research at the University of Texas, Austin (CSR), and the German Research Centre for Geosciences (GFZ) (Swenson and Wahr, 2006). We use 1°x1° grids from the GRACE Level 2 product from each processing center, expressed in units of cm of equivalent water thickness. The GRACE Level 2 data are corrected for ocean tidal loading, non-tidal ocean loading, and non-tidal atmospheric loading, meaning that contributions from those signals are not included in the product. We then compute the resulting elastic deformation assuming a Preliminary Reference Earth Model (PREM) (Dziewonski and Anderson, 1981) earth structure (Figure 5.2). We use Loading Love Numbers (Farrell, 1972) for the loading Green's functions following the formulation of Fu and Freymueller (2012). To derive the displacements, we sum the deformation due to every GRACE grid cell within 2000 km of a GNSS coordinate.

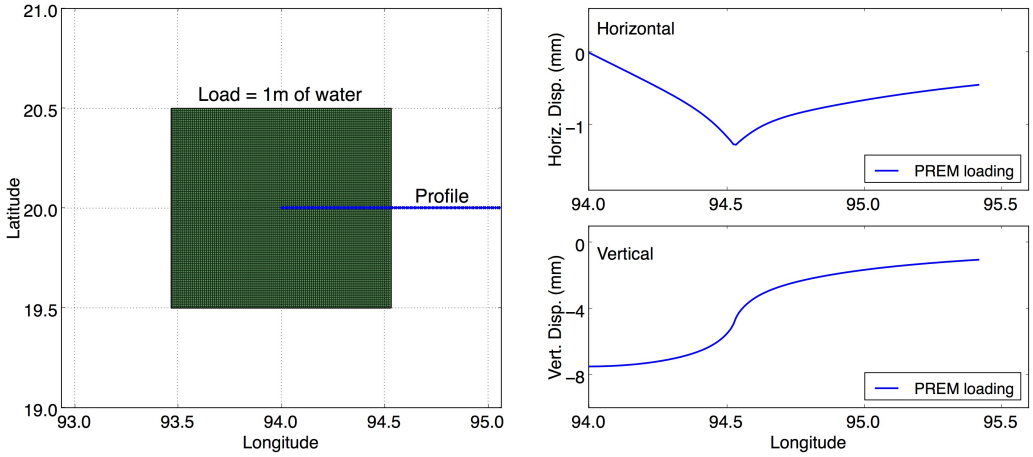

Figure 5.2: An example of a 1°x1° loading calculation on a PREM earth structure. The maximum vertical deformation due to the load is several times larger than the maximum horizontal deformation.

In constructing our GRACE models, we chose to apply the NASA-provided scaling grid to our dataset as recommended in the TELLUS documentation. The scaling grid is a product that restores some of the amplitude lost during the heavy smoothing applied earlier in the GRACE processing for removing north-south stripes in the GRACE TELLUS dataset (Landerer and Swenson, 2012). It is a simple time-independent scalar field multiplied by each grid cell in the dataset. However, we found that the amplitude of the multiplier in the scaling grids was unrealistically close to zero in central Myanmar, perhaps due to the

overall complexity of the data in this region (Felix Landerer, personal communication, 2017). Because hydrological loading deformation is most sensitive to the closest loads (Figure 5.2), the low-amplitude grid cells in central Myanmar resulted in very little hydrological correction being applied to the stations in that region. Therefore, while we use scaling grids at other stations, we manually force the stations KANI, SWBO, and SDWN in the affected area to use the GRACE data without scaling grids.

In addition to GRACE, we consider other physically-based elastic loading models from independent hydrological models. We try the Land Surface Discharge Model (LSDM), which estimates the elastic loading displacements driven by high-resolution hydrological models of terrestrial water storage (Dill and Dobslaw, 2013). The LSDM contains contributions from soil moisture, snow, and surface water stored in rivers and lakes. It also contains atmospheric loading contributions driven by the global operational weather model of the European Centre for Medium-Range Weather Forecasts (ECMWF). The loading displacements are computed using an elastic "ak135" earth structure (Kennett et al., 1995). Hydrological loading displacement time series for each coordinate are extracted from the LSDM website in the Center of Figure frame.

We assess the performance of each of these models by evaluating the reduction in the weighted root mean square error (WRMS) of each time series before and after correction. The percent improvement after correction shows the effectiveness of the seasonal correction technique. Because the background noise in the vertical component of the GNSS time series is generally 5-10 mm, and the amplitude of seasonal variation is on the order of 10 mm, a WRMS reduction of about 50% represents a nearly complete removal of seasonal variation from the time series.

5.4 Results

5.4.1 GNSS Results

Our findings show that GNSS stations across Southeast Asia contain significant deformation at seasonal periods (Figure 5.1), generally in phase with the local hydrological cycle. Peak uplift is around April, at the end of the dry period, and peak subsidence is around October, at the end of the monsoon (Figure 5.3, Figure 5.4). There is little phase shift observed across the region. The amplitudes of the vertical displacements are about 20 mm peak-to-peak (Figure 5.4).

5.4.2 GRACE Results

The GRACE models predict phases that are in good agreement with the observed GNSS data (Figure 5.4a). However, the amplitudes of the GRACE models are systematically lower than the GNSS, especially in Myanmar. We also find that the GRACE models across the region are more consistent in seasonal amplitude while the observed GNSS data is more

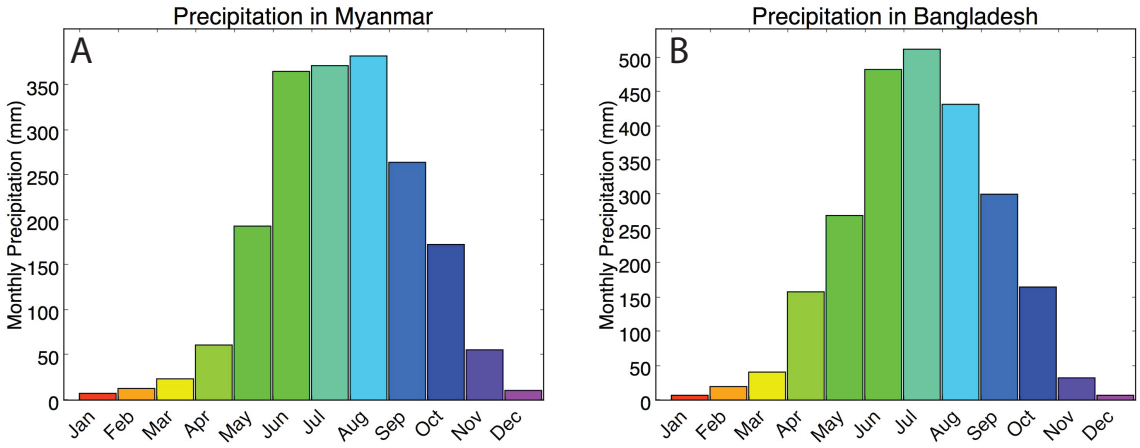

Figure 5.3: Average monthly precipitation in Myanmar and Bangladesh ("World Bank Group Climate Change Knowledge Portal" 2010)

spatially variable. We find that the three GRACE solutions (JPL, GFZ, and CSR) are extremely similar in their model predicted displacements at the GNSS stations (Sakumura et al., 2014). As one example, we show the results from the CSR solution (Figure 5.4).

When the detrended GRACE models are used to correct the detrended GNSS time series, the WRMS scatter in the time series is generally reduced by 10-50% (Figure 5.4b). The oscillations from hydrological loading are visibly reduced in the time series after the GRACE correction is applied (Figure 5.5). However, a few stations, typically those with misaligned phases between the GNSS and GRACE data, experience increases in WRMS scatter after seasonal correction by this technique (negative numbers in Figure 5.4b).

5.4.3 LSDM and Notch Filtering Results

We find that the LSDM model, unlike the GRACE model, fits the amplitude of the GNSS very well across the network in Southeast Asia. However, it reaches its peak phase 1-2 months earlier than the GNSS. Subsequently, the correction for seasonal loading using this technique is less effective (the WRMS scatter reduction is less), as the subtraction of a time series with improper phase results in introduced noise with seasonal periods.

We find that the Notch filter at 6-month and 12-month periods does not perform well on this dataset. The Notch filter generally does not identify large amplitudes associated with seasonal loading (see Figure 5.8). We suspect that this technique does not tolerate gaps very well, and therefore is unable to pick out seasonal oscillation in time series with missing data.

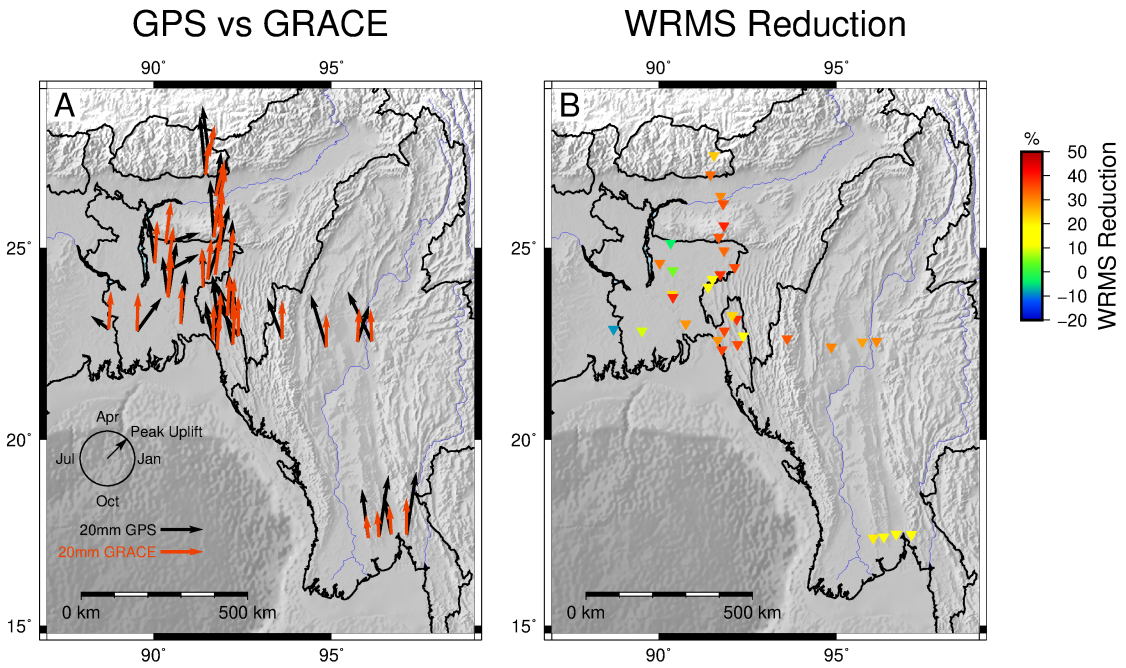

Figure 5.4: a) Average phase and amplitude results for GNSS observations using a least-squares model fit (black) and GRACE models computed from the CSR solution (red). The magnitude of the vector shows the peak-to-peak amplitude of the seasonal oscillation and the angle shows the phase by denoting the timing of peak uplift. b) WRMS reduction (in %) between the uncorrected and corrected GNSS time series using GRACE predicted displacements as corrections.

5.5 Discussion

We find that out of the model comparisons we tried, the GRACE-derived hydrological models are best able to capture the majority of hydrological signals in the MIBB GNSS data. Compared to the reference model of a least-squares fit (LSSQ), the GRACE prediction was generally able to model nearly all of the annual oscillation at most GNSS stations (Figure 5.7). The alternative LSDM model was less successful at reducing the scatter of the time series in large part because it contained a phase mismatch at most stations. The Notch filter was also less successful at reducing the scatter of the time series likely because it was unable to identify signals with annual period in the presence of large data gaps (Figure 5.7).

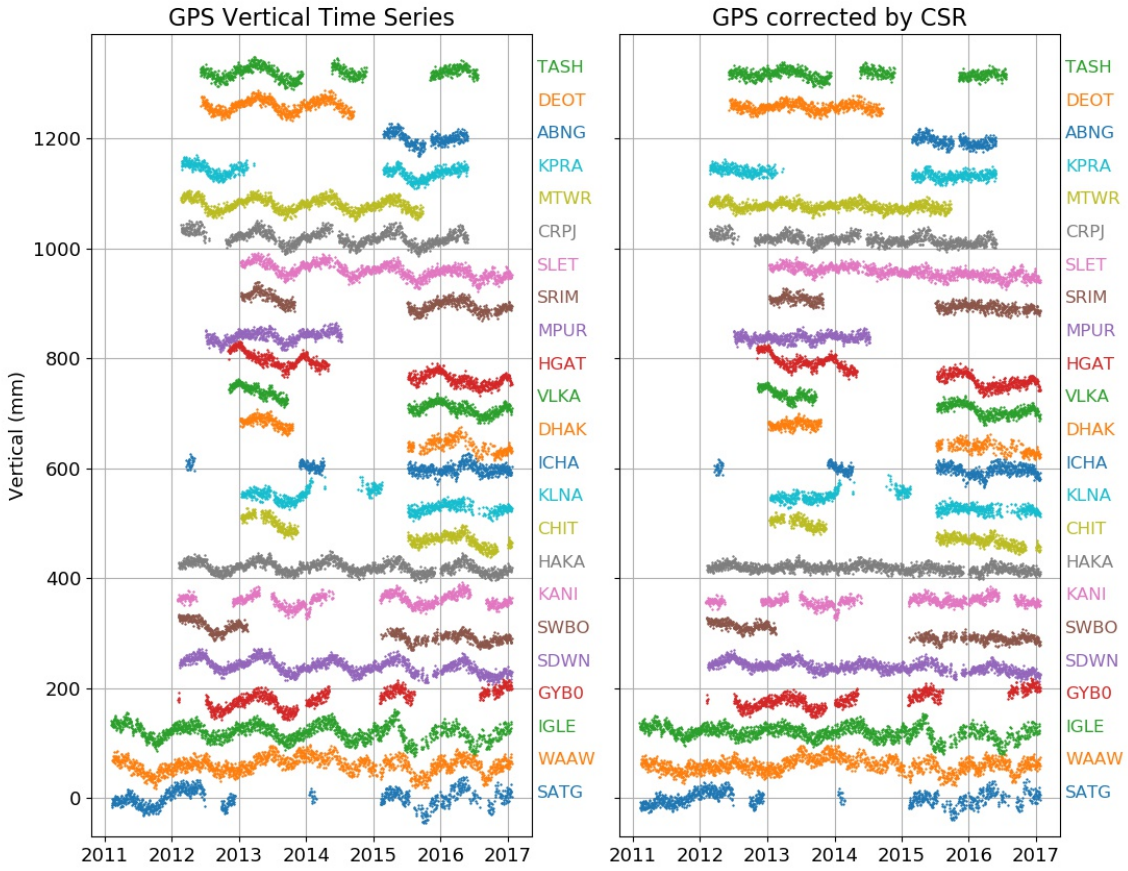

Figure 5.5: Left) GNSS vertical time series from the MIBB network spanning from 2012 to 2017. Right) The same time series corrected for hydrological motion by subtracting a model of hydrological loading derived from the GRACE CSR dataset. The hydrological loading signatures are generally reduced in the corrected time series.

One of the most interesting results of our analysis is the systematic difference in both phase and amplitude between the GRACE predictions and the LSDM predictions. The LSDM predicts peak uplift about 1-2 months earlier than GRACE but has a larger amplitude. We suspect several causes for this discrepancy. First, the LSDM contains the effects of atmospheric loading while the GRACE model does not. If the atmospheric loading is significant and out of phase with the other components of the hydrological cycle, then such a discrepancy might arise. However, the GNSS data are expected to have contributions from atmospheric loading; if atmospheric loading was significant, we would expect the phase of the

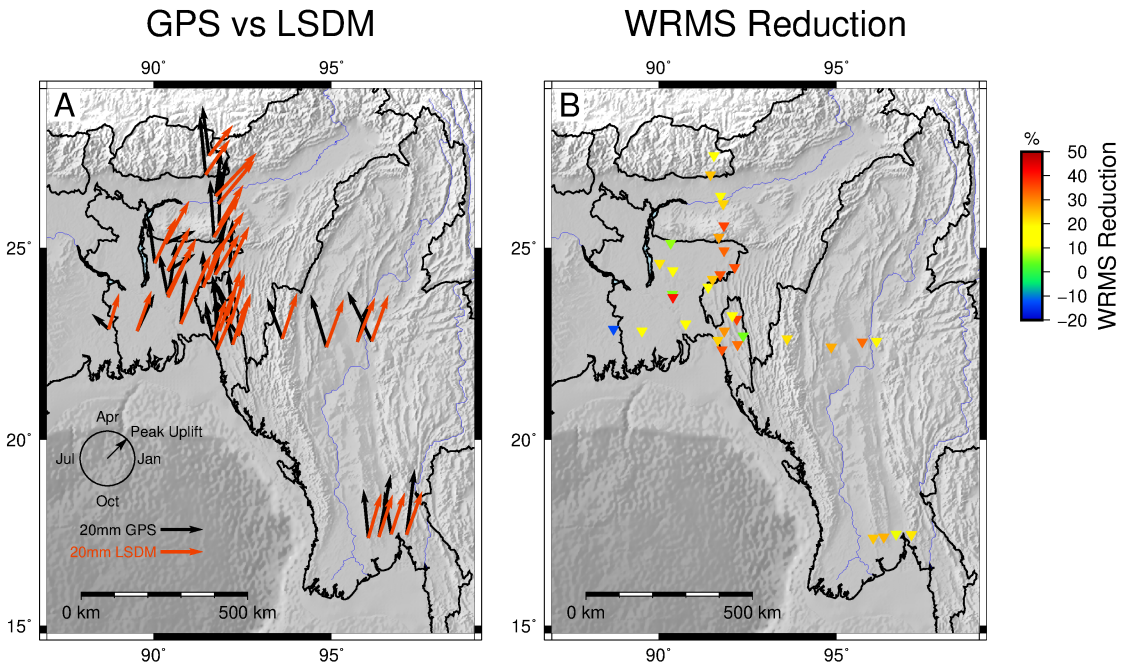

Figure 5.6: a) Average phase and amplitude results for GNSS observations using a least-squares model fit (black) and LSDM models (red). The magnitude of the vector shows the peak-to-peak amplitude of the seasonal oscillation and the angle shows the phase by denoting the timing of peak uplift. b) WRMS reduction (in %) between the uncorrected and corrected GNSS time series using LSDM predicted displacements as corrections.

LSDM to match the GNSS more than the phase of GRACE, which we do not see. Nonetheless, the atmospheric loading contributions may make up some of the difference between the two models. The phase of hydrological loading signatures in GNSS time series contains some inherent uncertainty, as the phase is thought to depend somewhat on processing strategy. Comparisons have found variation in phase between different solutions of the same raw data produced with different processing strategies (Van Dam et al., 2016). A future comparison of the MIBB data under multiple time series processing strategies would show the phase consistency of the hydrological signals and help illuminate the strengths and weaknesses of the LSDM and GRACE models in this region.

Second, the LSDM phase and amplitude could be responding to the surface water in the hydrological models used to drive it. We note that the LSDM phase is closer to the observed

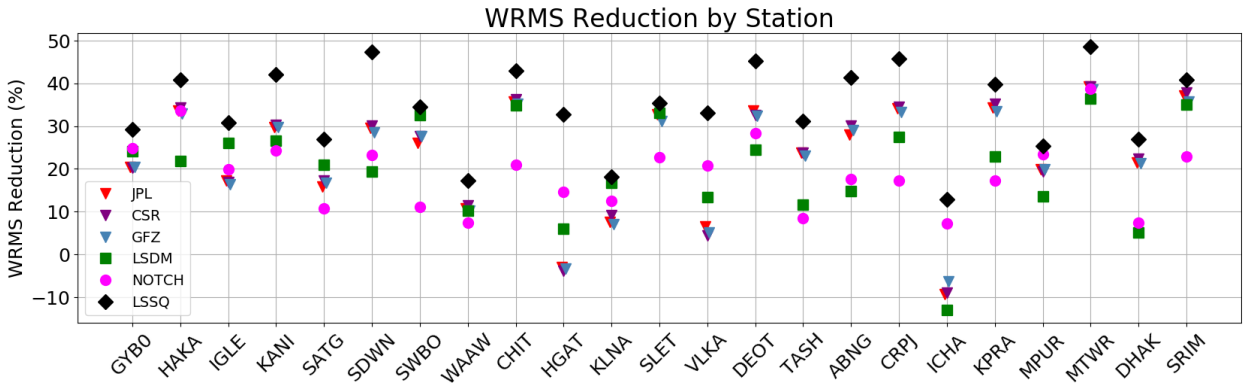

Figure 5.7: Station by station performance of each seasonal model. Higher values indicate a stronger model fit. The LSSQ model is the reference model, derived from fitting Equation 5.1 to the GNSS time series. The JPL, CSR, and GFZ models are three different GRACE solutions.

GNSS phase in central Bangladesh and southern Myanmar, while it is more discrepant in the rest of Myanmar and the foreland of the Indian Himalayas. This observation could be explained if the underlying components of the LSDM hydrological model for snow, atmosphere, and soil moisture contain phase discrepancies with the GRACE observations, but the surface discharge model has a closer phase to GRACE. In particular, the large quantities of surface water in the Ganges-Brahmaputra and Irrawaddy river deltas may be contributing to the better phase agreement with GNSS data in Bangladesh and Southern Myanmar respectively.

Third, the movement of groundwater may contribute to the phase difference between LSDM and GRACE. LSDM does not contain groundwater while GRACE is an aggregate of all water reservoirs. If the groundwater reservoirs take several months to respond to the onset of the seasonal monsoons, then we may expect the LSDM phase to be somewhat earlier than the GRACE phase, similar to our findings. However, further research separating the loading contributions from the atmosphere, soil moisture, snow, groundwater, and surface water is needed to more deeply understand the differences in phase between the two models.

The LSDM and GRACE models may have different amplitudes due to the different earth models used. The LSDM amplitudes are generally more in agreement with the GNSS, suggesting that the ak135 earth structure (used for the LSDM calculations) may be more appropriate in this setting and at these wavelengths than PREM (used for the GRACE models). On the other hand, the GRACE models better match in phase, suggesting that the underlying gravity observations are more consistent with the hydrological forcing experienced at GNSS stations. The GRACE amplitudes may be discrepant due to mis-modeled elastic structure for loads at these wavelengths.

We find systematic variations in the relationship between the GNSS observations and the GRACE models throughout the MIBB network. At some stations in central Bangladesh, we find that the GRACE predictions were larger in amplitude than the GNSS data (Figure 5.8).

This could occur potentially through poroelastic effects in basin sediments of the Ganges-Brahmaputra delta, or through earth model errors. To produce a mismatch in this direction, the earth model (PREM) must be too compliant compared to the real earth, i.e., the real earth must be stiffer than the model. Given that these stations are located in one of the world's deepest basins and that basin sediments are generally softer than reference earth materials (Mukherjee et al., 2009), we doubt that the earth model is too compliant. We suggest that poroelastic effects in the Ganges-Brahmaputra delta might also be producing significant displacements, acting in the opposite sense and serving to offset some of the purely elastic hydrological loading deformation expected, e.g., Chaussard, Bürgmann, et al., 2015.

On the other hand, at stations in southern Myanmar, the GNSS data showed seasonal amplitudes much larger than the GRACE predictions (Figure 5.8). This outcome could be due to several effects. First, local effects from small water bodies below the resolution of GRACE could be contributing to the elastic loading at particular stations. Second, GRACE gravity data in this region could be losing amplitude due to smoothing where the land grids meet the coastline. Third, the PREM earth model could be too stiff for the region at hand. In the case of southern Myanmar, in the center of the Irrawaddy delta, any or all of these effects could be taking place. The Irrawaddy river system is smaller than the Ganges-Brahmaputra in terms of drainage area and discharge (Hori and Saito, 2007), so it could be more difficult to capture in the low-resolution GRACE data. We suspect that the earth model or the sub-resolution water bodies could be contributing to the GRACE discrepancies in this area.

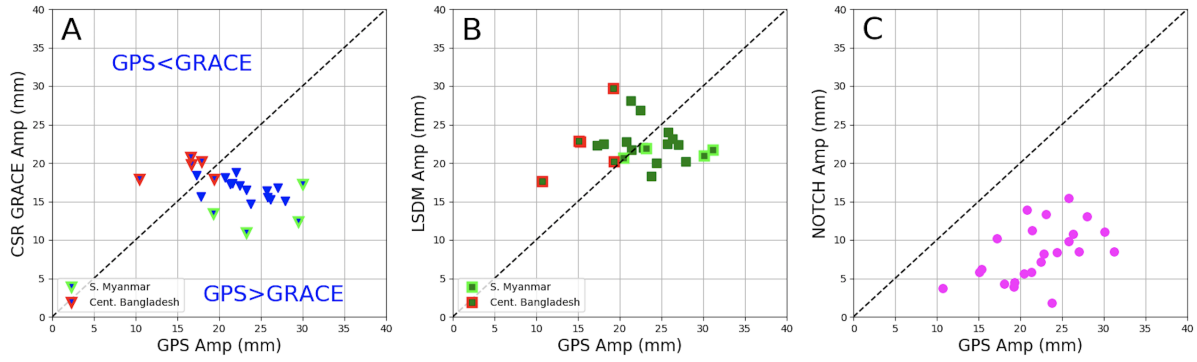

Figure 5.8: Comparisons of seasonal amplitude between the observed GNSS data and various models of the hydrological loads. A) GPS Amplitude vs. GRACE amplitude from the CSR solution. B) GPS Amplitude vs. LSDM amplitude. C) GPS Amplitude vs. the Notch filtering results of the GPS time series.

The research presented here could be used in a number of applications. A combined GNSS- and GRACE-derived estimate of total water storage could be higher resolution than a GRACE-based estimate alone (Fu, Argus, et al., 2015). An improved understanding of vertical seasonal motion could also be used to extract more accurate tectonic velocity measurements from time series that contain a mix of hydrological loading effects and earthquake

cycle deformation such as postseismic transients. These effects are especially pronounced when campaign GNSS time series are considered. From a hazards perspective, it is important to have as precise a velocity field as possible in Myanmar given that significant first-order questions still remain about the present-day activity of the Arakan megathrust (Mallick et al., 2019; Steckler, Mondal, et al., 2016). As more continuous and campaign GNSS data is collected in Myanmar in the future, these corrections will help to further characterize tectonic activity.

The study of vertical velocities from GNSS time series is also a general frontier in geophysical research that would benefit from accurate characterization of hydrological loads in Southeast Asia. Vertical velocities can reveal regions of elastic strain accumulation, active mountain-building, mantle upwelling, groundwater withdrawal, glacial isostatic uplift, sea level change, and more (Hammond et al., 2016; Higgins et al., 2014; Hill et al., 2011; Serpelloni et al., 2013). In and around Myanmar, little is known about the processes affecting vertical deformation and the rheology of the crust. Separating the annual and multiannual hydrological signals from the existing GNSS datasets will provide insight into these questions by revealing regions where present-day vertical motion is both significant and due to tectonics.

Chapter 6

Dynamically Triggered Changes of Plate Interface Coupling in Southern Cascadia

Submitted as: Materna, K., N. Bartlow, A. Wech, C. Williams, and R. Bürgmann, Dynamically Triggered Changes of Plate Interface Coupling in Southern Cascadia, submitted to Geophysical Research Letters, 2019.

6.1 Abstract

In Southern Cascadia, precise GPS measurements spanning about 15 years reveal steady deformation due to locking on the Cascadia megathrust punctuated by transient deformation from large earthquakes and episodic tremor and slip events. Near the Mendocino Triple Junction, however, we recognize several abrupt GPS rate changes that reflect a different process. After correcting for earthquakes and seasonal loading, we find that several dozen GPS time series show spatially coherent east-west velocity changes of about 2 mm/yr, and that these changes coincide in time with regional M>6.5 earthquakes. We consider several hypotheses and propose that dynamically triggered changes in megathrust coupling best explain the data. Our inversions locate the coupling changes slightly updip of the tremor-producing zone. We speculate that dynamic shaking near the tremor region may provide a mechanism. Observations of transient coupling changes are rare and challenging to explain mechanistically but have important implications for earthquake processes on faults.

6.2 Introduction

In subduction zones, seismically coupled regions of the megathrust accumulate strain during the interseismic period of the seismic cycle. The resulting slip deficit must eventually be released, either through coseismic slip, postseismic slip, or a wide spectrum of recently

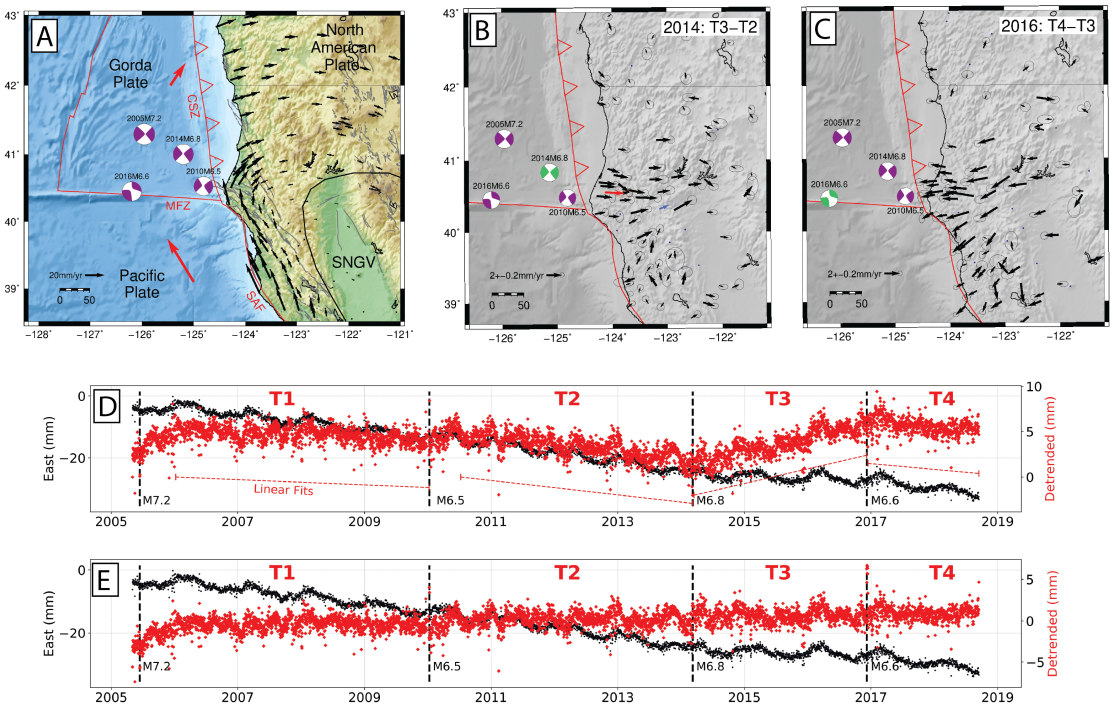

Figure 6.1: a) Tectonic setting of the Mendocino Triple Junction, located at the intersection of the San Andreas Fault (SAF), the Mendocino Fault Zone (MFZ), and the Cascadia Subduction Zone (CSZ). The black velocity vectors show the PBO velocity field in the Sierra Nevada Great Valley (SNGV) reference frame, converted using the Euler Pole from Dixon et al. (2000). b and c) Velocity changes (T3-T2 and T4-T3) from the PBO solutions with least-squares seasonal removal, shown with 1-σ confidence ellipses. d) Time series of east component for station P160 (red arrow in (b)). Time series after earthquake removal is shown in black and the detrended and de-seasonalized east component is shown in red, with dashed lines indicating the periods used for slope estimation. e) Residuals to linear fits in Figure 6.1.

discovered slow slip processes such as slow slip events (SSEs) (Gomberg et al., 2016; Obara and Kato, 2016; Bürgmann, 2018). The spatiotemporal evolution of slip deficit (or coupling)

is directly related to earthquake and tsunami hazards, and thus is important to understand.

SSEs are temporary phenomena. They display a range of time scales lasting from weeks to years (Bartlow et al., 2011; Fu and Freymueller, 2013; Hirose and Obara, 2005; Radiguet et al., 2012), but the subduction interface generally returns to the previous coupling state after SSEs are completed. An SSE may occur spontaneously or be triggered by the passage of regional or teleseismic seismic waves (Araki et al., 2017; Itaba and Ando, 2011; Wallace et al., 2017). However, outside of slow slip episodes and postseismic slip, fault coupling on the megathrust is often assumed to be constant during the interseismic period.

Here we document observations of abrupt changes in GPS velocities at the Mendocino Triple Junction (MTJ) of northern California that endure for years, challenging the assumption of constant interseismic coupling. We relate these velocity changes to changes in the state of coupling at the Cascadia Subduction Zone (CSZ) plate interface, separate from the short-term episodic tremor and slip (ETS) events observed in this region (Brudzinski and Allen, 2007). This area recently experienced four offshore M>6.5 earthquakes in 2005, 2010, 2014, and 2016 (Figure 6.1). The largest velocity changes in the GPS time series coincide closely in time with two of these offshore earthquakes. We find that Coulomb stress interactions, viscoelastic relaxation, afterslip, reference frame errors, or multiannual hydrological load changes cannot explain the observations. Instead, we propose that these observations represent the first report of a single region undergoing dynamically induced increases and decreases in plate coupling on years-long timescales.

6.3 Methods

6.3.1 GPS Data

We analyzed continuous GPS time series from multiple processing centers and reference frames. We focused on the Plate Boundary Observatory (PBO) combined solutions in the NAM08 reference frame (Herring, Melbourne, et al., 2016) and University of Nevada Reno (UNR) solutions in the NA12 and IGS08 reference frames (Blewitt et al., 2018), but we also analyzed the PBO Central Washington University (CWU) and New Mexico Tech (NMT) solutions. Our dataset extends through January 2019. For the NMT and PBO combined solutions, we only consider time series through their official end dates in mid-September 2018.

We corrected offsets due to antenna changes and earthquakes by applying offsets from published tables for the NMT, CWU, and PBO solutions (ftp://data-out.unavco.org/pub/products/offset/) For the UNR data, we solved for offsets using mean positions 10 days before and after the provided offset times (http://geodesy.unr.edu/NGLStationPages/steps.txt).

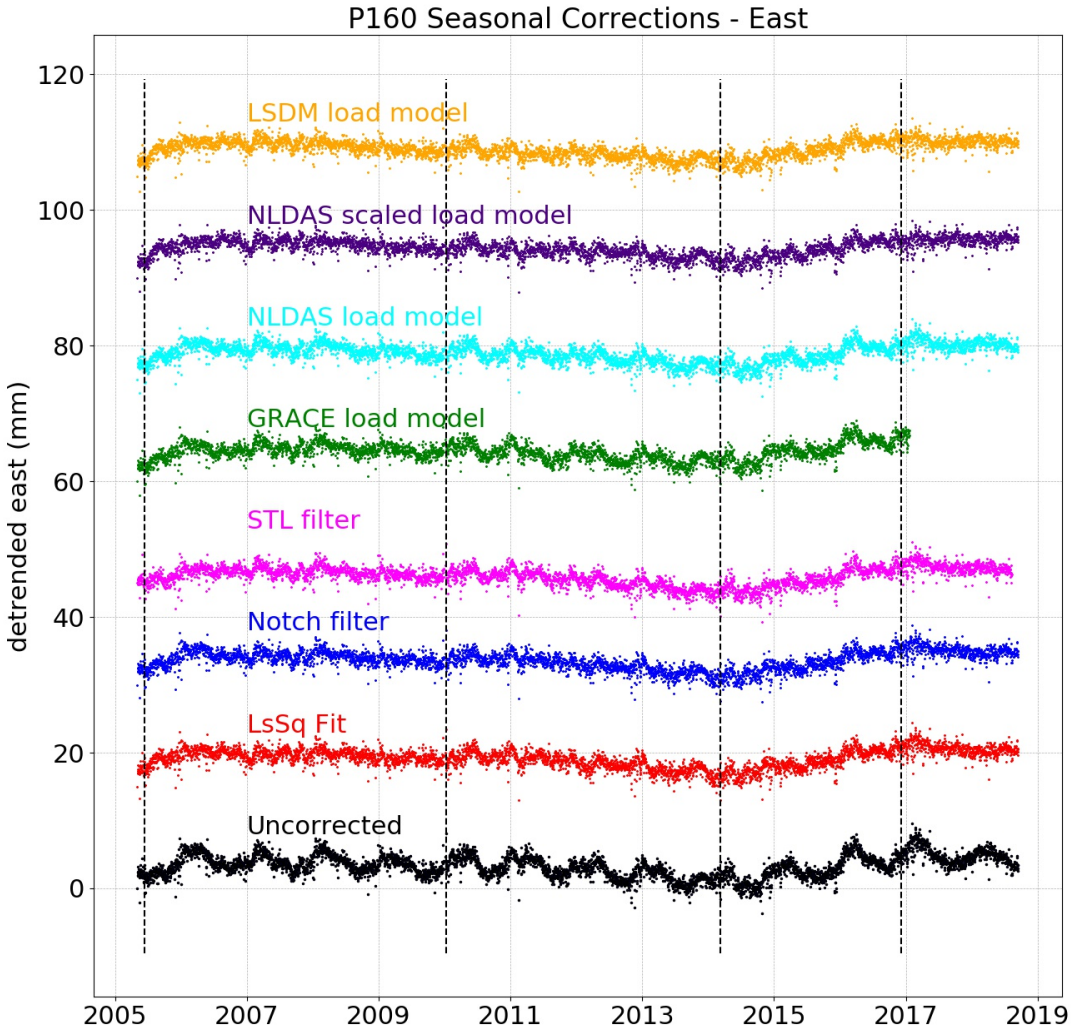

Figure 6.2: The east component of the GPS time series at station P160 corrected for seasonal components by multiple techniques. Vertical lines represent the timing of the four major earthquakes. The increased velocity in the east component between 2014-2016 is visible in each time series, including uncorrected. The lower resolution GLDAS model is not available for this station due to its proximity to the coastline and the edge of the GLDAS model domain.

6.3.2 Correction of Seasonal Terms and ETS Events

We estimated seasonal and longer-term hydrological corrections for each component of each time series using multiple methodologies. Inter-annual seasonal variation is important

2012-10-23 to 2012-11-01	2013-05-23 to 2013-06-08	2014-01-07 to 2014-01-12
2014-02-25 to 2014-03-02	2014-09-06 to 2014-09-16	2015-04-23 to 2015-05-17
2015-12-22 to 2015-12-27	2016-08-10 to 2016-08-20	2017-04-20 to 2017-05-05
2017-11-05 to 2017-11-21	2017-12-20 to 2018-01-06	2018-07-01 to 2018-07-15

Table 6.1: Times of ETS events identified in the red box in Figure 6.3.

during this time period because of the effect of California's drought on GPS positions from 2011-2015 (Argus, Landerer, et al., 2017; Zou et al., 2018). Therefore, we employ a number of physics-based loading models which include inter-annual variations, as well as a least-squares technique with no inter-annual variation, to correct for this motion. We also performed a simple correction for 12 ETS offsets in the time series.

We first tried to remove seasonal components from each time series using a simple least-squares fitting of the time series as a sum of linear, annual, and semiannual terms. Next, we tried a notch filter with notch frequencies at 1 year and 6 months. We also computed and removed the seasonal components using a seasonal-trend decomposition based on Loess smoothing (STL) (Cleveland et al., 1990). We set the tunable parameter ns to a value of 25. We also performed our computations on the time series with no seasonal corrections in order to understand the impact of seasonal corrections (Figure 6.2).

To consider physical processes due to multi-annual hydrology, we performed seasonal correction using the PBO H2O loading products from the NLDAS and GLDAS hydrological models (ftp://data-out.unavco.org/pub/products/hydro/) (Puskas et al., 2017). These models contain the loading contributions of water in the soil, snowpack, and vegetation. The NLDAS has higher spatial resolution over North America, while the GLDAS has lower spatial resolution but is global (Mitchell, 2004).

We also performed a seasonal correction using geophysical fluid loading time series produced by GFZ in the center-of-figure frame (http://rz-vm115.gfz-potsdam.de:8080/repository). More details of this product can be found in Dill and Dobslaw (2013). This result is named "LSDM" in our figures after the Land Surface Discharge Model, the hydrological model used to produce it.

We also tried a forward model loading calculation using the GRACE gravity field calculated at each station's coordinates (green line, Figure 6.2). At each station, we computed a load-induced deformation time series from a PREM elastic earth driven by the JPL mascon GRACE solutions with scaling grids applied (Fu and Freymueller, 2012; Swenson and Wahr, 2006). We then used this modeled time series for correcting seasonal components and comparative forward-modeling of the velocity change fields due to hydrological loading. However, it is not our preferred model for general correction of seasonal terms because of the low spatial resolution of the GRACE gravity field and the limitation of the dataset ending during 2017.

Finally, we performed a basic correction for ETS events in the GPS time series. We determined that an ETS event occurred when the Mendocino tremor counts in our revised

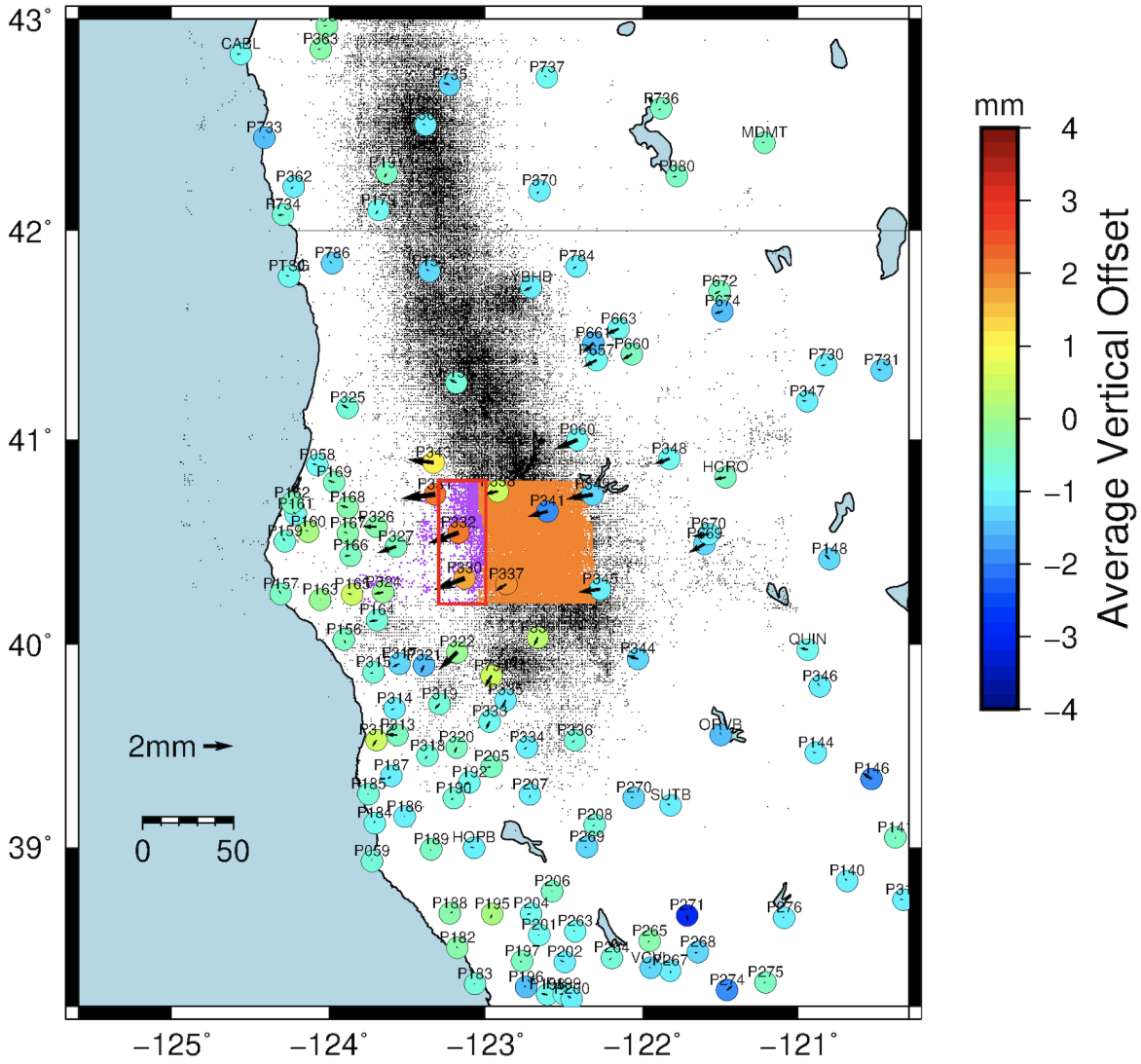

Figure 6.3: Average GPS offsets in the east, north, and up components during times of high tremor counts in the red box. The average ETS offsets shown here are used to correct the GPS time series for offsets during known ETS times. The tremor catalog is plotted in dots, with purple representing 24-35 km depth and orange representing 35-65 km depth on the McCrory et al. (2012) plate interface geometry.

tremor catalog (Wech, 2010)(Section 6.3.5) were above 10 per day. A total of 12 ETS intervals were identified (Table 6.1). The search area is shown in Figure 6.3. At each interval, we fit an offset to the seasonal-corrected time series, first removing outliers above 2 mm and then finding the difference between the 30-day averages before and after the offset time. We

Epoch	Time range (yyyy-mm-dd)	Time delay after earthquake
T1	2006-01-01 to 2010-01-10	6 months
T2	2010-07-10 to 2014-03-10	6 months
T3	2014-03-17 to 2016-12-08	7 days
T4	2016-12-15 to 2018-09-15	7 days

Table 6.2: Times used for the 4 velocity epochs defined in this study. The time range in the second column includes a delay imposed after each mainshock for avoiding postseismic transients.

solved for offsets in all three components at each ETS event. However, we found that fitting individual offsets for each ETS event introduced biases into the analysis, likely due to aliased signals from hydrological loading. Therefore, we used the average of the offsets during the 12 ETS intervals as a "characteristic" offset. The characteristic offsets at each station in east, north, and vertical are shown in Figure 6.3, and show the pattern of deformation expected for slow slip events in the Mendocino region. These offsets were removed from the GPS time series at the times of the 12 major ETS events before estimating the velocity changes that we later modeled through inversions.

6.3.3 Velocity Change Timing and Estimation

After removing seasonal corrections and offsets from the timeseries, we observed consistent velocity changes across much of the MTJ region (Figure 6.1). We estimated the timing of these changes by looking for "turning points" in the individual low-pass filtered time series. We filtered the detrended and de-seasonalized data with a low-pass Butterworth filter using a filter wavelength of one year. We then identified the position of the turning point by finding the point of maximum curvature of the filtered and detrended time series within 1 year of the 2014 and 2016 earthquakes. We recorded the relative time of the turning point compared to the earthquake time; a relative time of 0 represents a slope-change exactly coinciding with the time of the earthquake.

We found that most stations at the MTJ have a turning point within $\sim$60 days of the 2014 and 2016 earthquakes (Figure 6.4). We then defined four "velocity epochs" for the subsequent analysis based on the occurrence times of the four offshore M>6.5 earthquakes (Table 6.2). We excluded 6 months of data after the 2005 and 2010 earthquakes to avoid postseismic transients, and 7 days after the 2014 and 2016 earthquakes (Figure 6.1d). Finally, we estimated velocity differences between the four epochs by differencing the slopes of the corrected time series during each epoch.

6.3.4 Excluded Stations

Before the final analysis, some stations were excluded due to noise or unmodeled signals in their time series. For example, volcano-monitoring stations around Mt. Shasta and Mt.

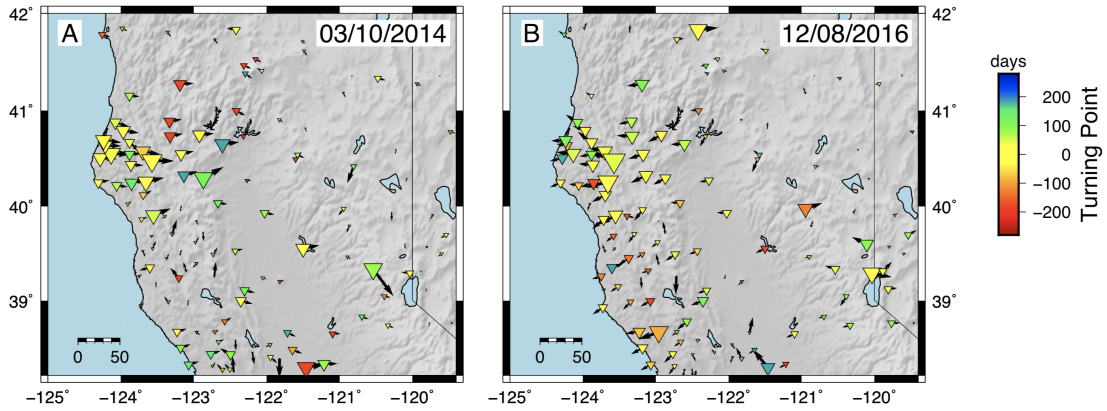

Figure 6.4: Timing plots of the slope change in the east component of each station's time series. A value of 0 signifies that the turning point in the detrended time series coincides with the offshore earthquakes in 2014 and 2016. Red colors signify times before the earthquake, and blue colors after the earthquake.

Lassen were excluded because of snow-related artifacts, as were stations with landslide signatures or large deviations from linear trends. Stations were excluded at particular velocity epochs if the residuals to a linear fit for either velocity epoch had a standard deviation larger than 5 mm. We also excluded time intervals that had less than 1 year of data for velocity estimation. These criteria typically excluded ∼5% of the stations.

6.3.5 Uncertainties on Velocity Changes

To compute uncertainties, we first determined velocity uncertainties in each epoch and then estimated uncertainties of the velocity differences by adding the velocity uncertainties of the two relevant epochs in quadrature. Because GPS time series contain correlated noise, such as flicker and random walk noise from processing errors and monument motions (Langbein and Svarc, 2019), the formal velocity uncertainties from the least-squares inversion are unrealistically small. It has been found that for GPS velocity estimation, formal uncertainties underestimate the true uncertainties by a factor of 2-11 (Johnson and Agnew, 1995; Mao et al., 1999; Williams et al., 2004). We derive more realistic uncertainties on our velocity estimates using the Allan variance of the rate (AVR) (Hackl et al., 2011), a modification of a technique developed for uncertainties on clocks and gyroscopes. It closely reproduces the uncertainty estimates of maximum likelihood estimators for uncertainties on GPS time series, but is computationally cheaper (Hackl et al., 2011). For most stations in Northern California, this procedure results in 1-sigma uncertainties of the velocity differences of about 0.3 mm/yr.

6.3.6 Tremor Catalog

In order to compare coupling changes with tectonic tremor in space and time, we reevaluated the tremor catalog in Wech (2010) from January 2015 to January 2018. A number of seismic stations in Mendocino became unavailable during mid-2016, requiring a revision of the numerical thresholds used in the tremor detection procedure. Furthermore, we imposed a new detection criterion that decreased the rate of false tremor detections due to spurious data from stations near the MTJ. Outside of the 2015-2018 window, we used the existing 2012-2019 tremor catalog (Wech, 2010).

6.3.7 Mechanical Modeling of Velocity Differences

To model the GPS velocity changes, we performed weighted non-negative least-squares inversions using both homogeneous and heterogeneous elastic Green's functions, with and without correcting for ETS offsets. Weights are the inverse of the uncertainties on the velocity changes, normalized so the average weight is 1. The model fault geometry is a triangular mesh approximation of the McCrory et al. (2012) geometry, with an assumed slip direction fixed on each subfault using the Juan de Fuca - Oregon Coast Block Euler Pole reported in McCaffrey, Qamar, et al. (2007).

We applied Laplacian smoothing regularization, with the rows of the discrete Laplacian corresponding to each subfault additionally weighted by the inverse of the median value of the Green's functions associated with the subfault. This additional weighting ensures that less resolved subfaults, as indicated by small amounts of surface motion at observable sites, are smoothed more. A smoothing parameter weights minimizing the Laplacian of the slip distribution relative to fitting the data. The smoothing parameter is chosen via an L-curve analysis, choosing the smoothest model that does not substantially increase the RMS value of the residuals. A smoothing parameter of 800 was chosen for all inversions.

Homogeneous Green's functions were calculated using triangular dislocations in an elastic half-space (Thomas, 1993). Heterogeneous Green's functions were calculated using the PyLith finite element software (Aagaard et al., 2013; Aagaard et al., 2017a; Aagaard et al., 2017b), with density (and by extension, shear modulus) estimated via empirical relationships with v_p and v_s (Brocher, 2005; Stephenson, 2007). The v_p and v_s values were taken from the model of Stephenson (2007) with the v_p and v_s values at 60 km (deepest depth of the model) extended to 400 km depth. Topography is ignored. The mesh used by PyLith to generate the Green's functions is at a much finer resolution than the mesh used in the inversions because PyLith impulses are applied at vertices rather than over a subfault. The PyLith Green's functions are then integrated over each triangular subfault to calculate the heterogeneous Green's functions associated with each.

Time	Mag.	Center Loc.	Center depth (km)	Strike,Rake,Dip	Slip (m)
2005-06-15	7.2	-125.953, 41.292	16.0	48, 7, 82	1.973
2010-01-10	6.5	-124.693, 40.652	24.0	230, 11, 86	0.663
2014-03-10	6.8	-125.134, 40.829	16.4	228, -2, 79.0	1.124
2016-12-08	6.6	-126.194, 40.454	8.5	95, -159, 81.0	0.850

Table 6.3: Earthquake source parameters used for inputs to Coulomb stress modeling. Location and geometry parameters are from the USGS moment tensor solution; slip is computed for rectangular fault plane from scaling relationships for strike-slip ruptures in Wells and Coppersmith (1994).

6.3.8 Coulomb Stress Modeling

Static stress changes on the Cascadia subduction thrust after the 2014 and 2016 earthquakes were computed using an elastic half-space model (Okada, 1992). We assumed source fault planes constrained by focal mechanisms in the USGS catalog and aftershock locations, and we used source dimensions and uniform-slip values computed from rupture scaling relationships (Wells and Coppersmith, 1994). Coulomb stress changes were computed on an idealized CSZ geometry along a slip vector assuming pure dip-slip motion for the Gorda plate. The earthquake source parameters are shown in Table 6.3, and the resulting Coulomb stress changes are shown in Figure 6.10.

6.4 Results

We identify three abrupt velocity changes in the cleaned, deseasonalized and detrended GPS time series, with the largest of these changes occurring in early 2014 and late 2016. As described in the methods, the onset time of these velocity changes is consistent with the timing of the 2014 and 2016 offshore earthquakes (Figure 6.4). In the two-year period starting in early 2014 (time period T3 in Figure 6.1d), the time series of almost two dozen GPS stations indicate steady eastward velocities that are 2-3 mm/yr larger than in the prior time period T2 (Figure 6.1b). Unlike typical postseismic transients, this signal does not show significant temporal evolution (Figure 6.1d, Figure 6.5). After the 2016 earthquake (time period T4), the eastward velocities reverse some of the velocity change observed in 2014 (Figure 6.1c). To first order, the results are not sensitive to the technique used for seasonal removal, and the rate changes are visible by eye in many time series prior to any seasonal removal (Figure 6.2).

After setting aside the 6-month postseismic period following the 2010 earthquake, time period T2 is also associated with a small westward velocity change at about 10 stations at the MTJ (T2 minus T1 in Figure 6.6), but these velocity changes are too small to reliably interpret. The 2005 earthquake may have also been associated with local velocity changes. However, only a few stations were installed prior to this earthquake and none have more

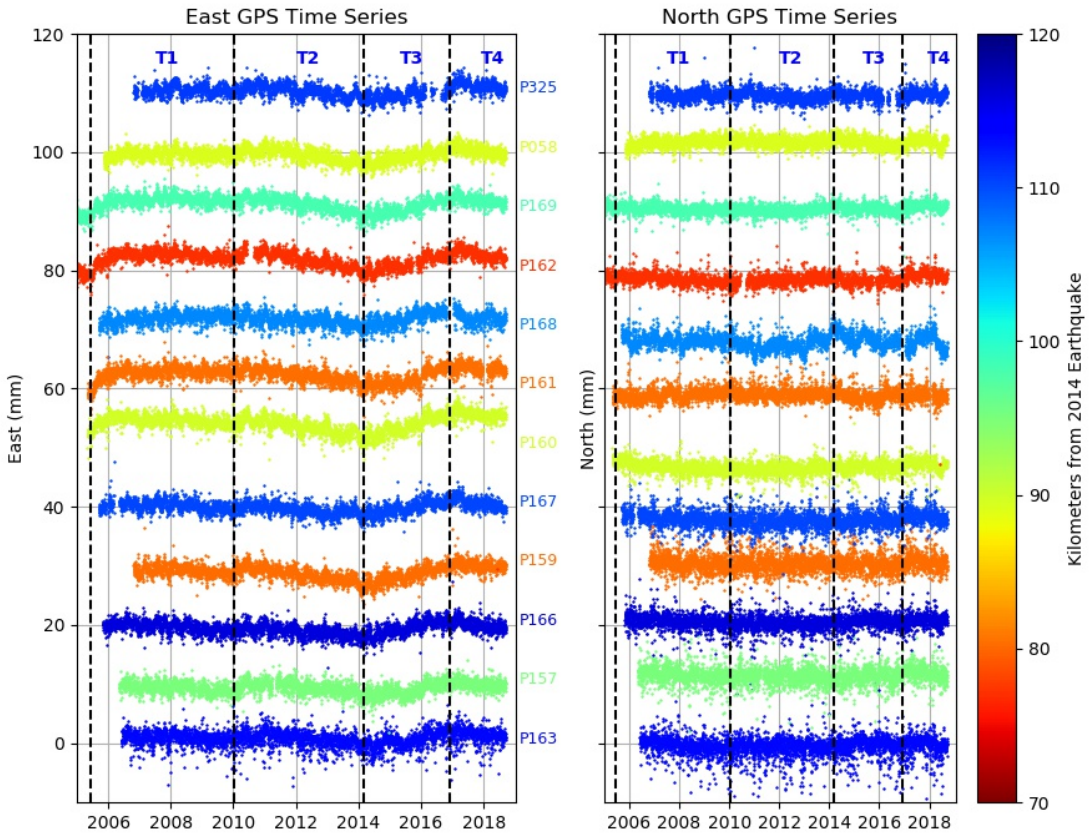

Figure 6.5: Detrended east and north time series for GPS stations at the MTJ, shown after correction of seasonal components by least squares fitting. All time series have been detrended and earthquake offsets have been estimated and removed. The black dashed lines represent the times of the four major earthquakes in the study window (Table 6.2).

than a year of data before the event, so we are unable to estimate these velocity changes. Instead we focus on understanding the larger velocity changes in 2014 and 2016.

Inverting the observed velocity changes for coupling changes on the plate interface indicates that the 2014 velocity change was associated with a coupling increase while the 2016 velocity change was associated with a coupling decrease (Figure 6.7). The coupling change distributions for the 2014 and 2016 events are similar spatially, although with different amplitudes and signs. The coupling changes are predominantly concentrated in a single "spot" on the plate interface near 40.3°N, 123.3°W, located at about 25-28 km depth just updip of the main ETS zone. Our preferred model (Figure 6.7) utilizes heterogeneous Green's func-

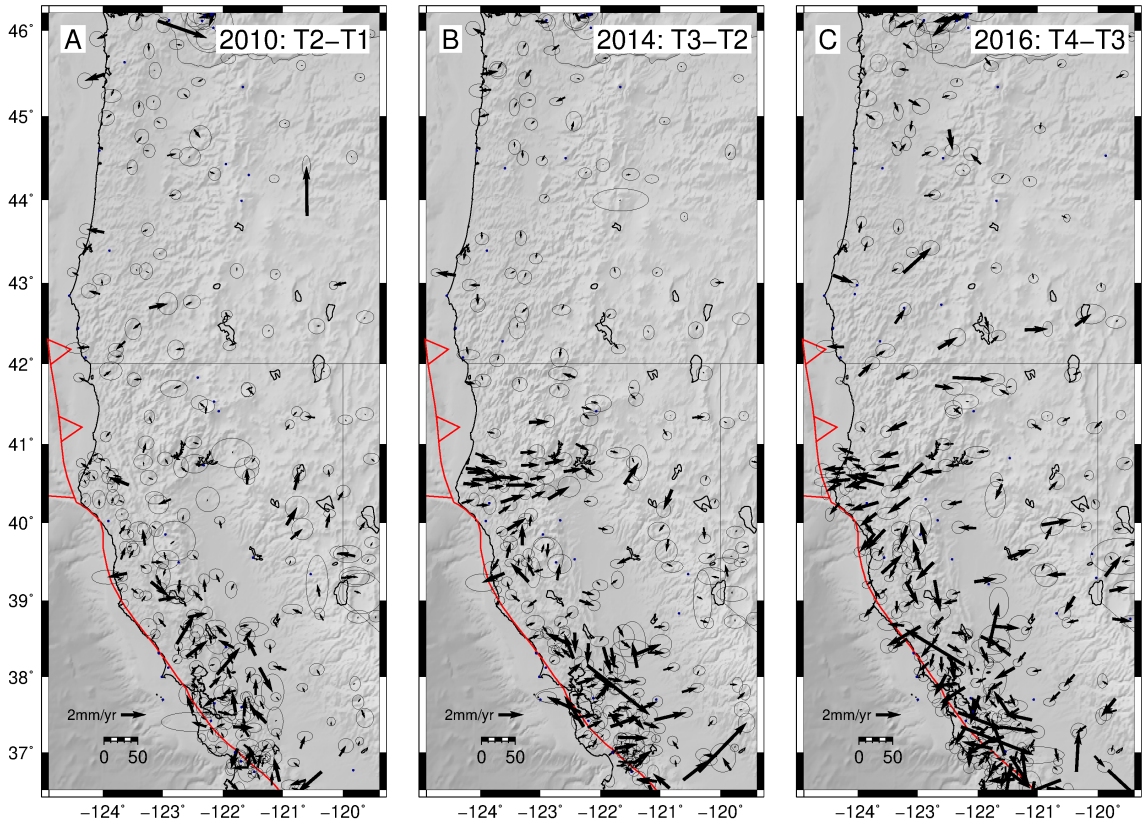

Figure 6.6: Northern California and Oregon velocity differences between T1, T2, T3, and T4 (see Figure 6.1 lower panel for time period definitions). The data are derived from the PBO solution in the North American reference frame and have been corrected for seasonal terms with the NLDAS hydrological model.

tions with ETS corrections and NLDAS hydrological corrections (Mitchell, 2004; Puskas et al., 2017), but alternative inversions show the same coupling change patch (Figures 6.8-6.9). Additionally, small patches of coupling change exist updip from the main spot to fit observed velocity changes at coastal stations. A plate velocity increase of 25 mm/yr in the dominant coupling change patch, or approximately 70% of the plate convergence rate, is required to fit velocity change in 2014. In 2016, the required plate interface slip rate decrease is about 15 mm/yr in the same area.

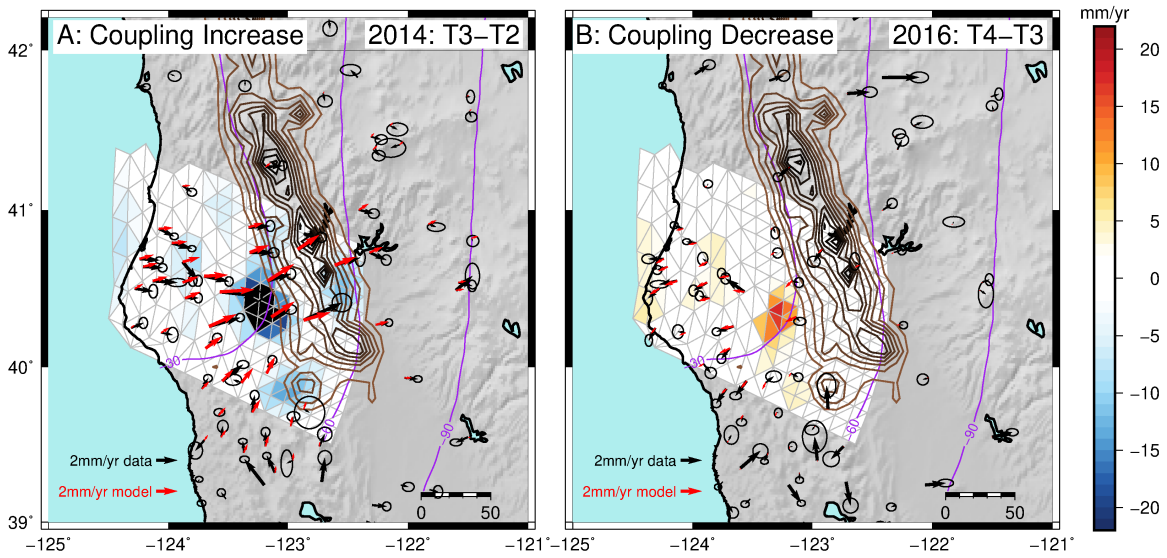

Figure 6.7: Inversion results for the PBO GPS velocity changes in 2014 and 2016, using a correction for ETS events, the NLDAS model to correct for seasonal variation in the time series, and elastic Green's functions computed for a heterogeneous elastic earth structure. The brown contours represent tremor density from the modified PNSN catalog, and the purple lines show the depth contours of the interface geometry. The most prominent feature is a localized coupling change on the interface around 40.3°N in both inversions.

6.5 Alternative Explanations for Observed Velocity Changes

We consider five hypotheses regarding the coherent GPS velocity changes following the 2014 and 2016 earthquakes: coseismic static stress changes on the CSZ, postseismic afterslip or viscoelastic relaxation, reference frame instability, multiannual hydrological loading, and coupling changes on the megathrust.

We reject explanations involving static stress changes because of the amplitude of the stresses. Coulomb stress changes from a single-dislocation model of the 2014 event are only ∼0.2 kPa, although in the right direction to produce increased coupling on the interface

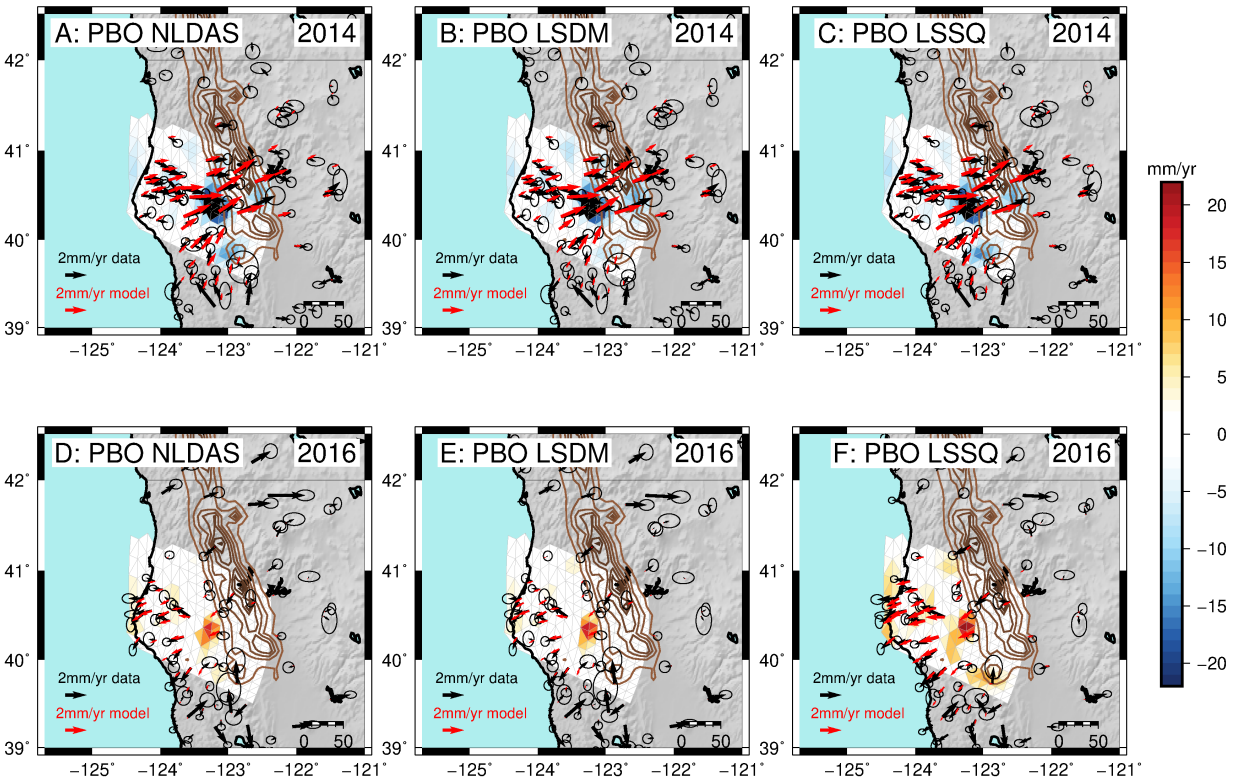

Figure 6.8: Inversion results for 2014 and 2016 time periods with a variety of seasonal correction techniques. All inversions have ETS corrections applied. Panels A and D are the same as Figure 6.7.

(Figure 6.10). For the 2016 event, the predicted coseismic Coulomb stress changes are less than 10 Pa and in the wrong direction. In addition, Coulomb stress changes are larger closer to the earthquakes in regions that did not experience coupling changes.

We also reject a hypothesis involving viscoelastic relaxation or afterslip following the offshore earthquakes because it cannot explain the largest displacements occurring inland from the coast rather than close to the earthquakes. Deep afterslip is similarly unable to explain the spatial gradients of the 2014 observations and the directions of the 2016 observations (Figure 6.11). These hypotheses also do not explain the apparent steady velocities after the 2014 and 2016 earthquakes.

Reference frame instability (Tian and Shen, 2016) may play a small role in generating large-scale motions in the GPS network. Our comparisons of different processing centers and reference frames show that the velocity changes affecting stations at the MTJ are evident in all the solutions we considered (Figure 6.12). Because we are computing velocity changes

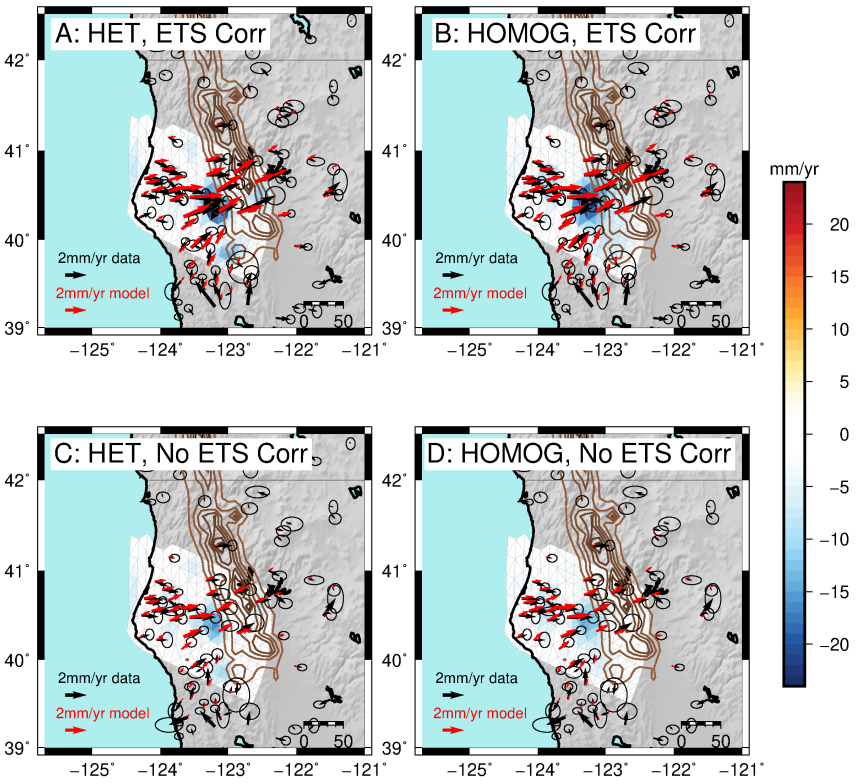

Figure 6.9: Testing the 2014 inversions for the effects of ETS corrections and homogeneous Greens functions vs. heterogeneous Green's functions. The ETS corrections affect the magnitude of the inverted velocity change, and the Green's functions affect the smoothness of the inverted velocity change.

from one period to the next, we would expect the results to be independent of reference frame if all frames are stable in time. However, some differences between solutions and reference frames do exist, most notably between the UNR NA12 and UNR ITRF solutions in central and southern California. Despite these differences, we find that all solutions have similar velocity changes at the MTJ. We also consider reference frame instability to be unlikely given the stability of nearby stations in Oregon (Figure 6.6).

Large-scale multiannual hydrology must be carefully considered in light of California's drought from 2011-2015. There appear to be other coherent velocity changes in central California that resemble the velocity changes at the MTJ, displaying eastward motion after 2014 and westward motion after 2016 (Figure 6.6). The directions of these changes are consistent with a hydrological explanation, moving faster towards the Sierra Nevadas during the post-2014 period when the drought was entering its recovery phase (Zou et al., 2018).

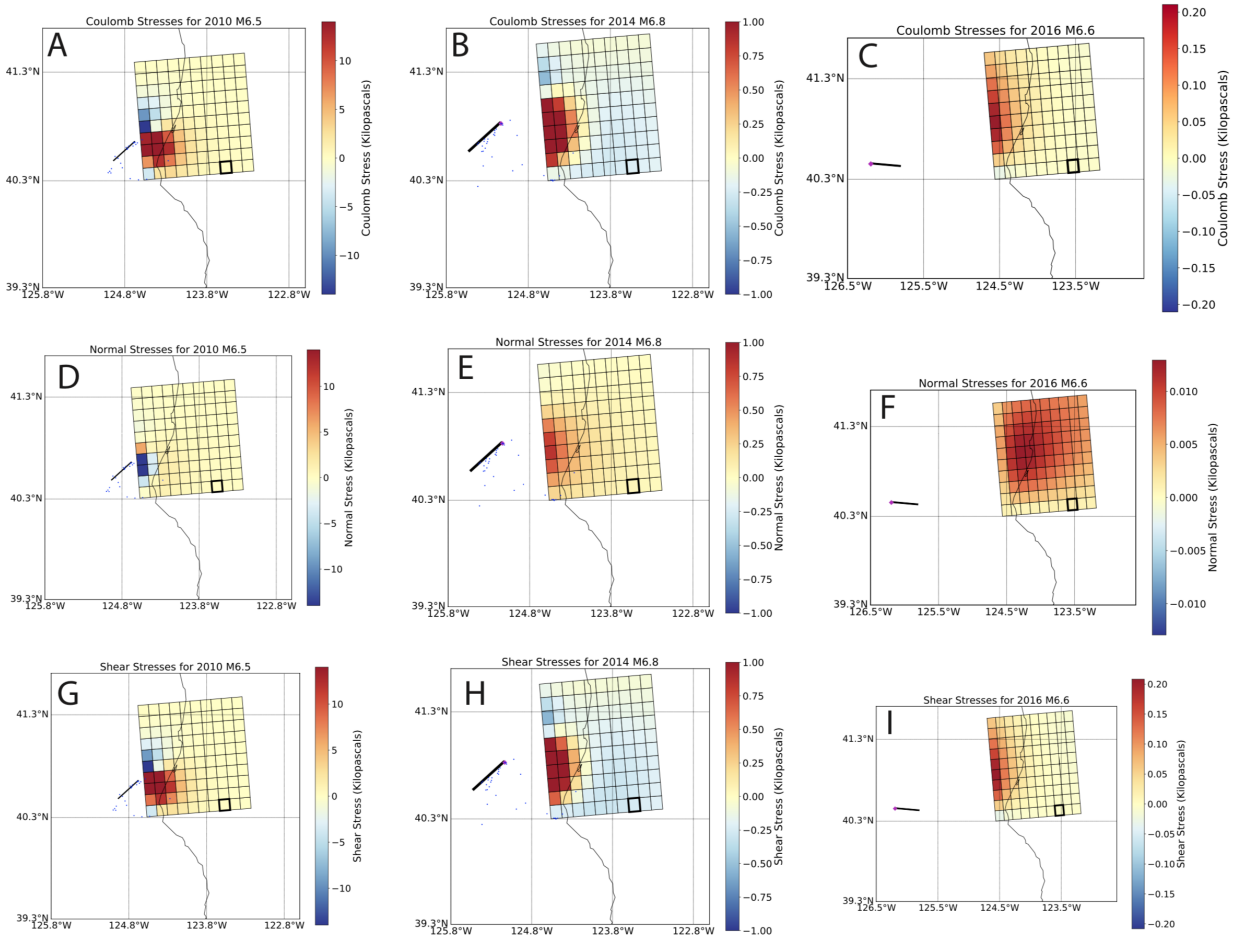

Figure 6.10: Plots of Coulomb, normal, and shear stress changes calculated from the estimated slip patches of the 2010, 2014, and 2016 earthquakes at the MTJ. Red is encouraging slip. The Coulomb stress changes at the grid cell closest to the coupling change patch (outlined box) are 0.1 kPa, -0.2 kPa, and -0.004 kPa for the 2010, 2014, and 2016 earthquakes, respectively.

GPS data in Oregon shows little to no variation through any of the time intervals in the study, even though some of the drought and hydrological loading signal would be expected there (Figure 6.6).

At the MTJ, our forward-modeled loading calculations with GRACE, GLDAS, NLDAS, and LSDM suggest that the observed velocity changes are larger than would be expected from large-scale hydrological loading. We find that the predicted horizontal rate changes due to these hydrological models are generally in the same direction as the observed velocity changes but are only 10-50% of the amplitude in Mendocino and extend over a much wider region from central California across Oregon (Figure 6.6). Predictions from GRACE differ

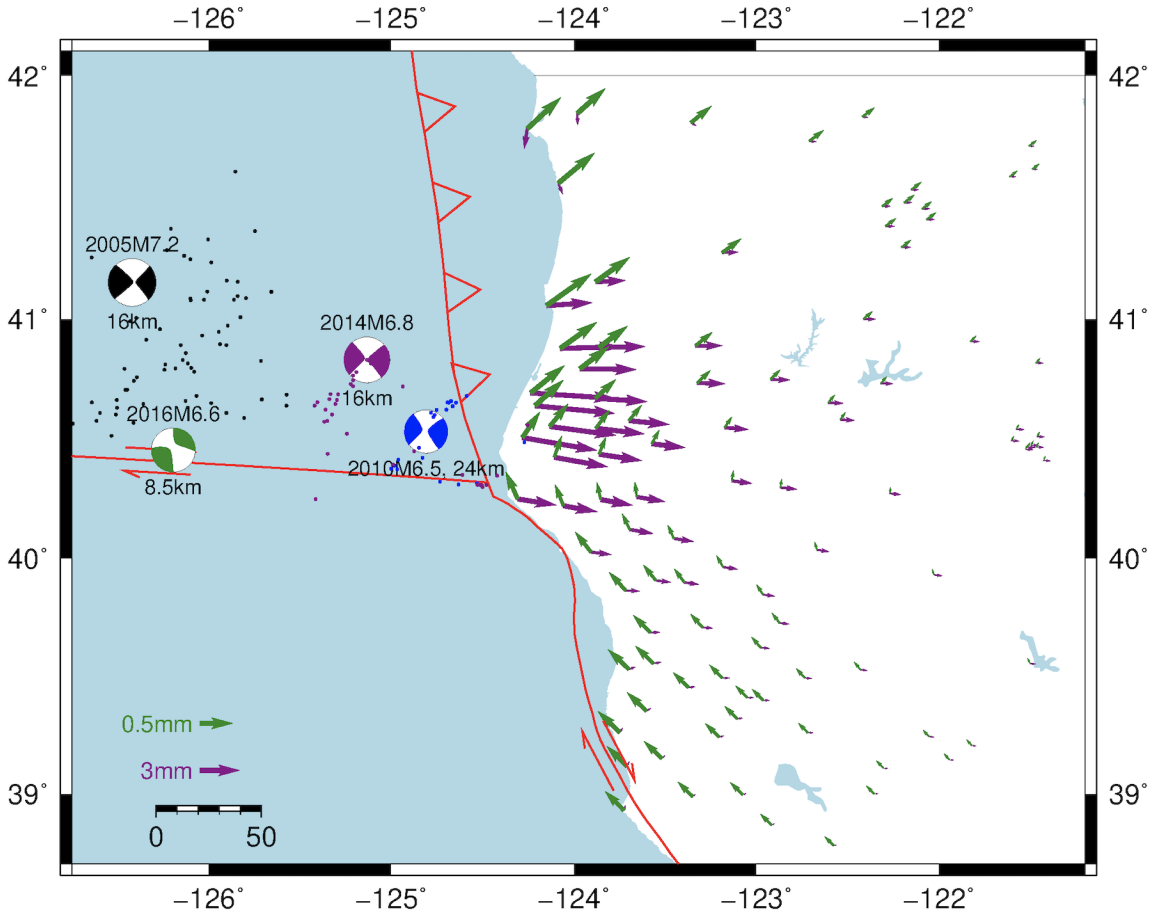

Figure 6.11: Simple afterslip models for the 2014 and 2016 earthquakes consisting of uniform slip patches in an elastic half-space. The modeled afterslip has the same geometry and rake as the coseismic rupture but is located 10km deeper than the coseismic rupture and is 50% of the coseismic moment. The 2014 afterslip-driven displacements (purple) show a marked decrease from the coast that is not observed in the data. The 2016 displacements (green, note different scale) do not match the data in either direction or magnitude.

from the other models in their orientations and very low amplitudes, which we think reflects the low spatial resolution of the GRACE-derived load distribution.

We also believe that large-scale processes like hydrological loading are unable to fully explain the MTJ signal because the velocity changes in the rest of California are different from the MTJ velocity changes in several important ways. First, unlike the data at the MTJ, the magnitudes and directions of the velocity changes are not consistent between the GPS solutions from different processing centers and reference frames. The central California effects seem to be larger in the CWU solution compared to the NMT solution, and they

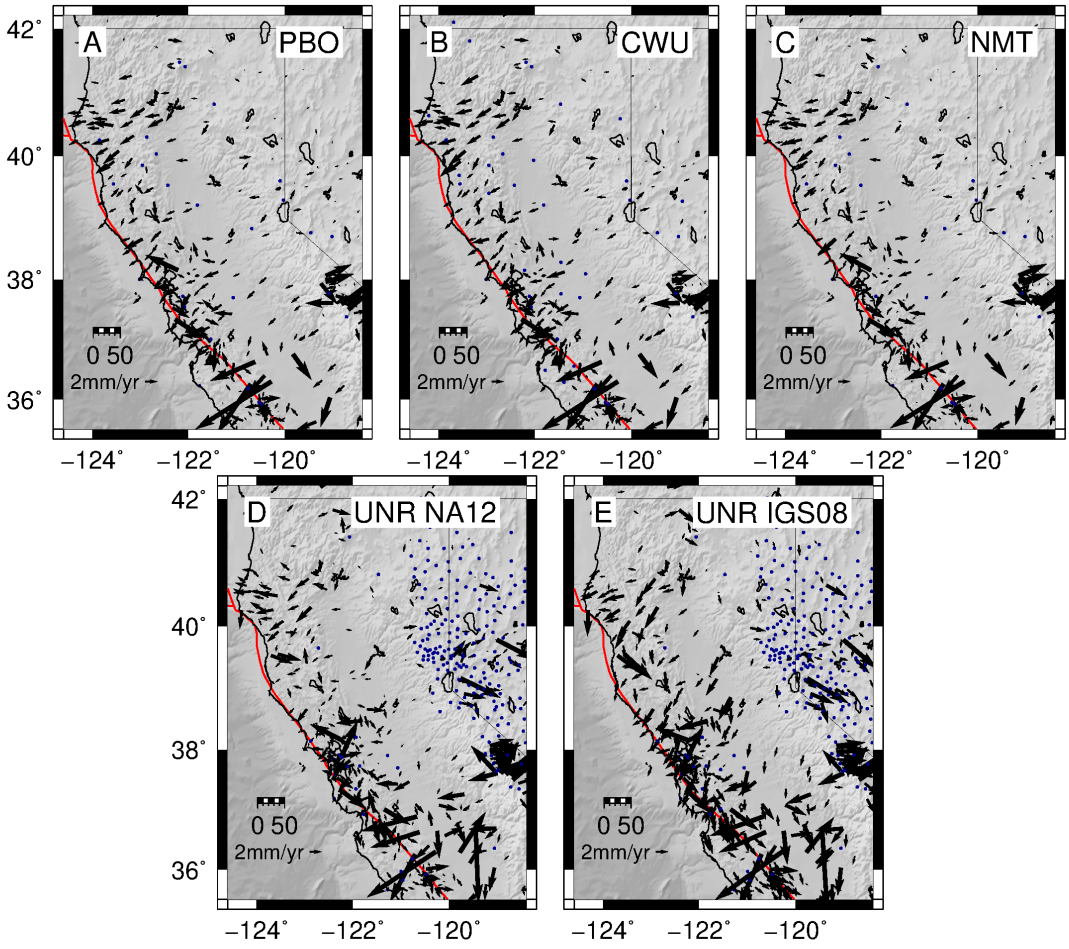

Figure 6.12: 2016 velocity changes (T4 minus T3) for all GPS processing centers. The data are in the North American reference frame unless otherwise noted. The velocity differences have unexplained signals in Central CA, but these signals vary in magnitude and azimuth depending on the processing center and reference frame. In particular, the signal seen around 2016 is west-oriented in central California in the PBO solutions and south-oriented in the UNR solutions.

seem to rotate progressively towards the south in the UNR ITRF solution (Figure 6.12). On the other hand, the velocity solutions are relatively consistent in their velocity changes at the MTJ. Second, the timing of the velocity changes in central California is less coherent compared to the timing of the velocity changes at the MTJ (Figure 6.4), suggesting that they have different causes. Although reference frame instability and regional hydrology are still possibilities for generating the signals in central California, it remains challenging to definitively attribute the signals to one of these mechanisms.

Beyond elastic loading, the poroelastic effects of aquifer recharge during drought recovery could produce horizontal motions near the edge of groundwater basins (Bawden et al., 2001), but could not produce changes on the scales observed in Mendocino. Poroelastic deformation may however be responsible for some of the rate changes we see at stations near large sedimentary basins in central California.

We determine that the above mechanisms are unable to produce the signals observed in Mendocino. In light of the closely coincident timing of the velocity changes and the nearby M6.5-M7.2 mainshocks, we consider changes in coupling on the interface between the subducting Gorda plate and the forearc blocks to be the most likely explanation for the observations at the MTJ. This hypothesis implies that plate interface coupling increased during the period from March 2014 to December 2016, and then decreased after December 2016.

6.6 Discussion

The location of inferred coupling changes is updip of the ETS zone (Wech, 2010; Wech and Creager, 2011; Michel et al., 2018) and downdip of the locked plate interface of the Cascadia megathrust (Wang and Tréhu, 2016)(Figure 6.7). Little is known about this region in Cascadia, or the so-called "gap" (Hyndman, 2013). Interseismic coupling models show low average coupling in this region ranging from 0-30% (Schmalzle et al., 2014). In other warm-slab subduction zones such as Nankai, this region hosts long-term SSEs that are distinct from the deeper and shorter-duration ETS events (Obara and Kato, 2016), and may involve either frictional or viscous deformation mechanisms (Gao and Wang, 2017). In Cascadia, such long-term SSE phenomena have been hypothesized (Wech and Creager, 2011) but are yet undocumented. The coupling changes documented here may reflect a similar long-term variation in slip behavior of the gap, although unlike a traditional SSE there is no observable temporal evolution to our identified signals. While we do not estimate absolute slip velocity on the plate interface, estimated velocity changes are below the plate rate, suggesting a coupling change rather than a slow slip event.

In light of the temporal association with nearby earthquakes, we suspect that the coupling changes somehow respond to dynamic stress perturbations. Seismic data show that the 2014 and 2016 earthquakes had similar shaking amplitudes and presumably similar dynamic stresses in the region of the coupling change in the long-period bands thought to be important for earthquake triggering (Brodsky and Prejean, 2005) (Figure 6.13). The 2016 event created

especially large Love waves for its magnitude, perhaps allowing it to influence coupling at such large distances (Figure 6.13). Unfortunately, using only surface measurements, it is extremely difficult to quantify the dynamic stresses applied to the interface at depth. This is especially true given our inability to estimate any waveguide effects of a finite width shear or damage zone at the interface.

One possible mechanism for dynamically triggered coupling changes is to alter the physical properties of the interface itself, such as the frictional contact area or rate-and-state friction parameters, through dynamic shaking. Experimentally, dynamic shaking has been observed to change frictional contacts in granular materials and fault gouge (Johnson, Savage, et al., 2008). Observational studies suggest that dynamic triggering of earthquakes or tremor is most likely when low-frequency surface waves interact with faults at very low effective normal stresses (Brodsky and Prejean, 2005; Miyazawa et al., 2008). However, these experiments typically move the faults closer to failure through dynamic shaking rather than providing mechanisms for both coupling increases and decreases under similar levels of shaking.

We instead propose an explanation involving pore fluid pressure exchange between the ETS zone and the coupling change zone just updip. ETS zones worldwide are thought to host nearly-lithostatic pore fluid pressures and thus low effective normal stresses (Shelly et al., 2007; Matsubara et al., 2009). These areas may undergo cyclic pressure changes during ETS cycles (Nakajima and Uchida, 2018; Warren-Smith et al., 2019). A low-permeability seal above the ETS zone may control the recurrence interval of ETS and the diffusion of fluids away from the overpressured ETS zone (Audet and Bürgmann, 2014). If this seal is fractured during dynamic shaking, or old fractures are reactivated, fracture permeability may temporarily increase, allowing pressure driven flow across the boundary and rapid pressure equalization with a high pore-fluid pressure zone located updip of the seal. Depending on the timing of the shaking with respect to the most recent ETS events, and the relative pressure in the updip zone, the unsealing could result in pressure diffusing into or out of the ETS zone, allowing for coupling in the updip region to increase or decrease (Figure 6.14). A similar model of permanent pressure changes through fracturing of low-permeability seals has been proposed for groundwater wells in Oregon following teleseismic shaking (Brodsky, Roeloffs, et al., 2003). This hypothesis requires that fluids are additionally confined by a seal mechanism updip from the ETS zone, creating a high pore pressure region corresponding to the coupling change "spot". This explains why coupling changes are observed only in this spot and not elsewhere along the interface. Speculatively, the coupling change zone's location may be controlled by the plate interface geometry, which shows a distinct "bump" in this region as indicated by the bend in the 30 km contour in Figure 6.7.

We hypothesize that coupling increased updip of the ETS zone after the 2014 earthquake because the dynamic shaking occurred shortly after an ETS event (Figure 6.14), when the pore pressure in the ETS zone was lowest. If the pressure seal was fractured during shaking, fluids could move into the ETS zone from the updip high-pressure reservoir, increasing coupling in the updip region. The 2016 event occurred 3 months after a major ETS event to the north, but that ETS event did not produce much tremor in the MTJ region. It is

therefore possible that pressures were still increasing in the ETS zone downdip of the observed coupling change, where the previous large ETS occurred ∼12 months before. Fracturing the seal in 2016 could have allowed fluids to diffuse in the opposite direction, decreasing coupling updip (Figure 6.14). Similar to the 2016 earthquake, the 2010 earthquake occurred late in an ETS cycle and produced velocity changes, although smaller and more difficult to resolve, in the same direction as the 2016 case (Figure 6.6). Although we propose a mechanism that invokes fluid flow in the fault zone, any mechanism producing increases and decreases of effective normal stress updip of the ETS zone (such as fluid exchange with the subducted slab or overriding crust) could also contribute to the velocity change phenomena.

Coupling changes similar to the MTJ have been observed in subduction zones in other parts of the world, but they appear to be rare. The closest analogue to the Mendocino case was observed south of the Iquique earthquake in Chile, where interface coupling appeared to increase after the earthquake on a distant enough part of the plate interface to preclude static triggering (Hoffmann et al., 2018). Two decreases in megathrust coupling have been observed in Chile and are potentially also associated with earthquakes (Jara et al., 2017; Klein et al., 2018). Elsewhere, a long-lived decrease in coupling was documented in Sumatra using campaign GPS following an earthquake in 2000 (Prawirodirdjo et al., 2010). In south central Alaska, multiple coupling changes were observed during the past two decades associated with many-years-long SSEs (Li, Freymueller, et al., 2016). To our knowledge, the MTJ case represents the first example of dynamic stressing leading to both increases and decreases in coupling on the same fault region.

Interseismic coupling models are a key element in our understanding of subduction zone processes and associated hazards. However, coupling models typically consider coupling to be time-independent and not susceptible to dynamic strain transients. The time-dependent coupling changes inferred at the MTJ and elsewhere have significant implications for our understanding of subduction zones and should be the subject of further work in the future.

6.7 Conclusion

We observe changes in GPS velocities in northern California that depict a consistent increased eastward movement of several mm/yr after mid-2014 and a westward reversal after late 2016. We invert these observations to model coupling changes on the CSZ, and we find that interseismic coupling updip of the ETS zone increased by ∼70% (25 mm/yr) at the time of a M6.8 earthquake in 2014 and then decreased again by ∼40% following a M6.6 event in 2016. These observations suggest that at least in the southernmost CSZ, megathrust coupling is a time-dependent quantity on years-long timescales in addition to the short timescales of ETS events. We infer that both coupling increases and decreases can result from dynamic stressing by nearby large earthquakes, which we propose to reflect variable pressure gradients in the fault zone at the time of the triggering events. Subduction zone coupling models, which are critical for estimating the hazards posed by megathrust earthquakes, are usually made under the assumption that interseismic coupling is time-independent. Our findings suggest

that this assumption may not hold in all regions or time periods even outside of the ETS zone. This finding has direct implications for our understanding of earthquakes in Cascadia and elsewhere.

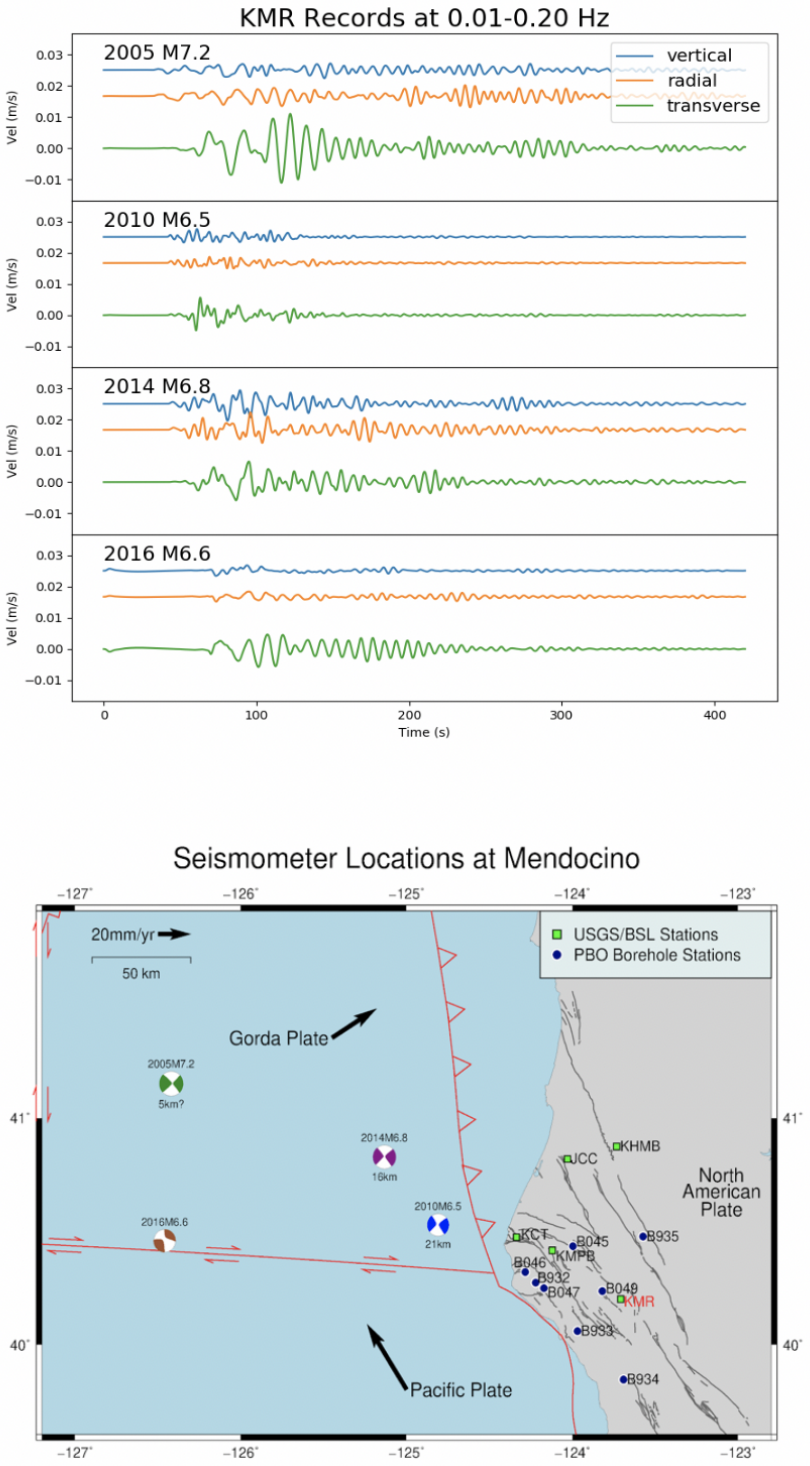

Figure 6.13: Filtered velocity waveforms (0.01-0.2 Hz bandpass) for the 4 earthquakes in Figure 6.1 at station KMR (red label), located near the node (or Love wave maximum) of the focal mechanism for each earthquake. All four waveforms are on the same scale.

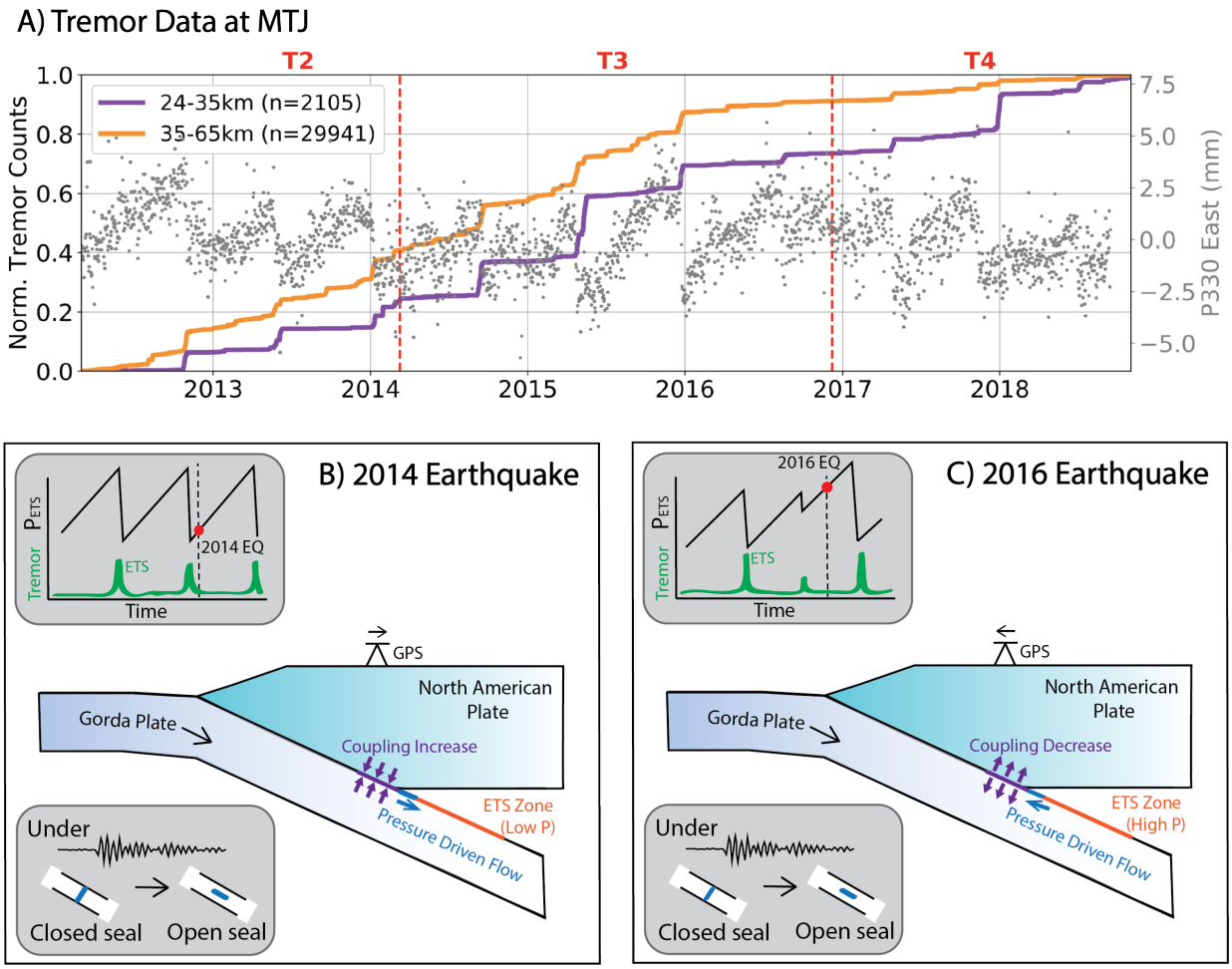

Figure 6.14: a) Tremor as a function of time in the MTJ, focusing on the region between 40°N and 41°N in the reprocessed tremor catalog. The detrended and seasonal-removed east component time series for station P330, located above the tremor zone at 40.3°N (blue arrow in Figure 6.1b), is plotted with gray dots. b and c) Cartoon schematic showing pressure conditions on the interface at the time of the 2014 and 2016 earthquakes.

Chapter 7

Conclusions

As I write this, nearly at the end of my PhD program at Berkeley, the city of Ridgecrest, California is recovering from a pair of recent large earthquakes that produced strong shaking and destroyed a number of buildings through fire or structural damage. Earth scientists are busily collecting and distributing data. Some of the most important datasets being provided are geodetic in nature; products such as GPS displacements, InSAR interferograms, and pixel offset maps are being distributed on short timescales to emergency responders and the general public. These developments underscore the growing usefulness of space geodetic measurements to both science and society.

These developments also remind us that understanding the mechanical behavior of the earth's crust is of utmost importance for a variety of applications including earthquake hazards. When faults slip, either at seismic speeds or at slow speeds through aseismic slip, or when the earth deforms in response to interseismic stress or mass loading, we have opportunities to learn about the energy stored in the crust that is the ultimate driver of earthquakes. Space geodesy provides useful tools to investigate the processes that store and release energy in the crust. However, studies attempting to resolve crustal deformation processes with geodetic data alone are often missing key information that could be gained from other sources.

In the chapters presented in this dissertation, I focused on a number of earth deformation problems related to tectonics and the earthquake cycle, in each case using geodetic tools as one piece of a larger scientific puzzle. I found that fault maturity on the San Andreas does not correlate with the presence of geodetically inferred compliant fault zones, but lithology does (Chapter 2). Using a case study of the Mendocino Fault Zone, I confirmed that an oceanic transform fault creeps aseismically at a large fraction of its slip rate (Chapter 3). In Chapter 4, I determined the rupture plane of the 2017 Botswana earthquake using InSAR and teleseismic data jointly when geodetic data alone was unable to distinguish between the planes. I showed that mass loading from hydrological sources produces deformation in Southeast Asia that can be well modeled by GRACE gravity models (Chapter 5). Lastly, I found that the seismic coupling on the southern Cascadia subduction zone shows unusual variations on years-long timescales that appear to be dynamically triggered (Chapter 6). In

each geodetic study, the inclusion of non-geodetic data resulted in insights beyond what was achievable with geodetic data alone.

In most cases, the research presented here answers a particular question but opens several more in the process. For example, is the aseismic slip on the Mendocino Fault Zone always constant with time, or can it respond to nearby earthquakes with transient slip perturbations? What are the physical processes initiating earthquakes at 30km deep in the cratonic lower crust of southern Africa, where earthquakes would not be expected? How can dynamic shaking from regional earthquakes change the frictional coupling properties of the megathrust in Southern Cascadia? Further research into fault zone behavior may shed light on these important questions, especially if the expertise of multiple scientific disciplines is leveraged in the effort.

New tools on the horizon, such as arrays of seismic networks, distributed acoustic sensing fiber optic cables, and laboratory studies under fault zone conditions, enrich the field of possibilities for answering some of these questions. From a geodesist's perspective, these tools provide important additional value to scientific investigations, whether incorporated as formal constraints, independent verification of outcomes, or guidance in model decision-making. A wide range of possibilities is open to scientific inquiry.

Space geodesy from GPS and InSAR is an increasingly precise and useful tool for improving our understanding of the behavior of faults during the earthquake cycle and the rheology of the earth. The role of geodesy in future science endeavors is potentially enormous, as underscored by the rapid push for geodetic information after new earthquakes such as the recent events in Ridgecrest, California. For geodesists as we investigate research questions and respond to natural disasters like earthquakes, it is important to remember that we always have a larger suite of tools at our disposal to understand the deformation of the earth.

Bibliography

Aagaard, B. T., M. G. Knepley, and C. A. Williams (2013). "A domain decomposition approach to implementing fault slip in finite-element models of quasi-static and dynamic crustal deformation". In: *Journal of Geophysical Research: Solid Earth* 118.6, pp. 3059–3079. ISSN: 21699356. DOI: 10.1002/jgrb.50217.

— (2017a). *PyLith User Manual, Version 2.2.1*. Tech. rep. Davis, CA: Computational Infrastructure of Geodynamics.

— (2017b). "PyLIth v2.2.1". In: *Computational Infrastructure of Geodynamics*. Davis, CA. DOI: 10.5281/zenodo.886600.

Abercrombie, R.E. and G. Ekström (2001). "Earthquake slip on oceanic transform faults". In: *Nature* 410.6824, pp. 74–7. ISSN: 0028-0836. DOI: 10.1038/35065064. URL: http://www.ncbi.nlm.nih.gov/pubmed/11242043.

Albano, Matteo, Marco Polcari, Christian Bignami, Marco Moro, Michele Saroli, and Salvatore Stramondo (2017). "Did Anthropogenic Activities Trigger the 3 April 2017 Mw6.5 Botswana Earthquake?" In: *Remote Sensing* 9.1028, pp. 1–12. DOI: 10.3390/rs9101028.

Anderson, Robert S. (1990). "Evolution of the Northern Santa Cruz Mountains by Advection of Crust Past a San Andreas Fault Bend". en. In: *Science* 249.4967, pp. 397–401. ISSN: 0036-8075, 1095-9203. DOI: 10.1126/science.249.4967.397. URL: http://science.sciencemag.org/content/249/4967/397 (visited on 04/20/2016).

Araki, Eiichiro, Demian M. Saffer, Achim J. Kopf, Laura M. Wallace, Toshinori Kimura, Yuya Machida, Satoshi Ide, and Earl Davis (2017). "Recurring and triggered slow-slip events near the trench at the Nankai Trough subduction megathrust". In: *Science* 356.6343, pp. 1157–1160. ISSN: 10959203. DOI: 10.1126/science.aan3120.

Argus, Donald F., Yuning Fu, and Felix W. Landerer (2014). "Seasonal variation in total water storage in California inferred from GPS observations of vertical land motion". In: *Geophysical Research Letters* 41, pp. 1971–1980. DOI: 10.1002/2014GL059570.

Argus, Donald F., Felix W. Landerer, et al. (2017). "Sustained Water Loss in California's Mountain Ranges During Severe Drought From 2012 to 2015 Inferred From GPS". In: *Journal of Geophysical Research: Solid Earth* 122.12, pp. 10, 559–10, 585. ISSN: 21699356. DOI: 10.1002/2017JB014424.

Arvidsson, Ronald, Rutger Wahlstrom, and Ota Kulhanek (1992). "Deep-crustal earthquakes in the southern Baltic Shield". In: *Geophysical Journal International* 108, pp. 767–777.

Audet, Pascal and Roland Bürgmann (2011). "Dominant role of tectonic inheritance in supercontinent cycles". In: *Nature Geoscience* 4.3, pp. 184–187. ISSN: 1752-0894. DOI: 10.1038/ngeo1080. URL: http://www.nature.com/doifinder/10.1038/ngeo1080.

— (2014). "Possible control of subduction zone slow-earthquake periodicity by silica enrichment". In: *Nature* 510.7505, pp. 389–392. ISSN: 14764687. DOI: 10.1038/nature13391.

Avouac, Jean-Philippe (2015). "From Geodetic Imaging of Seismic and Aseismic Fault Slip to Dynamic Modeling of the Seismic Cycle". In: *Annual Review of Earth and Planetary Sciences* 43.1, p. 150223150959000. ISSN: 0084-6597. DOI: 10.1146/annurev-earth-060614-105302. URL: http://www.annualreviews.org/doi/abs/10.1146/annurev-earth-060614-105302.

Ballard, S, H N Pollack, and N J Skinner (1987). "Terrestrial Heat-Flow in Botswana and Namibia". In: *Journal of Geophysical Research* 92.B7, pp. 6291–6300. DOI: 10.1029/JB092iB07p06291.

Barbot, Sylvain, Yuri Fialko, and Dave Sandwell (2008). "Effect of a compliant fault zone on the inferred earthquake slip distribution". en. In: *Journal of Geophysical Research: Solid Earth* 113.B6, B06404. ISSN: 2156-2202. DOI: 10.1029/2007JB005256. URL: http://onlinelibrary.wiley.com/doi/10.1029/2007JB005256/abstract (visited on 04/05/2016).

Bartlow, Noel M., Shin'Ichi Miyazaki, Andrew M. Bradley, and Paul Segall (2011). "Space-time correlation of slip and tremor during the 2009 Cascadia slow slip event". In: *Geophysical Research Letters* 38.18, pp. 1–6. ISSN: 00948276. DOI: 10.1029/2011GL048714.

Bawden, Gerald W., Wayne Thatcher, Ross S. Stein, Ken W. Hudnut, and Gilles Peltzer (2001). "Tectonic contraction across Los Angeles after removal of groundwater pumping effects". In: *Nature* 412.6849, pp. 812–815. ISSN: 00280836. DOI: 10.1038/35090558.

Bayes, Thomas (1763). "An Essay towards Solving a Problem in the Doctrine of Chances". In: *Philosophical Transaction* 53, pp. 370–418.

Becker, Janet M. and Michael Bevis (2004). "Love's problem". In: *Geophysical Journal International* 156.2, pp. 171–178. ISSN: 0956540X. DOI: 10.1111/j.1365-246X.2003.02150.x.

Begg, G C, L M Natapov, Suzanne Y O Reilly, C J O Neill, and P Bowden (2009). "The lithospheric architecture of Africa : Seismic tomography , mantle petrology , and tectonic evolution". In: *Geosphere* 5.1, pp. 23–50. DOI: 10.1130/GES00179.1.

Ben-Zion, Yehuda et al. (2015). "Basic data features and results from a spatially dense seismic array on the San Jacinto fault zone". en. In: *Geophysical Journal International* 202.1, pp. 370–380. ISSN: 0956-540X, 1365-246X. DOI: 10.1093/gji/ggv142. URL: http://gji.oxfordjournals.org/content/202/1/370 (visited on 04/23/2016).

Bird, Peter (2003). "An updated digital model of plate boundaries". In: *Geochemistry, Geophysics, Geosystems* 4.3. ISSN: 15252027. DOI: 10.1029/2001GC000252.

Bird, Peter, Zvi Ben-avraham, Gerald Schubert, Marco Andreoli, and Giulio Viola (2006). "Patterns of stress and strain rate in southern Africa". In: *Journal of Geophysical Research* 111.February, pp. 1–14. DOI: 10.1029/2005JB003882.

Blake, M. C. and David L. Jones (1974). "Origin of Franciscan Melanges in Northern California". In: *Society of Economic Paleontologists and Mineralogists* SEPM Special Publication No. 19.Modern And Ancient Geosynclinal Sedimentation, pp. 345–357.

Blewitt, Geoffrey, William C. Hammond, and Corné Kreemer (2018). "Harnessing the GPS data explosion for interdisciplinary science". In: *EOS* 99. DOI: https://doi.org/10.1029/2018EO104623.

Boettcher, M. S. and T. H. Jordan (2004). "Earthquake scaling relations for mid-ocean ridge transform faults". In: *Journal of Geophysical Research B: Solid Earth* 109.12, pp. 1–21. ISSN: 01480227. DOI: 10.1029/2004JB003110.

Boyarko, Devin C and Michael R Brudzinski (2010). "Spatial and temporal patterns of nonvolcanic tremor along the southern Cascadia subduction zone". In: *Journal of Geophysical Research: Solid Earth* 115.October 2009, pp. 1–16. DOI: 10.1029/2008JB006064.

Brocher, Thomas M. (2005). *Compressional and Shear Wave Velocity Versus Depth in the San Francisco Bay Area, California: Rules for USGS Bay Area Velocity Model 05.0.0.* URL: http://pubs.usgs.gov/of/2005/1317/of2005-1317.pdf.

Brodsky, Emily E. and Stephanie G. Prejean (2005). "New constraints on mechanisms of remotely triggered seismicity at Long Valley Caldera". In: *Journal of Geophysical Research: Solid Earth* 110.4, pp. 1–14. ISSN: 21699356. DOI: 10.1029/2004JB003211.

Brodsky, Emily E., Evelyn Roeloffs, Douglas Woodcock, Ivan Gall, and Michael Manga (2003). "A mechanism for sustained groundwater pressure changes induced by distant earthquakes". In: *Journal of Geophysical Research* 108.B8, pp. 1–10. ISSN: 0148-0227. DOI: 10.1029/2002jb002321.

Brudzinski, Michael R. and Richard M. Allen (2007). "Segmentation in episodic tremor and slip all along Cascadia". In: *Geology* 35.10, pp. 907–910. ISSN: 00917613. DOI: 10.1130/G23740A.1.

Bufford, Kelsey Mosley, Estella A. Atekwana, Mohamed G. Abdelsalam, Elijah Shemang, Eliot A. Atekwana, Kevin Mickus, Moikwathai Moidaki, Motsoptse P. Modisi, and Loago Molwalefhe (2012). "Geometry and faults tectonic activity of the Okavango Rift Zone, Botswana: Evidence from magnetotelluric and electrical resistivity tomography imaging". In: *Journal of African Earth Sciences* 65, pp. 61–71. ISSN: 1464343X. DOI: 10.1016/j.jafrearsci.2012.01.004.

Bürgmann, Roland (2018). "The geophysics, geology and mechanics of slow fault slip". In: *Earth and Planetary Science Letters* 495, pp. 112–134. ISSN: 0012821X. DOI: 10.1016/j.epsl.2018.04.062. URL: https://doi.org/10.1016/j.epsl.2018.04.062.

Bürgmann, Roland, Ramfffdfffdn Arrowsmith, Trevor Dumitru, and Robert McLaughlin (1994). "Rise and fall of the southern Santa Cruz Mountains, California, from fission tracks, geomorphology, and geodesy". en. In: *Journal of Geophysical Research: Solid Earth* 99.B10, pp. 20181–20202. ISSN: 2156-2202. DOI: 10.1029/94JB00131. URL: http://onlinelibrary.wiley.com/doi/10.1029/94JB00131/abstract (visited on 04/20/2016).

Bürgmann, Roland and David Chadwell (2014). "Seafloor Geodesy". In: *Annual Review of Earth and Planetary Sciences* 42.1, pp. 509–534. ISSN: 0084-6597. DOI: 10.1146/

annurev-earth-060313-054953. URL: http://dx.doi.org/10.1146/annurev-earth-060313-054953.

Calais, E., T. Camelbeeck, S. Stein, M. Liu, and T. J. Craig (2016). "A new paradigm for large earthquakes in stable continental plate interiors". In: *Geophysical Research Letters* 43.20, pp. 10, 621–10, 637. ISSN: 19448007. DOI: 10.1002/2016GL070815.

Calais, E., A. M. Freed, R. Van Arsdale, and S. Stein (2010). "Triggering of New Madrid seismicity by late-Pleistocene erosion". In: *Nature* 466.7306, pp. 608–611. ISSN: 0028-0836. DOI: 10.1038/nature09258. URL: http://www.nature.com/doifinder/10.1038/nature09258.

Cattania, Camilla, Jeffrey J. McGuire, and John A. Collins (2017). "Dynamic Triggering and Earthquake Swarms on East Pacific Rise Transform Faults". In: *Geophysical Research Letters* 44, pp. 702–710. ISSN: 00948276. DOI: 10.1002/2016GL070857. URL: http://doi.wiley.com/10.1002/2016GL070857.

Chanard, Kristel, Luce Fleitout, Eric Calais, Sylvain Barbot, and Jean Philippe Avouac (2018). "Constraints on Transient Viscoelastic Rheology of the Asthenosphere From Seasonal Deformation". In: *Geophysical Research Letters* 45.5, pp. 2328–2338. ISSN: 19448007. DOI: 10.1002/2017GL076451.

Chanard, Kristel, Luce Fleitout, Eric Calais, Paul Rebischung, and Jean Philippe Avouac (2018). "Toward a Global Horizontal and Vertical Elastic Load Deformation Model Derived from GRACE and GNSS Station Position Time Series". In: *Journal of Geophysical Research: Solid Earth* 123.4, pp. 3225–3237. ISSN: 21699356. DOI: 10.1002/2017JB015245.

Chaussard, E., R. Bfffdfffdrgmann, H. Fattahi, C. W. Johnson, R. Nadeau, T. Taira, and I. Johanson (2015). "Interseismic coupling and refined earthquake potential on the Hayward-Calaveras fault zone". en. In: *Journal of Geophysical Research: Solid Earth* 120.12, 2015JB012230. ISSN: 2169-9356. DOI: 10.1002/2015JB012230. URL: http://onlinelibrary.wiley.com/doi/10.1002/2015JB012230/abstract (visited on 04/18/2016).

Chaussard, Estelle, Roland Bürgmann, Manoochehr Shirzaei, Eric J. Fielding, and B. Baker (2015). "Predictability of hydraulic head changes and characterization of aquifer-system and fault properties from InSAR-derived ground deformation". In: *Journal of Geophysical Research : Solid Earth* 119, pp. 6572–6590. DOI: 10.1002/2014JB11266.

Chaytor, Jason D., Chris Goldfinger, Robert P. Dziak, and Christopher G. Fox (2004). "Active deformation of the Gorda plate: Constraining deformation models with new geophysical data". In: *Geology* 32.4, pp. 353–356. ISSN: 00917613. DOI: 10.1130/G20178.2.

Chen, Curtis W. and Howard A. Zebker (2000). "Network approaches to two-dimensional phase unwrapping: intractability and two new algorithms: erratum". In: *Journal of the Optical Society of America A* 17.3, pp. 401–414. URL: https://www.osapublishing.org/abstract.cfm?URI=josaa-18-5-1192.

Chen, Kate Huihsuan, Robert M. Nadeau, and Ruey Juin Rau (2007). "Towards a universal rule on the recurrence interval scaling of repeating earthquakes?" In: *Geophysical Research Letters* 34.16, pp. 1–5. ISSN: 00948276. DOI: 10.1029/2007GL030554.

Chen, Kate Huihusan, Roland Bürgmann, and Robert M. Nadeau (2013). "Do earthquakes talk to each other? Triggering and interaction of repeating sequences at Parkfield". In: *Journal of Geophysical Research: Solid Earth* 118.1, pp. 165–182. ISSN: 21699356. DOI: 10.1029/2012JB009486.

Chen, Qizhi and Jeffrey T. Freymueller (2002). "Geodetic Evidence for a Near-Fault Compliant Zone along the San Andreas Fault in the San Francisco Bay Area". en. In: *Bulletin of the Seismological Society of America* 92.2, pp. 656–671. ISSN: 0037-1106, 1943-3573. DOI: 10.1785/0120010110. URL: http://bssa.geoscienceworld.org/content/92/2/656 (visited on 04/05/2016).

Chen, Wang-ping and Peter Molnar (1983). "Focal depths of intracontinental and intraplate earthquakes and their implications for the thermal and mechanical properties of the lithosphere". In: *Journal of Geophysical Research* 88.B5, pp. 4183–4214.

Chen, Xiaowei and Jeffrey J McGuire (2016). "Measuring earthquake source parameters in the Mendocino triple junction region using a dense OBS array : Implications for fault strength variations". In: *Earth and Planetary Science Letters* 453, pp. 276–287. ISSN: 0012-821X. DOI: 10.1016/j.epsl.2016.08.022. URL: http://dx.doi.org/10.1016/j.epsl.2016.08.022.

Clark, Dan (2004). *Seismicity along the northern foreland of the Albany-Fraser Orogen*. Tech. rep.

Cleveland, Robert B., William S. Cleveland, Jean E. McRae, and Irma Terpenning (1990). "STL: A Seasonal-Trend Decomposition Procedure Based on Loess". In: *Journal of Official Statistics* 6.1, pp. 3–73. ISSN: 0282-423X. DOI: citeulike-article-id:1435502.

Cochran, Elizabeth S., Yong-Gang Li, Peter M. Shearer, Sylvain Barbot, Yuri Fialko, and John E. Vidale (2009). "Seismic and geodetic evidence for extensive, long-lived fault damage zones". en. In: *Geology* 37.4, pp. 315–318. ISSN: 0091-7613, 1943-2682. DOI: 10.1130/G25306A.1. URL: http://geology.gsapubs.org/content/37/4/315 (visited on 04/05/2016).

Copley, Alex, James Hollingsworth, and Eric Bergman (2012). "Constraints on fault and lithosphere rheology from the coseismic slip and postseismic afterslip of the 2006 M¡inf¿w¡/inf¿7.0 Mozambique earthquake". In: *Journal of Geophysical Research: Solid Earth* 117.3, pp. 1–16. ISSN: 21699356. DOI: 10.1029/2011JB008580.

Craig, T. J., J. A. Jackson, K. Priestley, and D. Mckenzie (2011). "Earthquake distribution patterns in Africa: Their relationship to variations in lithospheric and geological structure, and their rheological implications". In: *Geophysical Journal International* 185.1, pp. 403–434. ISSN: 0956540X. DOI: 10.1111/j.1365-246X.2011.04950.x.

d'Alessio, M. A., I. A. Johanson, R. Bfffdfffdrgmann, D. A. Schmidt, and M. H. Murray (2005). "Slicing up the San Francisco Bay Area: Block kinematics and fault slip rates from GPS-derived surface velocities". en. In: *Journal of Geophysical Research: Solid Earth* 110.B6, B06403. ISSN: 2156-2202. DOI: 10.1029/2004JB003496. URL: http://onlinelibrary.wiley.com/doi/10.1029/2004JB003496/abstract (visited on 04/05/2016).

DeMets, Charles, Richard G. Gordon, and Donald F. Argus (2010). "Geologically current plate motions". In: *Geophysical Journal International* 181.1, pp. 1–80. ISSN: 0956540X. DOI: 10.1111/j.1365-246X.2009.04491.x.

Dill, R. and H. Dobslaw (2013). "Numerical simulations of global-scale high-resolution hydrological crustal deformations". In: *Journal of Geophysical Research: Solid Earth* 118.9, pp. 5008–5017. ISSN: 21699356. DOI: 10.1002/jgrb.50353.

Dixon, Timothy H., Meghan Miller, Frederic Farina, Hongzhi Wang, and Daniel Johnson (2000). "Present-day motion of the Sierra Nevada block and some tectonic implications for the Basin and Range province, North American Cordillera". In: *Tectonics* 19.1, pp. 1–24. ISSN: 02787407. DOI: 10.1029/1998TC001088.

Dolan, J. F. and B. D. Haravitch (2014). "How well do surface slip measurements track slip at depth in large strike-slip earthquakes? The importance of fault structural maturity in controlling on-fault slip versus off-fault surface deformation". In: *Earth and Planetary Science Letters* 388, pp. 38–47.

Dominguez, Luis A., Taka'aki Taira, and Miguel A. Santoyo (2016). "Spatiotemporal variations of characteristic repeating earthquake sequences along the Middle America Trench in Mexico". In: *Journal of Geophysical Research: Solid Earth*, pp. 1–16. ISSN: 21699313. DOI: 10.1002/2016JB013242. URL: http://doi.wiley.com/10.1002/2016JB013242.

Dziewonski, A. M. and Don Anderson (1981). "Preliminary reference Earth model". In: *Physics of the Earth and Planetary Interiors* 25.4, pp. 297–356.

Ekström, G., M. Nettles, and A. M. Dziewoński (2012). "The global CMT project 2004-2010: Centroid-moment tensors for 13,017 earthquakes". In: *Physics of the Earth and Planetary Interiors* 200-201, pp. 1–9. ISSN: 00319201. DOI: 10.1016/j.pepi.2012.04.002.

England, Philip and James Jackson (2011). "Uncharted seismic risk". In: *Nature Geoscience* 4.6, pp. 348–349. ISSN: 1752-0894. DOI: 10.1038/ngeo1168. URL: http://dx.doi.org/10.1038/ngeo1168.

Farrell, W. E. (1972). "Deformation of the Earth by surface loads". In: *Reviews of Geophysics* 10.3, pp. 761–797.

Fialko, Yuri (2006). "Interseismic strain accumulation and the earthquake potential on the southern San Andreas fault system". en. In: *Nature* 441.7096, pp. 968–971. ISSN: 0028-0836. DOI: 10.1038/nature04797. URL: http://www.nature.com/nature/journal/v441/n7096/abs/nature04797.html (visited on 08/03/2016).

— (2004). "Probing the mechanical properties of seismically active crust with space geodesy: Study of the coseismic deformation due to the 1992 Mw7.3 Landers (southern California) earthquake". en. In: *Journal of Geophysical Research: Solid Earth* 109.B3, B03307. ISSN: 2156-2202. DOI: 10.1029/2003JB002756. URL: http://onlinelibrary.wiley.com/doi/10.1029/2003JB002756/abstract (visited on 04/05/2016).

Field, Edward H. et al. (2014). "Uniform California Earthquake Rupture Forecast, Version 3 (UCERF3)fffdfffdfffdThe Timefffdfffdfffd Independent Model". en. In: *Bulletin of the Seismological Society of America* 104.3, pp. 1122–1180. ISSN: 0037-1106, 1943-3573. DOI: 10.1785/0120130164. URL: http://www.bssaonline.org/content/104/3/1122 (visited on 04/06/2016).

Floyd, Michael A. et al. (2016). "Spatial variations in fault friction related to lithology from rupture and afterslip of the 2014 South Napa, California, earthquake". en. In: *Geophysical Research Letters* 43.13, 2016GL069428. ISSN: 1944-8007. DOI: 10.1002/2016GL069428. URL: http://onlinelibrary.wiley.com/doi/10.1002/2016GL069428/abstract (visited on 08/02/2016).

Frohlich, Cliff and Laura Reiser Wetzel (2007). "Comparison of seismic moment release rates along different types of plate boundaries". In: *Geophysical Journal International* 171.2, pp. 909–920. DOI: 10.1111/j.1365-246X.2007.03550.x.

Fu, Yuning, Donald F. Argus, and Felix W. Landerer (2015). "GPS as an independent measure to estimate terrestrial water storage variations in Washington and Oregon". In: *Journal of Geophysical Research: Solid Earth* 120, pp. 552–566. DOI: 10.1002/2014JB011415.

Fu, Yuning and Jeffrey T. Freymueller (2013). "Repeated large Slow Slip Events at the south-central Alaska subduction zone". In: *Earth and Planetary Science Letters* 375, pp. 303–311. ISSN: 0012821X. DOI: 10.1016/j.epsl.2013.05.049. URL: http://dx.doi.org/10.1016/j.epsl.2013.05.049.

— (2012). "Seasonal and long-term vertical deformation in the Nepal Himalaya constrained by GPS and GRACE measurements". In: *Journal of Geophysical Research: Solid Earth* 117.3, pp. 1–14. ISSN: 21699356. DOI: 10.1029/2011JB008925.

Furlong, Kevin P. and Susan Y. Schwartz (2004). "Influence of the Mendocino Triple Junction on the Tectonics of Coastal California". In: *Annual Review of Earth and Planetary Sciences* 32.1, pp. 403–433. ISSN: 0084-6597. DOI: 10.1146/annurev.earth.32.101802.120252. URL: http://www.annualreviews.org/doi/10.1146/annurev.earth.32.101802.120252.

Gao, Xiang and Kelin Wang (2017). "Rheological separation of the megathrust seismogenic zone and episodic tremor and slip". In: *Nature* 543.7645, pp. 416–419. ISSN: 14764687. DOI: 10.1038/nature21389.

Gardonio, B, R. Jolivet, E Calais, and H. Leclere (2018). "The April 2017 Mw6.5 Botswana Earthquake: An Intraplate Event Triggered by Deep Fluids". In: *Geophysical Research Letters* 45, pp. 8886–8896. DOI: 10.1029/2018GL078297.

Gomberg, J., A. Wech, K. Creager, K. Obara, and D. Agnew (2016). "Reconsidering earthquake scaling". In: *Geophysical Research Letters* 43.12, pp. 6243–6251. ISSN: 19448007. DOI: 10.1002/2016GL069967.

Groenewald, P. B., A. B. Moyes, G. H. Grantham, and J. R. Krynauw (1995). "East Antarctic crustal evolution: geological constraints and modelling in western Dronning Maud Land". In: *Precambrian Research* 75.3-4, pp. 231–250. ISSN: 03019268. DOI: 10.1016/0301-9268(95)80008-6.

Gu, Yanchao, Dongming Fan, and Wei You (2017). "Comparison of observed and modeled seasonal crustal vertical displacements derived from multi-institution GPS and GRACE solutions". In: *Geophysical Research Letters* 44.14, pp. 7219–7227. ISSN: 19448007. DOI: 10.1002/2017GL074264.

Gulick, Sean P S, Anne S. Meltzer, Timothy J. Henstock, and Alan Levander (2002). "Internal deformation of the southern Gorda plate: Fragmentattion of a weak plate near

the Mendocino triple junction". In: *Geology* 29.8, pp. 691–694. ISSN: 00917613. DOI: 10.1130/0091-7613(2001)029<0691:IDOTSG>2.0.CO;2.

Gumbricht, T, T S Mccarthy, and C L Merry (2001). "The topography of the Okavango Delta, Botswana, and its tectonic and sedimentological implications". In: *South African Journal of Geology* 104, pp. 243–264.

Hackl, M., R. Malservisi, U. Hugentobler, and R. Wonnacott (2011). "Estimation of velocity uncertainties from GPS time series: Examples from the analysis of the South African TrigNet network". In: *Journal of Geophysical Research: Solid Earth* 116.11, pp. 1–12. ISSN: 21699356. DOI: 10.1029/2010JB008142.

Hamiel, Yariv and Yuri Fialko (2007). "Structure and mechanical properties of faults in the North Anatolian Fault system from InSAR observations of coseismic deformation due to the 1999 Izmit (Turkey) earthquake". en. In: *Journal of Geophysical Research: Solid Earth* 112.B7, B07412. ISSN: 2156-2202. DOI: 10.1029/2006JB004777. URL: http://onlinelibrary.wiley.com/doi/10.1029/2006JB004777/abstract (visited on 04/05/2016).

Hammond, William C, Geoffrey Blewitt, and Corné Kreemer (2016). "GPS Imaging of Vertical Land Motion in California and Nevada: Implications for Sierra Nevada Uplift". In: *Journal of Geophysical Research : Solid Earth*. DOI: 10.1002/2016JB013458.Received.

Hanson, Richard E et al. (2004). "Coeval Large-Scale Magmatism in Cratons During Rodinia Assembly". In: *Science* 304.May, pp. 1126–1129.

Hao, Ming, Jeffrey T. Freymueller, Qingliang Wang, Duxin Cui, and Shanlan Qin (2016). "Vertical crustal movement around the southeastern Tibetan Plateau constrained by GPS and GRACE data". In: *Earth and Planetary Science Letters* 437, pp. 1–8. ISSN: 0012821X. DOI: 10.1016/j.epsl.2015.12.038. URL: http://dx.doi.org/10.1016/j.epsl.2015.12.038.

Harris, Ruth A. (2017). "Large earthquakes and creeping faults". In: *Reviews of Geophysics* 55, pp. 1–30. ISSN: 87551209. DOI: 10.1002/2016RG000539. URL: http://doi.wiley.com/10.1002/2016RG000539.

Hayes, Gavin P, David J Wald, and Rebecca L Johnson (2012). "Slab1 . 0 : A three fffdfffdfffd dimensional model of global subduction zone geometries". In: *Journal of Geophysical Research: Solid Earth* 117.September 2011, pp. 1–15. DOI: 10.1029/2011JB008524.

Heidbach, Oliver, Mark Tingay, Andreas Barth, John Reinecker, Daniel Kurfey, and Birgit Muller (2010). "Global crustal stress pattern based on the World Stress Map database release 2008". In: *Tectonophysics* 482, pp. 3–15.

Hengesh, James V. and John Wakabayashi (1995). "Dextral translation and progressive emergence of the pleistocene Merced basin and implications for the timing of initiation of the San Francisco Peninsula segment of the San Andreas Fault". In: *Recent Geologic Studes in the San Francisco Bay Area: Pacific section S.E.P.M* 76, pp. 47–53.

Henstock, Timothy J and Alan Levander (2003). "Structure and seismotectonics of the Mendocino Triple Junction , California". In: 108. DOI: 10.1029/2001JB000902.

Herring, Thomas A., Robert W. King, Michael A. Floyd, and Simon C. McClusky (2015). *Introduction to GAMIT/GLOBK, Release 10.6*. URL: http://www-gpsg.mit.edu/~simon/gtgk/Intro_GG.pdf.

Herring, Thomas A., Timothy I. Melbourne, et al. (2016). "Plate Boundary Observatory and related networks: GPS data analysis methods and geodetic products". In: *Reviews of Geophysics* 54.4, pp. 759–808. ISSN: 19449208. DOI: 10.1002/2016RG000529.

Higgins, Stephanie A., Irina Overeem, Michael S. Steckler, James P. M. Syvitski, Leonardo Seeber, and S. Humayun Akhter (2014). "InSAR measurements of compaction and subsidence in the Ganges-Brahmaputra Delta, Bangladesh". In: *Journal of Geophysical Research : Solid Earth* 119, pp. 1768–1781. DOI: 10.1002/2014JF003117.

Hill, Emma M., James L. Davis, Mark E. Tamisiea, Rui M. Ponte, and Nadya T. Vinogradova (2011). "Using a spatially realistic load model to assess impacts of Alaskan glacier ice loss on sea level". In: *Journal of Geophysical Research: Solid Earth* 116.10, pp. 1–9. ISSN: 21699356. DOI: 10.1029/2011JB008339.

Hinze, William J., Lawrence W. Braile, G. Randy Keller, and Edward G. Lidiak (1988). "Models for midcontinent tectonism: An Update". In: *Reviews of Geophysics* 26.4, pp. 699–717. ISSN: 19449208. DOI: 10.1029/RG026i004p00699.

Hirose, Hitoshi and Kazushige Obara (2005). "Repeating short- and long-term slow slip events with deep tremor activity around Bungo Channel region, southwest Japan". In: *Earth Planets Space* 57, pp. 961–972.

Hoffmann, Felix, Sabrina Metzger, Marcos Moreno, Zhiguo Deng, Christian Sippl, Francisco Ortega-Culaciati, and Onno Oncken (2018). "Characterizing Afterslip and Ground Displacement Rate Increase Following the 2014 Iquique-Pisagua Mw8.1 Earthquake, Northern Chile". In: *Journal of Geophysical Research : Solid Earth* 123, pp. 4171–4192. DOI: 10.1002/2017JB014970.

Hori, Kazuaki and Yoshiki Saito (2007). "Classification, Architecture, and Evolution of Large-river Deltas". In: *Large Rivers: Geomorphology and Management*. Ed. by Avijit Gupta. West Sussex, England: John Wiley & Sons Inc. Chap. 6, pp. 75–96.

Huang, Yihe, Jean-Paul Ampuero, and Don V. Helmberger (2016). "The potential for supershear earthquakes in damaged fault zones fffdfffdfffd theory and observations". In: *Earth and Planetary Science Letters* 433, pp. 109–115. ISSN: 0012-821X. DOI: 10.1016/j.epsl.2015.10.046. URL: http://www.sciencedirect.com/science/article/pii/S0012821X15006822 (visited on 04/05/2016).

Hyndman, R. D. (2013). "Downdip landward limit of Cascadia great earthquake rupture". In: *Journal of Geophysical Research: Solid Earth* 118.10, pp. 5530–5549. ISSN: 21699356. DOI: 10.1002/jgrb.50390.

Itaba, Satoshi and Ryosuke Ando (2011). "A slow slip event triggered by teleseismic surface waves". In: *Geophysical Research Letters* 38.21, pp. 1–5. ISSN: 00948276. DOI: 10.1029/2011GL049593.

Jachens, R. C. and M. L. Zoback (1999). "The San Andreas Fault in the San Francisco Bay Region, California: Structure and Kinematics of a Young Plate Boundary". In: *Interna-*

tional Geology Review 41.3, pp. 191–205. ISSN: 0020-6814. DOI: 10.1080/00206819909465139. URL: http://dx.doi.org/10.1080/00206819909465139 (visited on 04/20/2016).

James, D.E., M.J. Fouch, J.C. VanDecar, S. van der Lee, and Kaapvaal Seismic Group (2001). "Tectospheric structure beneath southern Africa". In: *Geophysical Research Letters* 28.13, pp. 2485–2488. ISSN: 0094-8276. DOI: 10.1029/2000GL012578.

James, Eric William (1992). "Cretaceous metamorphism and plutonism in the Santa Cruz Mountains, Salinian block, California, and correlation with the southernmost Sierra Nevada". en. In: *Geological Society of America Bulletin* 104.10, pp. 1326–1339. ISSN: 0016-7606, 1943-2674. DOI: 10.1130/0016-7606(1992)104<1326:CMAPIT>2.3.CO;2. URL: http://gsabulletin.gsapubs.org/content/104/10/1326 (visited on 04/19/2016).

Jara, Jorge, Anne Socquet, David Marsan, and Michel Bouchon (2017). "Long-Term Interactions Between Intermediate Depth and Shallow Seismicity in North Chile Subduction Zone". In: *Geophysical Research Letters* 44.18, pp. 9283–9292. ISSN: 19448007. DOI: 10.1002/2017GL075029.

Jeffreys, Harold (1961). *The Theory of Probability*. 3rd ed. Oxford University Press.

Ji, Chen, David J. Wald, and Donald V. Helmberger (2002). "Source description of the 1999 Hector Mine, California, earthquake, part I: Wavelet domain inversion theory and resolution analysis". In: *Bulletin of the Seismological Society of America* 92.4, pp. 1192–1207. ISSN: 00371106. DOI: 10.1785/0120000916.

Jiang, Junle and Nadia Lapusta (2016). "Deeper penetration of large earthquakes on seismically quiescent faults". en. In: *Science* 352.6291, pp. 1293–1297. ISSN: 0036-8075, 1095-9203. DOI: 10.1126/science.aaf1496. URL: http://science.sciencemag.org/content/352/6291/1293 (visited on 08/03/2016).

Johnson, Christopher W., Yuning Fu, and Roland Bürgmann (2017). "Seasonal water storage, stress modulation, and California seismicity". In: *Science* 356.6343, pp. 1161–1164. ISSN: 10959203. DOI: 10.1126/science.aak9547.

Johnson, Hadley O. and Duncan Carr Agnew (1995). "Monument motion and measurements of crustal velocities". In: *Geophysical Research Letters* 22.21, pp. 2905–2908. ISSN: 19448007. DOI: 10.1029/95GL02661.

Johnson, Paul A., Heather Savage, Matt Knuth, Joan Gomberg, and Chris Marone (2008). "Effects of acoustic waves on stick-slip in granular media and implications for earthquakes". In: *Nature* 451.7174, pp. 57–60. ISSN: 14764687. DOI: 10.1038/nature06440.

Johnston, Arch C (1989). "The seismicity of 'stable continental interiors'". In: *Earthquakes at North-Atlantic Passive Margins: Neotectonics and Postglacial Rebound*, pp. 299–327.

Jolivet, R., R. Bürgmann, and N. Houlié (2009). "Geodetic exploration of the elastic properties across and within the northern San Andreas Fault zone". In: *Earth and Planetary Science Letters* 288.1fffdfffdfffd2, pp. 126–131. ISSN: 0012-821X. DOI: 10.1016/j.epsl.2009.09.014. URL: http://www.sciencedirect.com/science/article/pii/S0012821X09005470 (visited on 04/05/2016).

Jonsson, Sigurjon, Howard Zebker, Paul Segall, and Falk Amelung (2002). "Fault Slip Distribution of the 1999 M w 7 . 1 Hector Mine , California , Earthquake , Estimated from

Satellite Radar and GPS Measurements". In: *Bulletin of the Seismological Society of America* 92.4, pp. 1377–1389.

Kanamori, Hiroo and Don Anderson (1975). "Theoretical basis of some empirical relations in seismology". In: *Bulletin of the Seismological Society of America* 65.5, pp. 1073–1095.

Kenner, S J and P Segall (2000). "A mechanical model for intraplate earthquakes: Application to the New Madrid Seismic Zone". In: *Science* 289.5488, pp. 2329–2332. ISSN: 00368075. DOI: 10.1126/science.289.5488.2329.

Kennett, B.L.N., E.R. Engdahl, and R. Buland (1995). "Constraints on seismic velocities in the Earth from traveltimes". In: *Geophysical Journal International* 122, pp. 108–124. DOI: https://doi.org/10.1111/j.1365-246X.1995.tb03540.x.

Key, Roger M. and Neil Ayres (2000). "The 1998 edition of the National Geological Map of Botswana". In: *Journal of African Earth Sciences* 30.3, pp. 427–451. ISSN: 08995362. DOI: 10.1016/S0899-5362(00)00030-0.

Kinabo, B. D., E. A. Atekwana, J. P. Hogan, M. P. Modisi, D. D. Wheaton, and A. B. Kampunzu (2007). "Early structural development of the Okavango rift zone, NW Botswana". In: *Journal of African Earth Sciences* 48.2-3, pp. 125–136. ISSN: 08995362. DOI: 10.1016/j.jafrearsci.2007.02.005.

Kinabo, B. D., J. P. Hogan, Estella A. Atekwana, M. G. Abdelsalam, and M. P. Modisi (2008). "Fault growth and propagation during incipient continental rifting: Insight from a combined aeromagnetic and Shuttle Radar Topography Mission digital elevation model investigation of the Okavango Rift Zone, northwest Botswana". In: *Tectonics* 27.3, pp. 1–16. ISSN: 02787407. DOI: 10.1029/2007TC002154.

Klein, E., Z. Duputel, D. Zigone, C. Vigny, J. P. Boy, C. Doubre, and G. Meneses (2018). "Deep Transient Slow Slip Detected by Survey GPS in the Region of Atacama, Chile". In: *Geophysical Research Letters* 45.22, pp. 12, 263–12, 273. ISSN: 19448007. DOI: 10.1029/2018GL080613.

Klose, Christian D and Leonardo Seeber (2007). "Shallow seismicity in stable continental regions". In: *Seismological Research Letters* 78.5, pp. 554–562. ISSN: 0895-0695. DOI: 10.1785/gssrl.78.5.554. URL: http://www.ncbi.nlm.nih.gov/entrez/query.fcgi?db=pubmed%7B%5C&%7Dcmd=Retrieve%7B%5C&%7Ddopt=AbstractPlus%7B%5C&%7Dlist%7B%5C_%7Duids=000249462100008%7B%5C%7D5Cnpapers2://publication/uuid/DCDE123C-1AB3-43E8-B377-34739BB27D3C.

Kolawole, F., E. A. Atekwana, S. Malloy, D. S. Stamps, R. Grandin, M. G. Abdelsalam, K. Leseane, and E. M. Shemang (2017). "Aeromagnetic, gravity, and Differential Interferometric Synthetic Aperture Radar analyses reveal the causative fault of the 3 April 2017 Mw6.5 Moiyabana, Botswana, earthquake". In: *Geophysical Research Letters* 44, pp. 1–10. DOI: 10.1002/2017GL074620.

Kruschke, John (2015). *Doing Bayesian Data Analysis: A Tutorial with R, JAGS, and Stan*. 2nd ed. London: Academic Press.

Landerer, F. W. and S. C. Swenson (2012). "Accuracy of scaled GRACE terrestrial water storage estimates". In: *Water Resources Research* 48.4, pp. 1–11. ISSN: 00431397. DOI: 10.1029/2011WR011453.

Langbein, John and Jerry L. Svarc (2019). "Evaluation of temporally correlated noise in GNSS time series: geodetic monument performance". In: *Journal of Geophysical Research: Solid Earth* 124, pp. 1–18. ISSN: 21699313. DOI: 10.1029/2018JB016783. URL: http://doi.wiley.com/10.1029/2018JB016783.

Le Gall, Bernard, Gomotsang Tshoso, Jérôme Dyment, Ali Basira Kampunzu, Fred Jourdan, Gilbert Féraud, Hervé Bertrand, Charly Aubourg, and William Vétel (2005). "The Okavango giant mafic dyke swarm (NE Botswana): Its structural significance within the Karoo Large Igneous Province". In: *Journal of Structural Geology* 27.12, pp. 2234–2255. ISSN: 01918141. DOI: 10.1016/j.jsg.2005.07.004.

Le Pichon, X., C. Kreemer, and N. Chamot-Rooke (2005). "Asymmetry in elastic properties and the evolution of large continental strike-slip faults". In: *Journal of Geophysical Research* 110.B03405.

Leitner, Beate, Anne M Trehu, and J Godfrey (1998). "Crustal structure of the northestern Vizcaino block and Gorda Escarpment, offshore northern California, and implications for postsubduction deformation of a paleoaccretionary margin". In: *Journal of Geophysical Research* 103.B10, pp. 23795–23812. DOI: 10.1029/98JB02050.

Lenardic, A, L Moresi, and H Muhlhaus (2000). "The role of mobile belts for the longevity of deep cratonic lithosphere: The crumple zone model". In: *Geophysical Research Letters* 27.8, pp. 1235–1238.

Li, Shanshan, Jeffrey Freymueller, and Robert McCaffrey (2016). "Slow Slip Events and Time-Dependent Variations in Locking Beneath Lower Cook Inlet of the Alaska-Aleutian Subduction Zone\". In: *Journal of Geophysical Research : Solid Earth* 121, pp. 1060–1079. DOI: 10.1002/2015JB012491.Received.

Li, Yong-Gang, John E. Vidale, and Elizabeth S. Cochran (2004). "Low-velocity damaged structure of the San Andreas Fault at Parkfield from fault zone trapped waves". en. In: *Geophysical Research Letters* 31.12, L12S06. ISSN: 1944-8007. DOI: 10.1029/2003GL019044. URL: http://onlinelibrary.wiley.com/doi/10.1029/2003GL019044/abstract (visited on 04/05/2016).

Lienkaemper, James J., Forrest S. McFarland, Robert W. Simpson, and S. John Caskey (2014). "Using Surface Creep Rate to Infer Fraction Locked for Sections of the San Andreas Fault System in Northern California from Alignment Array and GPS Data". en. In: *Bulletin of the Seismological Society of America* 104.6, pp. 3094–3114. ISSN: 0037-1106, 1943-3573. DOI: 10.1785/0120140117. URL: http://bssa.geoscienceworld.org/content/104/6/3094 (visited on 04/08/2016).

Lindsey, E. O. and Y. Fialko (2013). "Geodetic slip rates in the southern San Andreas Fault system: Effects of elastic heterogeneity and fault geometry". en. In: *Journal of Geophysical Research: Solid Earth* 118.2, pp. 689–697. ISSN: 2169-9356. DOI: 10.1029/2012JB009358. URL: http://onlinelibrary.wiley.com/doi/10.1029/2012JB009358/abstract (visited on 04/05/2016).

Lindsey, Eric O., Yuri Fialko, Yehuda Bock, David T. Sandwell, and Roger Bilham (2014). "Localized and distributed creep along the southern San Andreas Fault". en. In: *Journal of Geophysical Research: Solid Earth* 119.10, pp. 7909–7922. ISSN: 2169-9356. DOI:

10.1002/2014JB011275. URL: http://onlinelibrary.wiley.com/doi/10.1002/2014JB011275/abstract (visited on 04/05/2016).

Lindsey, Eric O., Valerie J. Sahakian, Yuri Fialko, Yehuda Bock, Sylvain Barbot, and Thomas K. Rockwell (2013). "Interseismic Strain Localization in the San Jacinto Fault Zone". en. In: *Pure and Applied Geophysics* 171.11, pp. 2937–2954. ISSN: 0033-4553, 1420-9136. DOI: 10.1007/s00024-013-0753-z. URL: http://link.springer.com/article/10.1007/s00024-013-0753-z (visited on 08/03/2016).

Lisowski, M., J. C. Savage, and W. H. Prescott (1991). "The velocity field along the San Andreas Fault in central and southern California". en. In: *Journal of Geophysical Research: Solid Earth* 96.B5, pp. 8369–8389. ISSN: 2156-2202. DOI: 10.1029/91JB00199. URL: http://onlinelibrary.wiley.com/doi/10.1029/91JB00199/abstract (visited on 04/05/2016).

Liu, Lanbo and Mark D Zoback (1997). "Lithospheric strength and intraplate seismicity in the New Madrid Seismic Zone". In: *Tectonics* 16.4, pp. 585–595.

Mallick, Rishav, Eric O. Lindsey, Lujia Feng, Judith Hubbard, Paramesh Banerjee, and Emma M. Hill (2019). "Active Convergence of the India-Burma-Sunda Plates Revealed by a New Continuous GPS Network". In: *Journal of Geophysical Research: Solid Earth* 124.3, pp. 3155–3171. ISSN: 21699356. DOI: 10.1029/2018JB016480.

Mao, Ailin, G A Harrison, and H Dixon (1999). "Noise in GPS coordinate time series". In: *Journal of Geophysical Research* 104, pp. 2797–2816.

Mapeo, R B M, R A Armstrong, and A B Kampunzu (2001). "SHRIMP U fffdfffdfffd Pb zircon geochronology of gneisses from the Gweta borehole, northeast Botswana : implications for the Palaeoproterozoic Magondi Belt in southern Africa". In: *Africa* 138.3, pp. 299–308. ISSN: 0016-7568. DOI: 10.1017/S001675680100526X.

Materna, K. and R. Bürgmann (2016). "Contrasts in compliant fault zone properties inferred from geodetic measurements in the San Francisco Bay area". In: *Journal of Geophysical Research: Solid Earth* 121.9. ISSN: 21699356. DOI: 10.1002/2016JB013243.

Materna, K., T. Taira, and R. Bürgmann (2018). "Aseismic Transform Fault Slip at the Mendocino Triple Junction From Characteristically Repeating Earthquakes". In: *Geophysical Research Letters* 45.2. ISSN: 19448007. DOI: 10.1002/2017GL075899.

Materna, Kathryn, Shengji Wei, Xin Wang, Luo Heng, Teng Wang, Weiwen Chen, Rino Salman, and Roland Bürgmann (2019). "Source characteristics of the 2017 Mw6.4 Moijabana, Botswana earthquake, a rare lower-crustal event within an ancient zone of weakness". In: *Earth and Planetary Science Letters* 506, pp. 348–359. ISSN: 0012821X. DOI: 10.1016/j.epsl.2018.11.007. URL: https://linkinghub.elsevier.com/retrieve/pii/S0012821X18306587.

Matsubara, Makoto, Kazushige Obara, and Keiji Kasahara (2009). "High-VP/VSzone accompanying non-volcanic tremors and slow-slip events beneath southwestern Japan". In: *Tectonophysics* 472.1-4, pp. 6–17. ISSN: 00401951. DOI: 10.1016/j.tecto.2008.06.013. URL: http://dx.doi.org/10.1016/j.tecto.2008.06.013.

Mattinson, James M. (1978). "Age, origin, and thermal histories of some plutonic rocks from the Salinian block of California". en. In: *Contributions to Mineralogy and Petrology*

67.3, pp. 233–245. ISSN: 0010-7999, 1432-0967. DOI: 10.1007/BF00381451. URL: http://link.springer.com/article/10.1007/BF00381451 (visited on 04/19/2016).

McCaffrey, Robert, Maureen D. Long, Chris Goldfinger, Peter C. Zwick, John L. Nabelek, Cheryl K. Johnson, and Curt Smith (2000). "Rotation and plate locking at the Southern Cascadia Subduction Zone". In: *Geophysical Research Letters* 27.19, pp. 3117–3120. ISSN: 0094-8276. DOI: 10.1029/2000GL011768.

McCaffrey, Robert, Anthony I. Qamar, Robert W. King, Ray Wells, Giorgi Khazaradze, Charles A. Williams, Colleen W. Stevens, Jesse J. Vollick, and Peter C. Zwick (2007). "Fault locking, block rotation and crustal deformation in the Pacific Northwest". In: *Geophysical Journal International* 169.3, pp. 1315–1340. ISSN: 0956540X. DOI: 10.1111/j.1365-246X.2007.03371.x.

McCrory, Patricia A., J. Luke Blair, Felix Waldhauser, and David H. Oppenheimer (2012). "Juan de Fuca slab geometry and its relation to Wadati-Benioff zone seismicity". In: *Journal of Geophysical Research: Solid Earth* 117.9, pp. 1–24. ISSN: 21699356. DOI: 10.1029/2012JB009407.

McGuire, J. J., M. S. Boettcher, and T. H. Jordan (2005). "Foreshock sequences and short-term earthquake predictability on East Pacific Rise transform faults." In: *Nature* 434.7032, pp. 457–461. ISSN: 0028-0836. DOI: 10.1038/nature03621.

McGuire, Jeffrey J. and John A. Collins (2013). "Millimeter-level precision in a seafloor geodesy experiment at the Discovery transform fault, East Pacific Rise". In: *Geochemistry, Geophysics, Geosystems* 14.10, pp. 4392–4402. ISSN: 15252027. DOI: 10.1002/ggge.20225.

Meng, Lingsen, Hui Huang, Roland Bürgmann, Jean Paul, and Anne Strader (2015). "Dual megathrust slip behaviors of the 2014 Iquique earthquake sequence". In: *Earth and Planetary Science Letters* 411, pp. 177–187. ISSN: 0012-821X. DOI: 10.1016/j.epsl.2014.11.041. URL: http://dx.doi.org/10.1016/j.epsl.2014.11.041.

Metropolis, Nicholas, Arianna W. Rosenbluth, Marshall N. Rosenbluth, Augusta H. Teller, and Edward Teller (1953). "Equation of State Calculations by Fast Computing Machines". In: *The Journal of Chemical Physics* 21.6, pp. 1087–1092. ISSN: 0021-9606, 1089-7690. DOI: 10.1063/1.1699114. URL: http://scitation.aip.org/content/aip/journal/jcp/21/6/10.1063/1.1699114 (visited on 04/20/2016).

Michel, Sylvain, Adriano Gualandi, and Jean-Philippe Avouac (2018). "Interseismic Coupling and Slow Slip Events on the Cascadia Megathrust". In: *Pure and Applied Geophysics*. ISSN: 0033-4553. DOI: 10.1007/s00024-018-2006-7.

Milliner, Chris, Kathryn Materna, Roland Bürgmann, Yuning Fu, Angelyn W. Moore, David Bekaert, Surendra Adhikari, and Donald F. Argus (2018). "Tracking the weight of Hurricane Harvey's stormwater using GPS data". In: *Science Advances* 4.9. ISSN: 23752548. DOI: 10.1126/sciadv.aau2477.

Millonig, Leo, Armin Zeh, Axel Gerdes, Reiner Klemd, and Jackson M. Barton (2010). "Decompressional heating of the Mahalapye Complex (Limpopo Belt, Botswana): A response to Palaeoproterozoic magmatic underplating?" In: *Journal of Petrology* 51.3, pp. 703–729. ISSN: 00223530. DOI: 10.1093/petrology/egp097.

Mitchell, Kenneth E. (2004). "The multi-institution North American Land Data Assimilation System (NLDAS): Utilizing multiple GCIP products and partners in a continental distributed hydrological modeling system". In: *Journal of Geophysical Research* 109.D7, pp. 1–32. ISSN: 0148-0227. DOI: 10.1029/2003jd003823.

Miyazawa, Masatoshi, Emily E. Brodsky, and Jim Mori (2008). "Learning from dynamic triggering of low-frequency tremor in subduction zones". In: *Earth, Planets and Space* 60.10, e17–e20. ISSN: 18805981. DOI: 10.1186/BF03352858.

Modisi, M. P., E. A. Atekwana, A. B. Kampunzu, and T. H. Ngwisanyi (2000). "Rift kinematics during the incipient stages of continental extension: Evidence the nascent Okavango rift basin, Northwest Botswana". In: *Geology* 28.10, pp. 939–942. ISSN: 00917613. DOI: 10.1130/0091-7613(2000)28<939:RKDTIS>2.0.CO;2.

Mooney, Walter D, Jeroen Ritsema, and Yong Keun (2012). "Crustal seismicity and the earthquake catalog maximum moment magnitude (M cmax) in stable continental regions (SCRs): Correlation with the seismic velocity of the lithosphere". In: *Earth and Planetary Science Letters* 357-358, pp. 78–83. ISSN: 0012-821X. DOI: 10.1016/j.epsl.2012.08.032. URL: http://dx.doi.org/10.1016/j.epsl.2012.08.032.

Mukherjee, Abhijit, Alan E. Fryar, and William A. Thomas (2009). "Geologic, geomorphic and hydrologic framework and evolution of the Bengal basin, India and Bangladesh". In: *Journal of Asian Earth Sciences* 34.3, pp. 227–244. ISSN: 13679120. DOI: 10.1016/j.jseaes.2008.05.011. URL: http://dx.doi.org/10.1016/j.jseaes.2008.05.011.

Nadeau, R. M. and T. V. McEvilly (1997). "Seismological studies at Parkfield V: Characteristic microearthquake sequences as fault-Zone drilling targets". In: *Bulletin of the Seismological Society of America* 87.6, pp. 1463–1472. ISSN: 00371106.

Nadeau, Robert M. and Lane R. Johnson (1998). "Seismological Studies at Parkfield VI : Moment Release Rates and Estimates of Source Parameters for Small Repeating Earthquakes". In: 88.3, pp. 790–814.

Nadeau, Robert M and Thomas V McEvilly (2004). "Periodic pulsing of characteristic microearthquakes on the San Andreas fault." In: *Science (New York, N.Y.)* 303.5655, pp. 220–222. ISSN: 0036-8075. DOI: 10.1126/science.1090353.

Nakajima, Junichi and Naoki Uchida (2018). "Repeated drainage from megathrusts during episodic slow slip". In: *Nature Geoscience* 11.5, pp. 351–356. ISSN: 17520908. DOI: 10.1038/s41561-018-0090-z. URL: http://dx.doi.org/10.1038/s41561-018-0090-z.

Neal, Radford (2003). "Slice Sampling". In: *Annals of Statistics* 31.3, pp. 705–741.

Nguuri, T K, J Gore, D E James, S J Webb, C Wright, T G Zengeni, O Gwavava, and J A Snoke (2001). "Crustal structure beneath southern Africa and its implications for the formation and evolution of the Kaapvaal and Zimbabwe cratons". In: *Geophysical Research Letters* 28.13, pp. 2501–2504. ISSN: 00948276. DOI: 10.1029/2000gl012587.GEOPHYSICAL.

Obara, Kazushige and Aitaro Kato (2016). "Connecting slow earthquakes to huge earthquakes". In: *Science* 353.6296, pp. 253–257. ISSN: 10959203. DOI: 10.1126/science.aaf1512.

Okada (1992). "Internal deformation due to shear and tensile faults in a half space". In: *Bulletin of the Seismological Society of America* 82.2, pp. 1018–1040. ISSN: 0037-1106. URL: http://bssa.geoscienceworld.org/content/82/2/1018.short.

Okada, Yoshimitsu (1985). "Surface deformation due to shear and tensile faults in a half-space". In: *Bulletin of the Seismological Society of America* 75.4, pp. 1135–1154.

Oppenheimer, D et al. (1993). "The cape mendocino, california, earthquakes of april 1992: subduction at the triple junction." In: *Science (New York, N.Y.)* 261.5120, pp. 433–438. ISSN: 0036-8075 (Print). DOI: 10.1126/science.261.5120.433.

Parsons, Tom and Mary Lou Zoback (1997). "Three-dimensional upper crustal velocity structure beneath San Francisco Peninsula, California". en. In: *Journal of Geophysical Research: Solid Earth* 102.B3, pp. 5473–5490. ISSN: 2156-2202. DOI: 10.1029/96JB03222. URL: http://onlinelibrary.wiley.com/doi/10.1029/96JB03222/abstract (visited on 04/05/2016).

Patil, Anand, David Huard, and Christopher J. Fonnesbeck (2010). "PyMC: Bayesian Stochastic Modelling in Python". In: *Journal of statistical software* 35.4, pp. 1–81. ISSN: 1548-7660. URL: http://www.ncbi.nlm.nih.gov/pmc/articles/PMC3097064/ (visited on 04/20/2016).

Pollitz, F. F., Patricia McCrory, Doug Wilson, Jerry Svarc, Christine Puskas, and Robert B. Smith (2010). "Viscoelastic-cycle model of interseismic deformation in the northwestern United States". In: *Geophysical Journal International* 181.2, pp. 665–696. ISSN: 0956540X. DOI: 10.1111/j.1365-246X.2010.04546.x.

Pollitz, Fred F., Louise Kellogg, and Roland Bürgmann (2001). "Sinking mafic body in a reactivated lower crust: A mechanism for stress concentration at the New Madrid seismic zone". In: *Bulletin of the Seismological Society of America* 91.6, pp. 1882–1897. ISSN: 00371106. DOI: 10.1785/0120000277.

Pollitz, Fred F., Aaron Wech, Honn Kao, and Roland Bürgmann (2013). "Annual modulation of non-volcanic tremor in northern Cascadia". In: *Journal of Geophysical Research: Solid Earth* 118.5, pp. 2445–2459. ISSN: 21699356. DOI: 10.1002/jgrb.50181.

Powell, Robert E. (1993). "Balanced palinspastic reconstruction of pre-late Cenozoic paleogeology, southern California: Geologic and kinematic constraints on evolution of the San Andreas fault system". In: *The San Andreas Fault System: Displacement, Palinspastic Reconstruction, and Geologic Evolution*. Geological Society of America Memoir 178. Boulder, Colorado, pp. 1–106.

Prawirodirdjo, L., R. McCaffrey, David Chadwell, Yehuda Bock, and Cecep Subarya (2010). "Geodetic observations of an earthquake cycle at the Sumatra Subduction Zone: Role of interseismic strain segmentation". In: *Journal of Geophysical Research* 115.B03414. ISSN: 19448007. DOI: 10.1029/97GL52691.

Prescott, William H. (1981). "The determination of displacement fields from geodetic data along a strike slip fault". en. In: *Journal of Geophysical Research: Solid Earth* 86.B7, pp. 6067–6072. ISSN: 2156-2202. DOI: 10.1029/JB086iB07p06067. URL: http://onlinelibrary.wiley.com/doi/10.1029/JB086iB07p06067/abstract (visited on 04/05/2016).

Priestley, Keith, Dan Mckenzie, and Eric Debayle (2006). "The state of the upper mantle beneath southern Africa". In: *Tectonophysics* 416, pp. 101–112. DOI: 10.1016/j.tecto.2005.11.024.

Puskas, Christine M, Charles M Meertens, and David Phillips (2017). "Hydrologic Loading Model Displacements from the National and Global Data Assimilation Systems (NLDAS and GLDAS)". In: URL: https://www.unavco.org/data/gps-gnss/associated-products/hydrological/displacement-model-readme.pdf.

Radiguet, M., F. Cotton, M. Vergnolle, M. Campillo, A. Walpersdorf, N. Cotte, and V. Kostoglodov (2012). "Slow slip events and strain accumulation in the Guerrero gap, Mexico". In: *Journal of Geophysical Research: Solid Earth* 117.4. ISSN: 21699356. DOI: 10.1029/2011JB008801.

Ranganai, R. T., A. B. Kampunzu, E. A. Atekwana, B. K. Paya, J. G. King, D. I. Koosimile, and E. H. Stettler (2002). "Gravity evidence for a larger Limpopo Belt in southern Africa and geodynamic implications". In: *Geophysical Journal International* 149.3. ISSN: 0956540X. DOI: 10.1046/j.1365-246X.2002.01703.x.

Reeves, C. V. (1972). "Rifting in the Kalahari?" In: *Nature* 239, pp. 73–78.

Reinoza, C., F. Jouanne, F. A. Audemard, M. Schmitz, and C. Beck (2015). "Geodetic exploration of strain along the El Pilar Fault in northeastern Venezuela". en. In: *Journal of Geophysical Research: Solid Earth* 120.3, 2014JB011483. ISSN: 2169-9356. DOI: 10.1002/2014JB011483. URL: http://onlinelibrary.wiley.com/doi/10.1002/2014JB011483/abstract (visited on 08/01/2016).

Robert Engdahl, E., Rob Der Van Hilst, and Raymond Buland (1998). "Global teleseismic earthquake relocation with improved travel times and procedures for depth determination". In: *Bulletin of the Seismological Society of America* 88.3, pp. 722–743. ISSN: 00371106. DOI: 10.1130/0-8137-2349-3.461.

Rollins, John C and Ross S Stein (2010). "Coulomb stress interactions among M fffdfffdfffd 5 . 9 earthquakes in the Gorda deformation zone and on the Mendocino Fault Zone , Cascadia subduction zone , and northern San Andreas Fault". In: *Journal of Geophysical Research* 115. DOI: 10.1029/2009JB007117.

Rybicki, Kacper and Keichi Kasahara (1977). "A strike-slip fault in a laterally inhomogeneous medium". In: *Tectonophysics* 42.2, pp. 127–138. ISSN: 0040-1951. DOI: 10.1016/0040-1951(77)90164-0. URL: http://www.sciencedirect.com/science/article/pii/0040195177901640 (visited on 04/05/2016).

Sakumura, C., S. Bettadpur, and S. Bruinsma (2014). "Ensemble prediction and intercomparison analysis of GRACE time-variable gravity field models". In: *Geophysical Research Letters* 41.5, pp. 1389–1397. ISSN: 19448007. DOI: 10.1002/2013GL058632.

Savage, J. C. and R. O. Burford (1973). "Geodetic determination of relative plate motion in central California". en. In: *Journal of Geophysical Research* 78.5, pp. 832–845. ISSN: 2156-2202. DOI: 10.1029/JB078i005p00832. URL: http://onlinelibrary.wiley.com/doi/10.1029/JB078i005p00832/abstract (visited on 04/05/2016).

Schluter, Thomas (2006). "Botswana". In: *Geological Atlas of Africa: With Notes on Stratigraphy, Tectonics, Economic Geology, Geohazards and Geosites of Each Country*. Berlin: Springer. Chap. Botswana, pp. 46–49. ISBN: 9783540291459.

Schmalzle, Gina M., Robert McCaffrey, and Kenneth C. Creager (2014). "Central Cascadia subduction zone creep". In: *Geochemistry, Geophysics, Geosystems* 15.4, pp. 1515–1532. ISSN: 15252027. DOI: 10.1002/2013GC005172.

Scholz, C H (1998). "Earthquakes and friction laws". In: *Nature* 391.6662, pp. 37–42. ISSN: 0028-0836. DOI: 10.1038/34097. URL: http://dx.doi.org/10.1038/34097.

Scholz, C. H. (1985). "The Black Mountain asperity: Seismic hazard of the southern San Francisco Peninsula, California". en. In: *Geophysical Research Letters* 12.10, pp. 717–719. ISSN: 1944-8007. DOI: 10.1029/GL012i010p00717. URL: http://onlinelibrary.wiley.com/doi/10.1029/GL012i010p00717/abstract (visited on 04/05/2016).

Segall, Paul (2010). *Earthquake and Volcano Deformation*. STU-Student Edition. Princeton University Press.

Serpelloni, Enrico, Claudio Faccenna, Giorgio Spada, Danan Dong, and Simon D.P. Williams (2013). "Vertical GPS ground motion rates in the Euro-Mediterranean region: New evidence of velocity gradients at different spatial scales along the Nubia-Eurasia plate boundary". In: *Journal of Geophysical Research: Solid Earth* 118.11, pp. 6003–6024. ISSN: 21699356. DOI: 10.1002/2013JB010102.

Shelly, David R., Gregory C. Beroza, and Satoshi Ide (2007). "Non-volcanic tremor and low-frequency earthquake swarms". In: *Nature* 446.7133, pp. 305–307. ISSN: 14764687. DOI: 10.1038/nature05666. arXiv: arXiv:1011.1669v3.

Smith-Konter, Bridget R., David T. Sandwell, and Peter Shearer (2011). "Locking depths estimated from geodesy and seismology along the San Andreas Fault System: Implications for seismic moment release". en. In: *Journal of Geophysical Research: Solid Earth* 116.B6, B06401. ISSN: 2156-2202. DOI: 10.1029/2010JB008117. URL: http://onlinelibrary.wiley.com/doi/10.1029/2010JB008117/abstract (visited on 08/03/2016).

Song, Seok Goo, Gregory C. Beroza, and Paul Segall (2008). "A Unified Source Model for the 1906 San Francisco Earthquake". en. In: *Bulletin of the Seismological Society of America* 98.2, pp. 823–831. ISSN: 0037-1106, 1943-3573. DOI: 10.1785/0120060402. URL: http://bssa.geoscienceworld.org/content/98/2/823 (visited on 04/05/2016).

Stamps, D S, L M Flesch, E Calais, and A Ghosh (2014). "Current kinematics and dynamics of Africa and the East". In: *Journal of Geophysical Research: Solid Earth* 119.May, pp. 1–26. DOI: 10.1002/2013JB010717.

Stamps, D. Sarah, Eric Calais, Elifuraha Saria, Chris Hartnady, Jean Mathieu Nocquet, Cynthia J. Ebinger, and Rui M. Fernandes (2008). "A kinematic model for the East African Rift". In: *Geophysical Research Letters* 35.5, pp. 1–6. ISSN: 00948276. DOI: 10.1029/2007GL032781.

Steckler, Michael S., Dhiman Ranjan Mondal, Syed Humayun Akhter, Leonardo Seeber, Lujia Feng, Jonathan Gale, Emma M. Hill, and Michael Howe (2016). "Locked and loading megathrust linked to active subduction beneath the Indo-Burman Ranges". In: *Nature Geoscience* 9.8, pp. 615–618. ISSN: 17520908. DOI: 10.1038/ngeo2760.

Steckler, Michael S., Scott L. Nooner, S. Humayun Akhter, Sazedul K. Chowdhury, Srinivas Bettadpur, Leonardo Seeber, and Mikhail G. Kogan (2010). "Modeling earth deformation from monsoonal flooding in Bangladesh using hydrographic, GPS, and gravity recovery and climate experiment (GRACE) data". In: *Journal of Geophysical Research: Solid Earth* 115.8, pp. 1–18. ISSN: 21699356. DOI: 10.1029/2009JB007018.

Stephenson, W. J. (2007). *Velocity and density models incorporating the Cascadia subduction zone for 3D earthquake ground motion simulations*. Tech. rep. U.S. Geological Survey, Earthquake Hazards Ground Motion Investigations, Open-File Report, 24p.

Swenson, Sean and John Wahr (2006). "Post-processing removal of correlated errors in GRACE data". In: *Geophysical Research Letters* 33.8, pp. 1–4. ISSN: 00948276. DOI: 10.1029/2005GL025285.

Templeton, Dennise C., Robert M. Nadeau, and Roland Bürgmann (2008). "Behavior of repeating earthquake sequences in Central California and the implications for subsurface fault creep". In: *Bulletin of the Seismological Society of America* 98.1, pp. 52–65. ISSN: 00371106. DOI: 10.1785/0120070026.

Thomas, A. L. (1993). "Poly3D: A threefffdfffdfffddimensional, polygonal element, displacement discontinuity boundary element computer program with applications to fractures, faults, and cavities in the Earth's crust". PhD thesis. Stanford University.

Thurber, Clifford H., Thomas M. Brocher, Haijiang Zhang, and Victoria E. Langenheim (2007). "Three-dimensional P wave velocity model for the San Francisco Bay region, California". en. In: *Journal of Geophysical Research: Solid Earth* 112.B7, B07313. ISSN: 2156-2202. DOI: 10.1029/2006JB004682. URL: http://onlinelibrary.wiley.com/doi/10.1029/2006JB004682/abstract (visited on 04/25/2016).

Tian, Yunfeng and Zheng Kang Shen (2016). "Extracting the regional common-mode component of GPS station position time series from dense continuous network". In: *Journal of Geophysical Research: Solid Earth* 121.2, pp. 1080–1096. ISSN: 21699356. DOI: 10.1002/2015JB012253.

Tormann, T, S Wiemer, and A Mignan (2014). "Systematic survey of high-resolution b value imaging along Californian faults : Inference on asperities". In: *Journal of Geophysical Research: Solid Earth* 119, pp. 2029–2054. DOI: 10.1002/2013JB010867.

Tregoning, P., C. Watson, G. Ramillien, H. McQueen, and J. Zhang (2009). "Detecting hydrologic deformation using GRACE and GPS". In: *Geophysical Research Letters* 36.15, pp. 1–6. ISSN: 00948276. DOI: 10.1029/2009GL038718.

Uchida, Naoki and Toru Matsuzawa (2011). "Coupling coefficient, hierarchical structure, and earthquake cycle for the source area of the 2011 off the Pacific coast of Tohoku earthquake inferred from small repeating earthquake data". In: *Earth, Planets and Space* 63.7, pp. 675–679. ISSN: 13438832. DOI: 10.5047/eps.20U.07.006.

— (2013). "Pre- and postseismic slow slip surrounding the 2011 Tohoku-oki earthquake rupture". In: *Earth and Planetary Science Letters* 374, pp. 81–91. ISSN: 0012821X. DOI: 10.1016/j.epsl.2013.05.021. URL: http://dx.doi.org/10.1016/j.epsl.2013.05.021.

Uchida, Naoki, Junichi Nakajima, Akira Hasegawa, and Toru Matsuzawa (2009). "What controls interplate coupling?: Evidence for abrupt change in coupling across a border between two overlying plates in the NE Japan subduction zone". In: *Earth and Planetary Science Letters* 283.1-4, pp. 111–121. ISSN: 0012821X. DOI: 10.1016/j.epsl.2009.04.003. URL: http://dx.doi.org/10.1016/j.epsl.2009.04.003.

Vallee, M., J. Charlety, A.M.G. Ferreira, B. Delouis, and J. Vergoz (2011). "SCARDEC: a new technique for the rapid determination of seismic moment magnitude, focal mechanism, and source time functions for large earthquakes using body wave deconvolution". In: *Geophysical Journal International* 184, pp. 338–358.

Van Dam, Tonie, J. Ray, A. Sheehan, Thomas A. Herring, Mark H. Murray, and Geoffrey Blewitt (2016). "Interpreting the GNSS Vertical Coordinate Variations". In: *American Geophysical Union Fall Meeting*. San Francisco, CA, abstract #G13C03.

Wahr, John, Shfaqat A. Khan, Tonie Van Dam, Lin Liu, Jan H. Van Angelen, Michiel R. Van Den Broeke, and Charles M. Meertens (2013). "The use of GPS horizontals for loading studies, with applications to northern California and southeast Greenland". In: *Journal of Geophysical Research: Solid Earth* 118.4, pp. 1795–1806. ISSN: 21699356. DOI: 10.1002/jgrb.50104.

Waldhauser, Felix and David P. Schaff (2008a). "Large-scale relocation of two decades of Northern California seismicity using cross-correlation and double-difference methods". en. In: *Journal of Geophysical Research: Solid Earth* 113.B8, B08311. ISSN: 2156-2202. DOI: 10.1029/2007JB005479. URL: http://onlinelibrary.wiley.com/doi/10.1029/2007JB005479/abstract (visited on 08/02/2016).

— (2008b). "Large-scale relocation of two decades of Northern California seismicity using cross-correlation and double-difference methods". In: *Journal of Geophysical Research* 113.B8, B08311. ISSN: 0148-0227. DOI: 10.1029/2007JB005479. URL: http://doi.wiley.com/10.1029/2007JB005479.

Wallace, Laura M., Yoshihiro Kaneko, Sigrún Hreinsdóttir, Ian Hamling, Zhigang Peng, Noel Bartlow, Elisabetta D'Anastasio, and Bill Fry (2017). "Large-scale dynamic triggering of shallow slow slip enhanced by overlying sedimentary wedge". In: *Nature Geoscience* 10.10, pp. 765–770. ISSN: 17520908. DOI: 10.1038/ngeo3021.

Wang, Kelin and Garry C. Rogers (1994). "An explanation for the double seismic layers north of the Mendocino Triple Junction". In: *Geophysical Research Letters* 21.2, pp. 121–124. ISSN: 19448007. DOI: 10.1029/93GL03538.

Wang, Kelin and Anne M. Tréhu (2016). "Some outstanding issues in the study of great megathrust earthquakesfffdfffdfffdThe Cascadia example". In: *Journal of Geodynamics* 98, pp. 1–18. ISSN: 02643707. DOI: 10.1016/j.jog.2016.03.010. URL: http://dx.doi.org/10.1016/j.jog.2016.03.010.

Wang, Xin, Kyle Edward Bradley, Shengji Wei, and Wenbo Wu (2018). "Active backstop faults in the Mentawai region of Sumatra, Indonesia, revealed by teleseismic broadband waveform modeling". In: *Earth and Planetary Science Letters* 483, pp. 29–38. ISSN: 0012821X. DOI: 10.1016/j.epsl.2017.11.049. URL: https://doi.org/10.1016/j.epsl.2017.11.049.

Wang, Xin, Shengji Wei, and Wenbo Wu (2017). "Double-ramp on the Main Himalayan Thrust revealed by broadband waveform modeling of the 2015 Gorkha earthquake sequence". In: *Earth and Planetary Science Letters* 473, pp. 83–93. ISSN: 0012821X. DOI: 10.1016/j.epsl.2017.05.032. URL: http://dx.doi.org/10.1016/j.epsl.2017.05.032.

Warren-Smith, E. et al. (2019). "Episodic stress and fluid pressure cycling in subducting oceanic crust during slow slip". In: *Nature Geoscience*. ISSN: 1752-0894. DOI: 10.1038/s41561-019-0367-x. URL: http://www.nature.com/articles/s41561-019-0367-x.

Wech, Aaron G. (2010). "Interactive Tremor Monitoring". In: *Seismological Research Letters* 81.4, pp. 664–669. DOI: 10.1785/gssrl.81.4.664.

Wech, Aaron G. and Kenneth C. Creager (2011). "A continuum of stress, strength and slip in the Cascadia subduction zone". In: *Nature Geoscience* 4.9, pp. 624–628. ISSN: 17520894. DOI: 10.1038/ngeo1215.

Wells, Donald L. and Kevin J. Coppersmith (1994). "New Empirical Relationships among Magnitude, Rupture Length, Rupture Width, Rupture Area, and Surface Displacement". In: *Bulletin of the Seismological Society of America* 84.4, pp. 974–1002. ISSN: 0037-1106. DOI: .

Weston, J, A M G Ferreira, and G J Funning (2011). "Global compilation of interferometric synthetic aperture radar earthquake source models : 1 . Comparisons with seismic catalogs". In: *Journal of Geophysical Research* 116.B08408. DOI: 10.1029/2010JB008131.

Weston, J., A. M.G. Ferreira, and G. J. Funning (2014). "Joint earthquake source inversions using seismo-geodesy and 3-D earth models". In: *Geophysical Journal International* 198.2, pp. 671–696. ISSN: 1365246X. DOI: 10.1093/gji/ggu110.

Williams, Simon D. P., Yehuda Bock, Peng Fang, Paul Jamason, Rosanne Nikolaidis, Linette Prawirodirdjo, Meghan Miller, and Daniel Johnson (2004). "Error analysis of continuous GPS position time series". In: *Journal of Geophysical Research* 109.B3, B03412. ISSN: 0148-0227. DOI: 10.1029/2003JB002741. URL: http://doi.wiley.com/10.1029/2003JB002741.

Wilson, Douglas S (1986). "A kinematic model for the Gorda Deformation Zone as a Diffuse Southern Boundary of the Juan de Fuca Plate". In: *Journal of Geophysical Research* 91, pp. 10259–10269.

— (1989). "Deformation of the so-called Gorda Plate". In: *Journal of Geophysical Research* 94, pp. 3065–3075.

Wit, Maarten J. de, Cornel E. J. de Ronde, Marian Tredoux, Chris Roering, Rodger J. Hart, Richard a. Armstrong, Rod W. E. Green, Ellie Peberdy, and Roger a. Hart (1992). "Formation of an Archaean continent". In: *Nature* 357.6379, pp. 553–562. ISSN: 0028-0836. DOI: 10.1038/357553a0. URL: http://www.nature.com/doifinder/10.1038/357553a0.

"World Bank Group Climate Change Knowledge Portal" (2010). In: URL: http://sdwebx.worldbank.org/climateportal/index.cfm.

Xie, X. and Z. Yao (1989). "A generalized reflection-transmission coefficient matrix method to calculate static displacement field of a dislocation source in a statified half-space". In: *Chinese Journal of Geophysics* 32, pp. 191–205.

Xue, Lian, Emily E. Brodsky, Jon Erskine, Patrick M. Fulton, and Reed Carter (2016). "A permeability and compliance contrast measured hydrogeologically on the San Andreas Fault". en. In: *Geochemistry, Geophysics, Geosystems* 17.3, pp. 858–871. ISSN: 1525-2027. DOI: 10.1002/2015GC006167. URL: http://onlinelibrary.wiley.com/doi/10.1002/2015GC006167/abstract (visited on 05/09/2016).

Yamasaki, Tadashi and Tetsuzo Seno (2003). "Double seismic zone and dehydration embrittlement of the subducting slab". In: *Journal of Geophysical Research* 108, pp. 1–21. DOI: 10.1029/2002JB001918.

Yao, Dongdong, Jacob Walter, Xiaofent Meng, Tiegan Hobbs, Zhigang Peng, Andrew Newman, Susan Y. Schwartz, and Marino Protti (2017). "Detailed spatiotemporal evolution of microseismicity and repeating earthquakes following the 2012 Mw 7.6 Nicoya earthquake". In: *Journal of Geophysical Research : Solid Earth* 122.1, pp. 524–542. DOI: 10.1002/2016JB013632.

Yu, Wen-che (2013). "Shallow-Focus Repeating Earthquakes in the Tonga fffdfffdfffd Kermadec fffdfffdfffd Vanuatu Subduction Zones". In: 103.1, pp. 463–486. DOI: 10.1785/0120120123.

Zhu, Lupei and Donald V. Helmberger (1996). "Advancement in source estimation techniques using broadband regional seismograms". In: *Bulletin of the Seismological Society of America* 86.5, pp. 1634–1641. ISSN: 00371106. DOI: 10.1785/0120160029.

Zoback, Mary Lou (1992). "First- and Second-Order Patterns of Stress in the Lithosphere: The World Stress Map Project". In: *Journal of Geophysical Research* 97.B8, pp. 11703–11728. DOI: 10.1029/92JB00132.

Zoback, Mary Lou, Robert C. Jachens, and Jean A. Olson (1999). "Abrupt along-strike change in tectonic style: San Andreas Fault zone, San Francisco Peninsula". en. In: *Journal of Geophysical Research: Solid Earth* 104.B5, pp. 10719–10742. ISSN: 2156-2202. DOI: 10.1029/1998JB900059. URL: http://onlinelibrary.wiley.com/doi/10.1029/1998JB900059/abstract (visited on 04/05/2016).

Zou, Zhenhua, Xiangming Xiao, Jinwei Dong, Yuanwei Qin, Russell B. Doughty, Michael A. Menarguez, Geli Zhang, and Jie Wang (2018). "Divergent trends of open-surface water body area in the contiguous United States from 1984 to 2016". In: *Proceedings of the National Academy of Sciences* 115.15, p. 201719275. ISSN: 0027-8424. DOI: 10.1073/pnas.1719275115. URL: http://www.pnas.org/lookup/doi/10.1073/pnas.1719275115.

Zumberge, J. F., M. B. Heftin, D.C. Jefferson, M. M. Watkins, and F. H. Webb (1997). "Precise point positioning for the efficient and robust analysis of GPS data from large networks". In: *Journal of Geophysical Research* 102.B3, pp. 5005–5017.